

UNIVERSITY OF CALIFORNIA SAN DIEGO

On the waveform shape of neural oscillations

A dissertation submitted in partial satisfaction
of the requirements for the Doctor of Philosophy

in

Neurosciences

by

Scott Robert Cole

Committee in charge:

Professor Bradley Voytek, Chair
Professor Maxim Bazhenov
Professor Eric Halgren
Professor Eran Mukamel
Professor Lara Rangel

2018

Copyright

Scott Robert Cole, 2018

All Rights Reserved

The Thesis of Scott Robert Cole is approved, and it is acceptable in quality and form for publication on microfilm and electronically:

Chair

University of California, San Diego

2018

DEDICATION

I would like to dedicate this work to the societal structures that are in place such that I was able to have this enriching scientific experience. I am lucky to be born in an era in which I do not need to be a farmer or hunter, and in circumstances which gave me the opportunity to pursue scientific research. I hope that I have not squandered this opportunity and here have contributed something useful to our efforts towards understanding the human brain.

EPIGRAPH

Even though it may be possible to analyze the complex forms of brain waves into a number of different sine-wave frequencies, this may lead only to what might be termed a "Fourier fallacy," if one assumes ad hoc that all of the necessary frequencies actually occur as periodic phenomena in cell groups within the brain. However, frequency analysis, when related at all times to the original recording, is proving to be a useful adjunct to the electroencephalographer's armamentarium, if and when the various spectra thus obtained can receive adequate and valid interpretation.

Herbert H. Jasper. Charting the Sea of Brain Waves. *Science*, 1948.

We note, that for there to be any power in the alpha band (as seen in a spectral analysis) there must be something oscillating in that frequency band to generate that section of the 1/f frequency spectrum. That one does not see an oscillation "by eye" in the 10 Hz frequency range or a bump in the frequency spectrum, but that power exists, implies that the oscillator is heavily damped (overdamped as opposed to underdamped).

Anonymous cognitive neuroscientist, 2018

TABLE OF CONTENTS

Signature Page	iii
Dedication	iv
Epigraph.....	v
Table of Contents.....	vi
List of Figures.....	vii
Acknowledgments.....	ix
Vita	xi
Abstract of the Dissertation.....	xii
Introduction	1
Chapter 1 Nonsinusoidal beta oscillations reflect cortical pathophysiology in Parkinson's disease	26
Chapter 2 Cycle-by-cycle analysis of neural oscillations	58
Chapter 3 Hippocampal theta bursting and waveform shape reflect CA1 spiking patterns	99
Conclusion	140

LIST OF FIGURES

Figure 0.1: Oscillatory waveforms are nonsinusoidal in many neural recordings and simulations	6
Figure 0.2: Features of nonsinusoidal waveforms relate to physiology.....	14
Figure 0.3: Features of oscillatory waveforms relate to behavior and disease	18
Figure 1.1: Waveform shape of M1 beta oscillation changes in PD	36
Figure 1.2: M1 beta oscillations have a consistent sawtooth shape	38
Figure 1.3: Estimates of phase-amplitude coupling in PD.....	40
Figure 1.4: Sharp beta oscillations yield phase-locked high gamma amplitude	43
Figure 1.5: Power spectral properties of motor cortical recordings and relation to estimated phase-amplitude coupling	47
Figure 1.6: Sharp beta oscillations produce similar cross-frequency coupling estimates compared to canonical phase-amplitude coupling	51
Figure 2.1: Decomposing a neural signal into individual cycles	69
Figure 2.2: Distributions of cycle features differ between theta oscillations recorded in the CA1 pyramidal layer and layer 3 of the entorhinal cortex (EC3)	71
Figure 2.3: Determining oscillatory bursts in a neural signal.....	73
Figure 2.4: Validating cycle-by-cycle analysis with simulated data	75
Figure 2.5: Comparison of cycle-by-cycle and instantaneous amplitude analysis on simulated event-related data	79
Figure 2.6: Comparison of cycle-by-cycle and instantaneous frequency analysis on simulated data	80
Figure 2.7: Autocorrelation of cycle features within, but not between, bursts of the hippocampal theta oscillation.....	82
Figure 2.8: Difference between hippocampal theta oscillations between running and not running in an example rat.....	85
Figure 2.9: Changes in motor cortical beta oscillation shape with deep brain stimulation (DBS) treatment of Parkinson's disease	86
Figure 2.10: Differences in the visual alpha rhythm between periods of eyes-closed resting and eyes-open task in an example subject	87
Figure 3.1: Cycle-by-cycle characterization of the rodent hippocampal theta rhythm	109

Figure 3.2: Correlations between features of hippocampal theta cycles	111
Figure 3.3: Comparison of hippocampal theta cycle features between movement and nonmovement.....	113
Figure 3.4: Spike-field coupling of CA1 neurons to the hippocampal theta rhythm.....	115
Figure 3.5: Theta cycle features are correlated to neuronal firing rate.....	119
Figure 3.6: Neuronal synchrony and sequence are correlated with theta cycle features	123
Figure 3.7: Characteristics of theta bursts and their relationship to cycle features and neuronal firing.....	127
Figure 3.8: Schematized summary of observed relationships between theta oscillation bursting, waveform shape, and local neuronal firing patterns	129

ACKNOWLEDGEMENTS

I would like to acknowledge the members of the Voytek lab for their support over the past 4 years. I feel lucky to have been able to spend this time learning from them and debating the nuances of our research and academia in general. Foremost, I'd like to thank my advisor, Brad Voytek, for his multifaceted mentoring and for nurturing a fun and enriching lab environment. I was especially lucky to join the lab along with 3 other PhD students who have worked alongside me and helped me brainstorm. Tammy Tran often gave helpful advice for with my writing and control analyses, Tom Donoghue has helped make me a much better python programmer, and Richard Gao taught me a lot as we debated about the intricacies of spectral analysis. I also want to thank former post docs Erik Peterson and Roemer van der Meij for their mentorship and advice specifically in programming and signal processing, respectively. Furthermore, I thank the undergraduate researchers for their work in pursuing ideas similar to this thesis: Yimeng Yang, Sunny Pasumarthi, Jenny Hamer, and Andrew Washington.

I would also like to acknowledge generous funding from the National Science Foundation Graduate Research Fellowship program and the Frontiers of Innovations Scholars Program at UC San Diego.

The introduction, in part, is an adaptation of the material that appears in: Cole SR, Voytek B. (2017) Brain oscillations and the importance of waveform shape. *Trends in Cognitive Sciences*, 21(2), 137-149. The dissertation author was the primary investigator and author of this paper.

Chapter 1, in full, is a reprint of the material as it appears in: Cole SR, van der Meij R, Peterson EJ, de Hemptinne C, Starr P, Voytek B. (2017) Nonsinusoidal oscillations underlie pathological phase-amplitude coupling in the motor cortex in Parkinson's disease. *Journal of*

Neuroscience, 37(18) 4830-4840. The dissertation author was the primary investigator and author of this paper.

Chapter 2, in full, has been submitted for publication of the material as it currently appears in: Cole SR, Voytek B. (2018) Cycle by cycle analysis of neural oscillations. *bioRxiv*. The dissertation author was the primary investigator and author of this paper.

Chapter 3, in full, has been submitted for publication of the material as it currently appears in: Cole SR, Voytek B. (2018) Hippocampal theta bursting and waveform shape reflect CA1 spiking patterns. *bioRxiv*. The dissertation author was the primary investigator and author of this paper.

VITA

2014	Bachelor of Science, Clemson University
2017	Data science intern, Crime Lab New York
2018	Doctor of Philosophy, University of California San Diego
2019	Fellow, Insight Data Science - Silicon Valley

PUBLICATIONS

Cole SR, Voytek B. (2018) Hippocampal theta bursting and waveform shape reflect CA1 spiking patterns. *bioRxiv*.

Cole SR, Voytek B. (2018) Cycle by cycle analysis of neural oscillations. *bioRxiv*.

Cole SR, van der Meij R, Peterson EJ, de Hemptinne C, Starr P, Voytek B. (2017) Nonsinusoidal oscillations underlie pathological phase-amplitude coupling in the motor cortex in Parkinson's disease. *Journal of Neuroscience*, 37(18) 4830-4840.

Cole SR, Voytek B. (2017) Brain oscillations and the importance of waveform shape. *Trends in Cognitive Sciences*, 21(2), 137-149.

Mohammed FS, Cole SR, Kitchens CL. (2013) Synthesis and Enhanced Colloidal Stability of Cationic Gold Nanoparticles using Polyethyleneimine and Carbon Dioxide. *ACS Sustainable Chem. Eng.*, 1(7), 826-832.

ABSTRACT OF THE DISSERTATION

On the waveform shape of neural oscillations

by

Scott Robert Cole

Doctor of Philosophy in Neurosciences

University of California San Diego, 2018

Professor Bradley Voytek, Chair

Brain rhythms, or neural oscillations, are one the most prominent features of electrical brain recordings. Over the past century, they have been studied for their relationships to healthy behavior, neurological diseases, and physiological changes. Theories have developed for how these oscillations may play key roles in neural communication and computation. Many discoveries have been made by analyzing these rhythms using tools based on the Fourier transform, which decomposes the neural signal as a sum of rhythmic sine waves. However, the rhythms in these signals often have waveforms that significantly deviate from sine waves. Therefore, the standard Fourier decomposition may not be optimal for studying the potential meanings of these nonsinusoidal features. In this dissertation, I begin by reviewing the literature of the sparse reports of nonsinusoidal waveform shape and its potential physiological meaning.

Using a dataset of motor cortical electrocorticography recordings from Parkinson's Disease patients, I show that deep brain stimulation treatment decreased the sharp shape of the patients' beta oscillations. Furthermore, I showed that this waveform shape change underlied past reports of phase-amplitude coupling, and that the coupled high gamma power was predominantly coming from the sharp extrema of the nonsinusoidal beta wave. Next, I propose a cycle-by-cycle analysis framework for analyzing the waveform shapes of oscillations across neural recordings. Finally, I apply this framework to study the sawtooth-shaped rodent hippocampal theta rhythm. I found that the waveform shape of this rhythm contained information about the firing rates, synchrony, and sequences of the local hippocampal CA1 neuron population. Rather than being a nuisance, I conclude that these nonsinusoidal features may provide critical, heretofore overlooked physiological information related to neural communication, computation, and cognition.

INTRODUCTION

In order to accomplish tasks at fast time scales, the brain not only relies on biochemical mechanisms but also electrical ones. Therefore, electrophysiology is a critical component in efforts to understand how the human brain works. Brain rhythms, or neural oscillations, are the prominent features of macroscale electrophysiological recordings, and they are thought to be implicated in virtually every behavior and neuropathology (Buzsáki and Draguhn, 2004). While structural changes to the brain happen on relatively long time scales, oscillations are theorized to support mental functions that require dynamically switching between functional neural circuits (Fries, 2005; Womelsdorf et al., 2014; Voytek and Knight, 2015). While evidence for causal or mechanistic roles of neural oscillations is currently limited, correlational studies have shown promise for the importance of various brain rhythms. I became interested in how oscillations relate to mental processes such as memory (Klimesch, 1999) and disorders including Parkinson's disease (de Hemptinne et al., 2013). Recording brain rhythms has proven useful toward developing biomarkers of neurological diseases (Buzsáki and Watson, 2012) and for training successful brain-machine interfaces (Leuthardt et al., 2004).

Rhythms in neural activity are observed across various temporal and spatial scales (Buzsáki and Draguhn, 2004). Traditionally, neural oscillations have been clustered into canonical frequency bands, including delta (1-4 Hz), theta (4-8 Hz), alpha (8-12 Hz), beta (15-30 Hz), gamma (30-90 Hz), and high gamma (>50 Hz). These bands roughly correspond to frequency ranges commonly observed in human electroencephalography (EEG). Though they have been observed for nearly a century, recent theories suggest that these oscillations play an active role in neural communication (Fries, 2005).

One prominent theory is that oscillations accomplish this function using cross-frequency coupling, in which multiple neural oscillators in different frequency ranges interact with one another (Canolty and Knight, 2010). To characterize this coupling, the phase and amplitude properties of each oscillator are calculated using spectral analysis. A key feature in all spectral

analysis methods is that they inherently assume that the fluctuations in brain activity over time can be characterized using a sinusoidal basis. That is, the underlying assumption is that the complexities of oscillatory brain activity are best captured by sinusoidal oscillators. A sinusoid (or sine wave) is a smoothly-varying rhythmic signal governed by a mathematical equation. However, the focus of this thesis is that neural oscillations are commonly nonsinusoidal. Rather than being a nuisance, I argue that these nonsinusoidal features may contain critical physiological information about the neural systems and dynamics that generate them. My goal is to address the inconsistency between standard neural analysis approaches and the observed nonsinusoidal shapes of oscillatory waveforms, which is particularly highlighted in Chapter 1.

I begin by reviewing a diverse set of examples of nonsinusoidal oscillations across species and brain regions in this introduction. Interestingly, studies published prior to the modern proliferation of advanced computation focused more on raw, unfiltered data, by necessity. In contrast, recent studies tend to focus on heavily processed data and lack attention to the oscillatory waveform shapes. I discuss past methodological approaches for characterizing nonsinusoidal features of neural oscillations, as well as adaptations to traditional spectral analysis to account for nonsinusoidal waveforms. In Chapter 2, I outline and motivate our proposed cycle-by-cycle approach for analyzing the waveform shape of brain rhythms. In Chapter 3, I apply this method to explore if waveform shape contains information about local neuronal firing patterns. Combining waveform shape analysis with a modern understanding of the physiological generators of neural oscillations can provide an entirely new framework for understanding the physiological basis of neural computation and cognition.

Nonsinusoidal waveforms are stereotyped

One strong indication that the waveform shape of neural oscillations contains physiological information is that features of these waveforms are stereotyped across recordings. This consistency indicates that the waveform shape reflects something specific about the physiology of the recorded brain region. Here I review several examples of this phenomena.

In human electrophysiology, oscillations with stereotyped nonsinusoidal shapes include the sensorimotor “mu rhythm,” motor cortical beta oscillation, and cortical “slow oscillations”. The mu rhythm oscillates at an alpha frequency (around 10 Hz) and was named because its waveform shape resembles the Greek character μ (Fig. 0.1A). It is characterized by the fact that one extremum (e.g., its peak) is consistently sharper than the other (e.g., its trough); it is also described as an arch, comb, or wicket shape (Kuhlman, 1978; Tiihonen et al., 1989; Arroyo et al., 1993; Salmelin and Hari, 1994; Pfurtscheller et al., 1997, 2006; Muthukumaraswamy et al., 2004).

In addition to the sensorimotor mu rhythm, we have recently highlighted that motor cortical beta oscillations also have striking nonsinusoidal features (see Chapter 1). These beta oscillations manifest a sawtooth shape, in that their voltage either rapidly rises before more slowly falling off, or vice versa (Fig. 0.1B).

In contrast to these faster rhythms, “slow oscillations” are low-frequency rhythms (<1 Hz) that dominate across the cerebral cortex during anesthesia and natural sleep (Steriade et al., 1993; Amzica and Steriade, 1998, 2000). Slow oscillations are distinguished by alternating periods of depolarization (up states, positive half-wave in surface EEG) and hyperpolarization (down states, negative half-wave in surface EEG) (Amzica and Steriade, 1998). The negative half-waves are consistently sharper than the positive half-waves, again resulting in a stereotyped arch-like shape (Mölle et al., 2002; Massimini et al., 2004; Clemens et al., 2007; Ngo et al., 2013). Because the waveform shapes of these oscillations are relatively conserved across brain regions, people, and even species, we reason that these oscillation features likely contain information about the oscillatory generators. Due to the assumptions of standard sinusoid-based spectral analyses, these potentially critical nonsinusoidal features will be lost or overlooked.

Animal models also give us an opportunity to invasively record nonsinusoidal oscillations often not feasible to record in humans. Hippocampal theta oscillations, for example, are among

the most studied rhythms in the local field potential (LFP); they have a stereotyped sawtooth shape (Fig. 0.1C) (Green and Petsche, 1961; Artemenko, 1973; Buzsáki et al., 1985; Belluscio et al., 2012; Dvorak and Fenton, 2014; Lockmann et al., 2016). Similarly, respiratory rhythms in the olfactory bulb are also sawtooth-like in shape (Buonviso et al., 2003; Lockmann et al., 2016). While slow oscillations are arch-shaped when recorded with macroelectrodes, those recorded in the LFP have complex and diverse shapes, with sharp transitions between the up and down states (Fig. 0.1D) (Amzica and Steriade, 1998; Fröhlich and McCormick, 2010; Lockmann et al., 2016; Ouedraogo et al., 2016). These invasive recordings present a unique opportunity to extract information from waveform shape because of their closer proximity to the signal source.

If an oscillation's waveform shape reflects physiology that is truly evolutionarily conserved, we expect to see similar waveform features in analogous oscillations across species. One example of such conservation is the stereotyped sawtooth waveform of the hippocampal theta rhythm is observed in rabbit, mouse, and rat (Bland et al., 1980; Buzsáki et al., 1985, 2003). Also, the arch-shaped alpha-frequency oscillations observed in rat somatosensory cortex, which have been hypothesized to be analogous to the previously mentioned mu rhythms in EEG (Wiest and Nicolelis, 2003; Fransen et al., 2016). Additionally, slow oscillations are also arch-shaped in surface EEG in the anesthetized cat (Amzica and Steriade, 1998), to give but three examples. Concerning slow oscillations, Amzica & Steriade presaged in 1998 that “Fourier spectra are not able to discriminate between periodic phenomena and waves with a given shape,” noting that analyses “should take into consideration the actual aspect of waves and, if possible, their relationship with the state of the cellular aggregates of the corticothalamic network” (Amzica and Steriade, 1998). Here I extend this sentiment to all neural oscillations.

In addition to the variety of empirical reports, theoretical estimates of field activity acquired through computational modeling are also notably nonsinusoidal. A common method for

simulating gamma oscillations, for example, is the biophysically-inspired pyramidal-interneuron gamma (PING) cortical model. In a morphologically-realistic simulation of the LFP, gamma oscillations show a sawtooth-like waveform shape; while the decay phase was very short, the voltage rise had an exponentially decaying trajectory, analogous to synaptic currents (see Fig. 0.1E). In comparison, a slightly different implementation of the PING model yielded gamma oscillations with an arch shape (Lowet et al., 2016). The different oscillatory shapes generated by different PING models are driven by differences in the defined biophysical parameters, hinting at a link between biophysics and waveform shape.

Other computational models of neural oscillations are more abstract and do not directly simulate the synaptic currents that largely underlie the LFP. Still, the waveform generated by a Morris-Lecar model (Somers and Kopell, 1993) (Fig. 0.1F, top) has a strikingly similar waveform to the slow oscillations shown in Fig. 0.1D. By changing the parameters of the model oscillators, researchers can fit simulated waveforms to those recorded in the LFP. In theory, this technique of altering biophysical parameters in LFP simulations to fit waveform shape can be inverted to try and infer biophysical parameters from the LFP. This could prove to be an enticing extension to the common analytic toolkit used to study oscillations, moving beyond standard spectral analyses to more physiologically informed approaches.

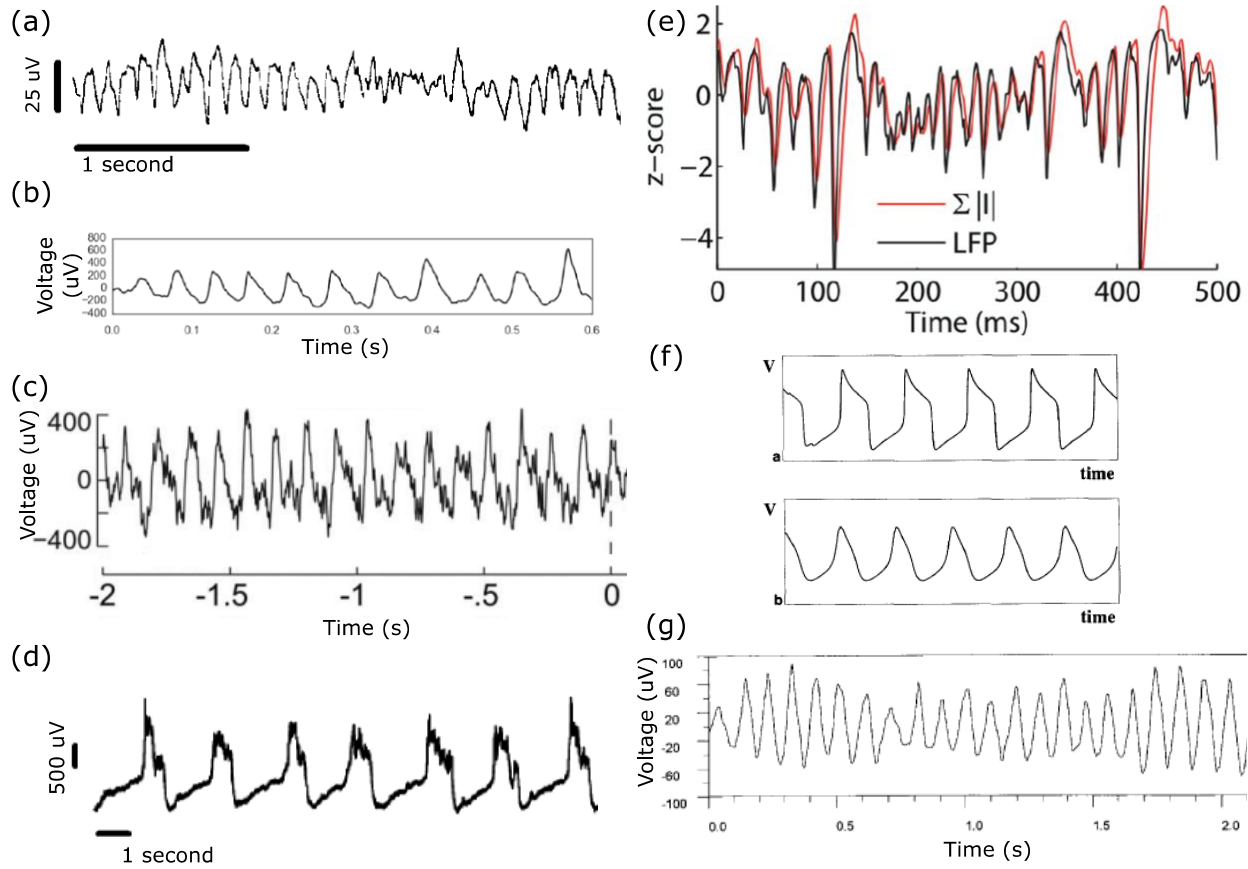


Figure 0.1. Oscillatory waveforms are nonsinusoidal in many neural recordings and simulations. (a) The mu rhythm, a motor cortical oscillation with power at 10 Hz, is characterized by its sharp extrema which produce an arch shape. (b) Beta oscillations in the human primary motor cortex (ECoG) have sharp and sawtooth-like features. Produced by the authors. (c) Theta oscillations in the rodent hippocampus have a sawtooth-like waveform in which oscillatory rises are steeper than decays. (d) Slow oscillations in the neocortex have complex waveforms that contain aspects of arches, sawtooths, and rectangular waves. (e) Gamma oscillations produced by the pyramidal-interneuron gamma (PING) mechanism. Field potentials were generated both in a population of morphologically realistic neurons (black) and by using a weighted sum of synaptic currents (red). In both cases, the waveforms had an asymmetric shape: a sharp voltage drop followed by an exponential-shaped voltage rise. (f) The waveform shape of a conductance-based Morris-Lecar oscillator model changes with the lambda parameter (top: $\lambda=0.02$, bottom: $\lambda=0.33$), though they are never truly sinusoidal. Note that the top example is strikingly similar to the temporal dynamics of slow oscillations recorded in the parietal cortex of rats (see panel d). (g) An example of the occipital alpha that appears to have a shape that is more triangular than sinusoidal.

Methods for characterizing nonsinusoidal oscillations

Given the numerous examples of stereotyped oscillatory waveforms described above, metrics have been developed to quantify the features of the waveform shape, though they are underutilized. We recently quantified the sharpness of peaks and troughs by calculating the short-term voltage change around each extrema in the raw trace (see Chapter 1). The ratio between peak and trough sharpness was shown to differentiate neural activity between neurological treatment conditions in Parkinson's disease. In addition to the symmetry of oscillatory peaks and troughs, other studies have quantified the symmetry between the rise and decay phases to determine how rapidly the voltage rises compared to its decay time. The ratio between the rise time and decay time has been used to quantify the sawtooth nature of the hippocampal theta rhythm, where the rise phase is consistently shorter than the decay phase (Belluscio et al., 2012; Dvorak and Fenton, 2014). Similarly, a "slope ratio" has been used to compare the steepness of the rise period to that of the adjacent decay period (Lee and Jones, 2013). While promising, these metrics do not capture the full space of possible waveform features, so more approaches will need to be developed to further characterize oscillatory waveforms. Links between nonsinusoidal waveform shape and physiology will be more accurate by measuring multiple waveform features.

In addition to quantifying features of the waveform shape, methods have been developed to account for nonsinusoidal waveforms when performing traditional spectral analysis. Nonsinusoidal oscillations have been shown to generate unintuitive phase and amplitude estimates (Dvorak and Fenton, 2014; van Driel et al., 2015; Amiri et al., 2016b; Jones, 2016). The amplitude of high frequency oscillations is spuriously increased when filtering sharp transients (Amiri et al., 2016b). To correct for this, a classifier was developed to differentiate sharp events with and without high frequency oscillations (Amiri et al., 2016b). Because the hippocampal theta waveform has such a striking sawtooth shape, some researchers studying the phase of this oscillation have developed alternative waveform-based

phase estimates that interpolate between empirically identified time points, including extrema and zero-crossings (Siapas et al., 2005; Belluscio et al., 2012; Dvorak and Fenton, 2014; Trimper et al., 2014). Using this approach, it was shown that decoding of a rat's spatial position is improved by referencing spiking to this alternate phase estimate as compared to traditional sinusoidal phase estimates (Belluscio et al., 2012).

Because both phase and amplitude estimates can be unintuitive for nonsinusoidal oscillations, waveform shape is an important consideration in phase-amplitude coupling (PAC) analysis, which quantifies the correlation between the phase of one oscillator and the amplitude of a higher-frequency oscillator. Past studies have provided various recommendations for assessing whether PAC is true or spurious (Kramer et al., 2008; Ray and Maunsell, 2011; Aru et al., 2015; Gerber et al., 2016; Jones, 2016; Lozano-Soldevilla et al., 2016; Vaz et al., 2017). Here I suggest that the spurious/non-spurious dichotomy may not be useful, as "spurious" implies uninformative. In contrast, I argue that apparent PAC that arises from nonsinusoidal features is still a valid measure of signal properties, though the biophysical interpretation may differ depending on the waveform properties that give rise to the observed PAC. That is, statistically significant PAC may not indicate two interacting oscillators at different frequencies, but rather may reflect one regular nonsinusoidal oscillator.

PAC methods have been recently adapted to account for nonsinusoidal oscillations. Because nonsinusoidal oscillations produce a nonuniform distribution of instantaneous phase, PAC estimates may be biased, and a correcting factor based on phase nonuniformity was suggested (van Driel et al., 2015). This nonuniform phase distribution also confounds analyses of phase-locked spiking, which can be appropriately addressed using surrogate statistics (Sigurdsson et al., 2010). As for amplitude estimates, the previously mentioned classifier that detects true high frequency oscillations was applied to assess PAC changes while avoiding the confounding effects of sharp transients (Amiri et al., 2016a). Ultimately, measuring the waveform shape of oscillations would clarify the implications of PAC estimates.

While nonsinusoidal oscillations are not parsimoniously captured in the components of the Fourier transform, alternative decomposition methods have been applied to study neural oscillations (Mäkinen et al., 2005; Chandran K S et al., 2016). In contrast to techniques like the Fourier transform, the matching pursuit algorithm decomposes the signal using transient broadband functions in addition to narrowband functions, making it suitable for capturing physiologically-informative sharp waveform features (Chandran K S et al., 2016). Another approach, empirical mode decomposition (EMD), decomposes a signal into rhythmic components based on local extrema rather than sinusoidal components. One study showed that EMD improved the frequency resolution of coupling in both simulated data and mouse hippocampal recordings (Pittman-Polletta et al., 2014). EMD was also applied to analyze amplitude-amplitude coupling in an attempt to account for the fact that such coupling is positively biased by nonsinusoidal and nonstationary oscillations (Yeh et al., 2016). Thus, decomposition methods that do not assume a sinusoidal basis may be more appropriate for analyzing the spectral properties of oscillations with a nonsinusoidal waveform shape.

While such approaches require multiple oscillatory cycles to yield useful metrics, studying the temporal dynamics of single oscillatory cycles can also reveal critical physiological information, as previously suggested (Artemenko, 1973; Jones, 2016). The fast (30-60 Hz) arch-shaped oscillations produced in response to cortical injury in the rabbit are relevant here (Adrian and Matthews, 1934). At the start of injury, monophasic spikes appear in isolation but gradually become broader and more frequent, generating an arch-shaped oscillation, followed by a quasi-sinusoidal oscillation. From a nonsinusoidal perspective, each period of the oscillation has its own interesting temporal dynamics. Therefore, analysis of each period as an individual event may be more appropriate than analyzing the series of events as one oscillatory process.

Distinguishing different oscillatory processes by waveform shape

The aforementioned methods for quantifying the features of oscillatory waveforms can be used to distinguish between oscillatory phenomena that appear at similar spatial locations at

the same frequency but have different physiological origins. Because distinct neural processes can co-exist in the same frequency band, applying a narrow bandpass filter may make multiple distinct oscillatory processes indistinguishable from one another. For example, in the rat gustatory cortex there are three alpha frequency rhythms that appear to be distinct because they occur at a specific time during a sensory experience and can be distinguished by their waveform shape in addition to their center frequency and amplitude (Tort et al., 2010).

Similarly, two of the earliest identified signals in human EEG were the visual cortical alpha oscillation and the aforementioned sensorimotor mu rhythm. Because of their sometimes overlapping spatial topographies and frequencies (8-12 Hz), the two oscillations can be misidentified and confused with one another (Pineda, 2005). However, an important difference between these two rhythms is their waveform shape. As mentioned above, the mu rhythm has an arch-like waveform while, in contrast, the occipital alpha oscillation has a more symmetric waveform that even appears characteristically triangular in some raw traces (Stam et al., 1999) (Fig. 0.1G). These differences in shape likely reflect differences in the properties of these two oscillatory generators. The sharp transient of the mu rhythm is hypothesized to reflect a current source in the primary somatosensory hand area (Tiihonen et al., 1989). The occipital alpha oscillation may manifest as a smoother waveform because the underlying current source is less temporally synchronous. This hypothesized difference in physiology is analogous to previous hypotheses regarding the differences in the shapes of slow oscillations (Amzica and Steriade, 1998).

In addition to slow oscillations, 1-5 Hz sawtooth-shaped waves also occur in human EEG and are particularly associated with REM sleep (Berger et al., 1962; Pearl et al., 2002; Louis et al., 2004). Noting the shape of this rhythm has helped associate it with distinct behaviors and mechanisms that would not have been possible if it was simply filtered and identified as a “delta oscillation.” Additionally, sleep spindles are characterized as bursts of 8-14

Hz oscillations that are observed during sleep, along with slow oscillations and sawtooth waves. Sleep spindle subtypes can be distinguished by their shape (Pavlov et al., 2012).

Oscillation waveform shape relates to physiology

Robust differences in the waveform shapes of the oscillations mentioned above can be assumed to represent differences in properties of their underlying generators. For example, the sharp transients that occur in spike-wave discharges, as well as in an alpha rhythm in the gustatory cortex, correspond to synchronous local spiking (Coenen and Van Luijtelaar, 2003; Slaght et al., 2004; Fontanini and Katz, 2005; Fabricius et al., 2008). In contrast, the smooth “wave” component of the spike-wave discharge coincided with a slow depolarization of layer 5/6 neurons (Polack et al., 2007). The “spike” portion of this waveform was preceded by a layer-specific firing pattern, coincided with fast depolarization, and followed by fast hyperpolarization of these layer 5/6 neurons. Given the known variability of the generators for spike-wave discharge shapes (Slaght et al., 2004), quantifying differences in waveform shape may explain some differences in the type or stage of epilepsy.

Waveform shape differences are also observed within a region. The longer duration of slow oscillation up states in the infragranular layers (below pyramidal cell bodies) compared to supragranular layers (above pyramidal cell bodies) contains information on how the slow oscillation is generated across layers (Fröhlich and McCormick, 2010). By analyzing multielectrode recordings throughout the hippocampus, the hilar region has consistently been observed to have the most sinusoidal oscillations (see ‘hil’ in Fig. 0.2A) (Buzsáki et al., 1986; Konopacki et al., 1988; Montgomery et al., 2009). These results suggest that the electrical properties of these oscillations are nonuniform across the region, even if the whole region contains power at the same frequency.

In addition to differences across cortical layers, waveform shape may also contain information about the neurotransmitters present. Again in the hippocampus, the addition of atropine, which blocks acetylcholine receptors, resulted in more irregular theta oscillations, as

characterized by broader distributions in cycle length and trough amplitude (Fig. 0.2B) (Hentschke et al., 2007). In contrast, urethane anesthesia makes the theta oscillation more symmetric . Addition of kainate to hippocampal slices induced gamma oscillations that were more sawtooth-shaped than spontaneously-generated gamma oscillations (Pietersen et al., 2009). The near-instantaneous voltage drop followed by an exponentially decaying voltage rise observed in the kainate-induced gamma oscillations is strikingly similar to the gamma oscillations produced in a previously-mentioned PING model (Mazzoni et al., 2015). In summary, these experiments suggest that the shape of the LFP may index the influence of neurotransmitters on neurophysiology. However, since reports analyzing waveform shape are sparse, it is difficult to generalize these results.

Attempts to explain distinct waveform shapes can inspire models of their physiological generation. A recent study did just this for the transient beta oscillations recorded by MEG in primary somatosensory cortex (S1) and right inferior frontal cortex (IFC) (Fig. 0.2C) (Sherman et al., 2016). The S1 beta waveform is shaped such that the central trough is sharper and more negative than the adjacent troughs, consequently making its flanks relatively steep. It was proposed that the transient oscillations could be generated by nearly synchronous excitatory synaptic burst inputs into the proximal and distal dendrites of pyramidal cells. However, the relative size of the peaks and troughs differed between S1 and IFC; follow up studies incorporating more physiological and architectural features may be able to explain this difference.

For some oscillations, waveform shape may be a surrogate for the population firing rate throughout a period. This relates trivially to slow oscillations in which one extremum is associated with greater local firing whereas the opposite phase is associated with lower firing. Additionally, asymmetric peaks in a slow oscillation period are indicative of strong spiking in that cycle (Lewis et al., 2012), and the sawtooth shape of hippocampal theta oscillations tracks firing rate better than a comparable sinusoid (Fig. 0.2D) (Belluscio et al., 2012). However, the amount

of firing rate variance explained by the oscillation waveform in general is unclear, and likely differs by the identity of the oscillator being studied. In a model of cortical gamma oscillations, the population firing rate was a candidate proxy for the biophysically-computed LFP ($R^2 > 0.5$) (Mazzoni et al., 2015). However, waveform shape may not reflect solely neural processes, as glial membrane potentials are synchronized to slow oscillations and have similar shapes (Amzica and Steriade, 1998, 2000).

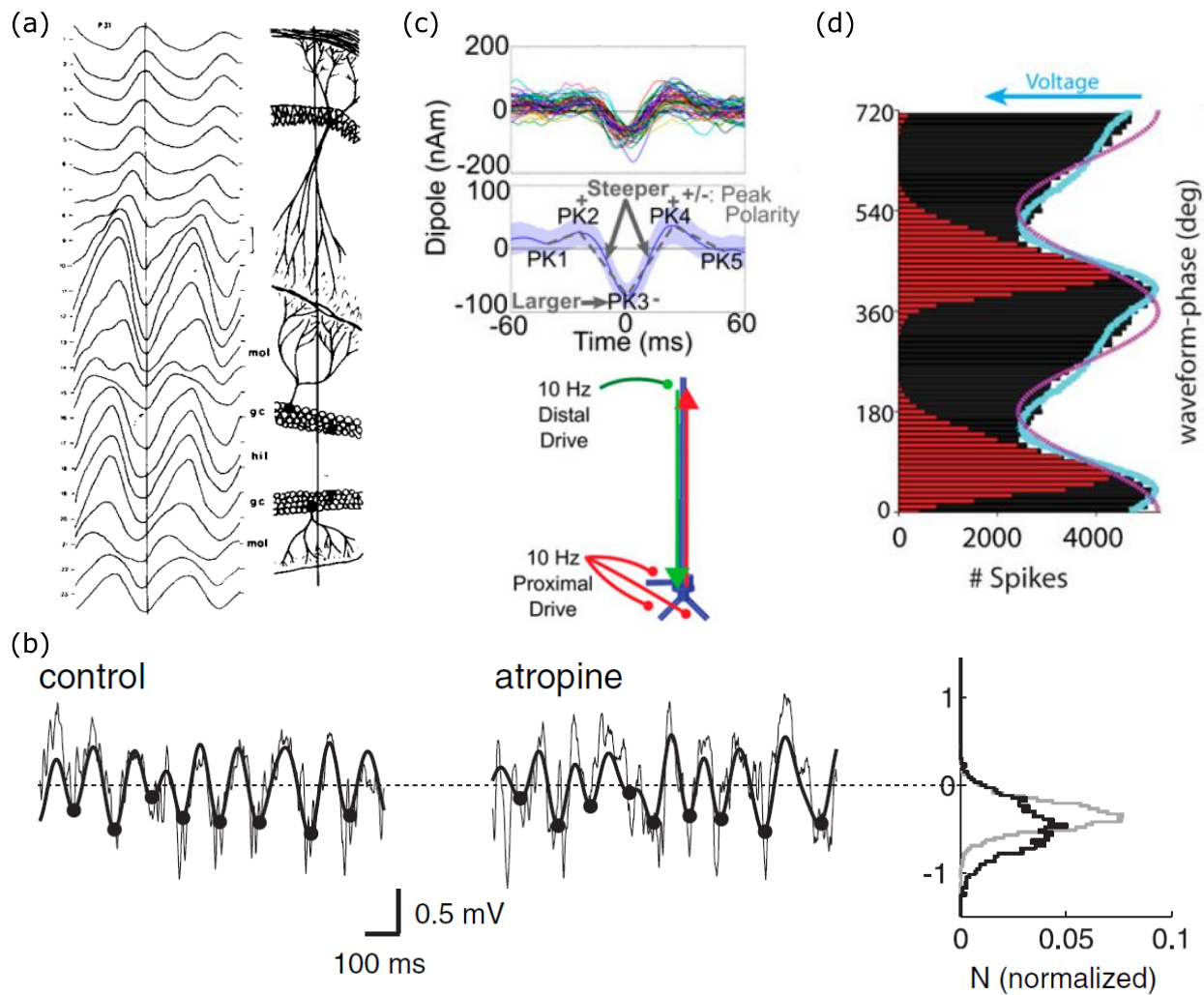


Figure 0.2. Features of nonsinusoidal waveforms relate to physiology. (a) The shapes of hippocampal theta oscillations change as a function of recording depth. (b) Theta oscillations recorded in mouse hippocampus during exploration without (left) and with (center) addition of atropine. The voltage at each trough is indicated with a dot and the distribution of voltages are represented in histograms (right). Addition of atropine blocks muscarinic acetylcholine receptors and causes the trough voltage to be more variable (broader, black histogram). (c) Transient beta oscillations in human somatosensory cortex recorded by MEG. (top) Examples of raw beta oscillations aligned to the largest trough. (center) The average waveform (shading = standard deviation) has a sharp, steep center transient. (bottom) This waveform shape was reproduced in a model by synchronous excitatory synaptic drive both distal and proximal to the soma. (d) The temporal dynamics of extracellular theta oscillations relate to those of firing rates. The firing histogram color indicates if the spike occurred in the rise of a theta oscillation (red) or the decay (black). The blue line indicates the median voltage of the theta oscillation in each phase bin. The purple line is a sinusoid of comparable frequency. Note that the nonsinusoidal voltage trace is more highly correlated to the population firing rate compared to the sinusoid.

As suggested earlier, the shape of an oscillatory waveform can be analyzed to test whether it is consistent with a proposed model of generation. This has been used, for example, in one modeling study that generated gamma oscillations using two different mechanisms. These two oscillators manifested waveforms that differed in slope ratio (defined above), predicting different waveform shapes (Lee and Jones, 2013). In another example, an oscillation generated by pulsing inhibition has been hypothesized to produce an oscillation with “amplitude asymmetry” (Mazaheri and Jensen, 2010). Amplitude asymmetry occurs when the trough voltage remains constant while the peak voltage fluctuates (or vice versa). Thus it has been proposed that pulsing inhibition is the underlying mechanism of some MEG oscillations projected to occipital, central, and parietal areas that have this property (Nikulin et al., 2007; Mazaheri and Jensen, 2008, 2010; van Dijk et al., 2010). This model is consistent with known inhibitory feedback from the neocortex and thalamus (Mazaheri and Jensen, 2010), but direct empirical evidence is needed to confirm this model.

Causal evidence of the computational importance of oscillatory waveform shape comes from studies applying oscillatory neurostimulation. Modifying the shape of the stimulating waveform, while preserving amplitude and frequency, resulted in changes in the efficiency of entraining local population spiking in slices (Fröhlich and McCormick, 2010) and alpha oscillations in human EEG (Dowsett and Herrmann, 2016). In both cases, it was concluded that the steep slopes of the nonsinusoidal stimulation are key in entraining the network, reminiscent of a previous modeling result showing that nonsinusoidal oscillators synchronize faster to one another compared to more sinusoidal oscillators (Somers and Kopell, 1993). Relatedly, rectangular waves induce seizures more reliably than sine waves for electroconvulsive therapy (Merritt, 1938; Abrams, 2002), and sine wave stimulation is associated with greater memory loss and more intense seizures (Weiner et al., 1986a, 1986b). In summary, the effects of neurostimulation vary greatly with the stimulating waveform, suggesting that electrical waveforms generated by the brain may also impact neural computation in different ways.

Oscillatory waveform shape relates to disease and behavior states

Two recent studies have compared the shape of neural oscillations between disease states. In anesthetized rats, the relative duration of up and down states were measured in parietal cortical slow oscillations (Ouedraogo et al., 2016). There was no difference in slow oscillation frequency between rats developing epilepsy compared to control animals. However, the rats developing epilepsy had relatively longer up states. Recently we analyzed primary motor cortical ECoG from patients with Parkinson's disease who had undergone implantation of a permanent deep brain stimulator (DBS), as explained in detail in Chapter 1. Oscillations were most asymmetric in regards to peak and trough sharpness in recordings from untreated Parkinsonian patients compared to those same patients when their DBS was turned on (Fig. 0.3A). Sharpening of oscillatory beta extrema may reflect an increase in synchrony of synaptic bursts (Sherman et al., 2016) thought to be pathological in Parkinson's disease.

There is mounting evidence that the prominent hippocampal theta oscillation shape is altered with behavior. In particular the aforementioned sawtooth shape of hippocampal theta has been reported to become more asymmetric (i.e., approaching the instantaneous voltage change that characterizes a pure sawtooth) when a rat is running, compared to during immobility (Hentschke et al., 2007), lever pressing (Buzsáki et al., 1985), or REM sleep (Belluscio et al., 2012) (Fig. 0.3B). This change in the asymmetry of hippocampal theta oscillations during running must reflect a change in the rhythmic neural computation. Future studies could identify the mechanisms associated with changes in theta asymmetry and what significance this has for running behavior. A similar analysis on theta oscillations was performed during memory encoding periods (Trimper et al., 2014). During encoding of objects that were subsequently remembered (compared to subsequently forgotten), the rat's hippocampal theta oscillation was more asymmetric (Fig. 0.3C). There was no accompanying change in theta frequency or amplitude. The authors theorized that this elongation of the theta oscillation's falling slope improved memory by enhancing CA3-CA1 gamma coherence. Future studies can

test this hypothesis by using electrical or optogenetic stimulation to manipulate the shape of the theta waveform in CA1.

Concluding remarks

Here I reviewed a broad literature showing that oscillations have diverse waveform shapes. These nonsinusoidal features likely relate to physiology, making it theoretically possible to infer physiology from waveform shape. This idea has been hinted at or directly mentioned in several past reports, however, such reports of waveform shape have been brief and sparse in the literature of neural oscillations. While relatively novel in neuroscience, nonsinusoidal oscillations emerge in other physical phenomena with associated methods for addressing these features. For example, the chemical processing industry applies curve-fitting algorithms to identify nonsinusoidal waveforms in control loops.

Future efforts in experimental design, analytical methods development, and computational modeling should explicitly probe how differences in waveform shape relate to differences in physiology. For example, rhythmic stimulation experiments (electric, magnetic, optogenetic, etc.) can vary the stimulating waveform and assess behavioral or physiological differences. Additionally, simultaneous recordings of field potentials and neuronal spiking will help us quantify relationships between waveform shape, synchrony, and other spiking features (see Chapter 3). It may even be possible to move past the sinusoidal assumptions of the Fourier transform and toward more biologically-informed decomposition methods, perhaps consisting of a “dictionary” of neurophysiological basis functions.

The introduction, in part, is an adaptation of the material that appears in: Cole SR, Voytek B. (2017) Brain oscillations and the importance of waveform shape. *Trends in Cognitive Sciences*, 21(2), 137-149. The dissertation author was the primary investigator and author of this paper.

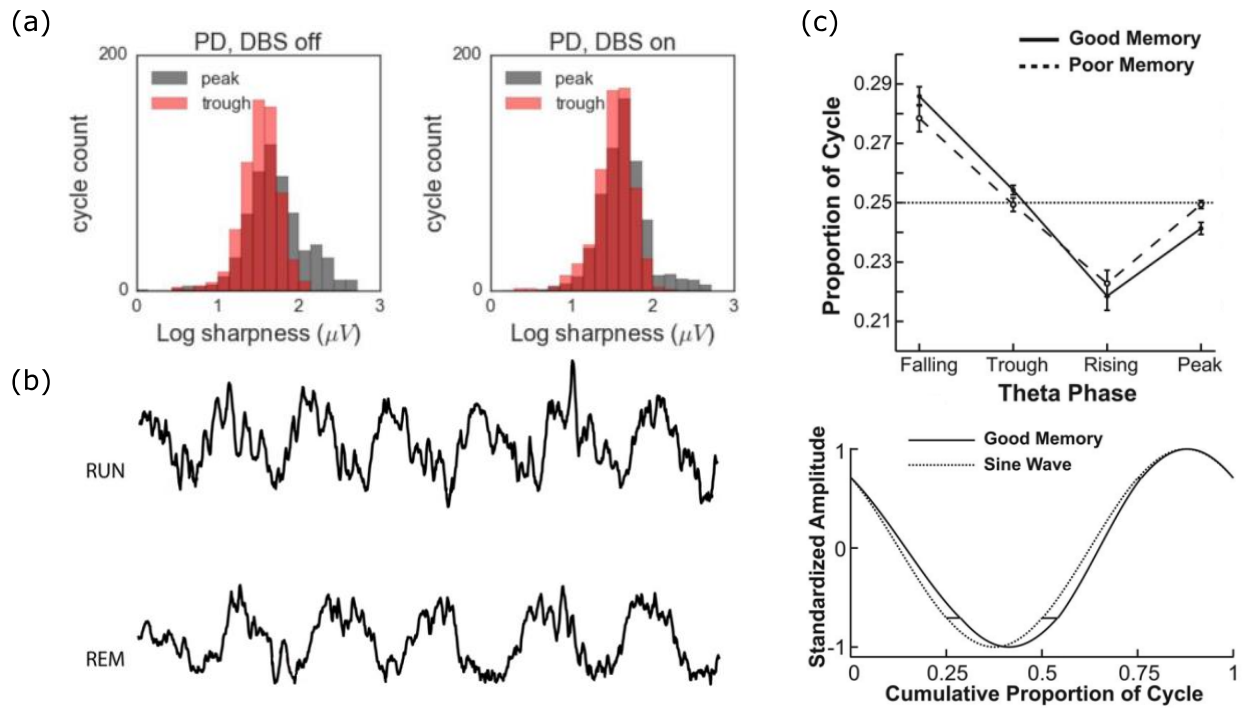


Figure 0.3. Features of oscillatory waveforms relate to behavior and disease. (a) The sharpness of the peaks and troughs of motor cortical beta oscillations were measured in Parkinson's disease (PD) patients. The overlap in peak and trough sharpness distributions is lower in PD patients with an implanted DBS turned off (left) compared to when it is turned on (right). In other words, the sharpness ratio between the peaks and troughs is greater in untreated PD patients, as visualized by a separation in the distributions of peak and trough sharpness. (b) Hippocampal theta oscillations in rats are more asymmetric while the rats are running (top) compared to when the rat is sleeping (bottom). During running, theta oscillations generally have a steeper rise to the peak and a more gradual decay to the trough. (c) Hippocampal theta oscillation symmetry also differed in rats based on memory performance. During a successful encoding period of an object, the theta oscillation was more asymmetric in that its falling phase was extended and its rising phase was shortened.

References

- Abrams R (2002) Electroconvulsive Therapy. Oxford University Press.
- Adrian ED, Matthews BH (1934) The interpretation of potential waves in the cortex. *J Physiol (Lond)* 81:440–471.
- Amiri M, Frauscher B, Gotman J (2016a) Phase-Amplitude Coupling Is Elevated in Deep Sleep and in the Onset Zone of Focal Epileptic Seizures. *Front Hum Neurosci* 10:387.
- Amiri M, Lina J-M, Pizzo F, Gotman J (2016b) High Frequency Oscillations and spikes: Separating real HFOs from false oscillations. *Clin Neurophysiol* 127:187–196.
- Amzica F, Steriade M (1998) Electrophysiological correlates of sleep delta waves. *Electroencephalogr Clin Neurophysiol* 107:69–83.
- Amzica F, Steriade M (2000) Neuronal and glial membrane potentials during sleep and paroxysmal oscillations in the neocortex. *J Neurosci* 20:6648–6665.
- Arroyo S, Lesser RP, Gordon B, Uematsu S, Jackson D, Webber R (1993) Functional significance of the mu rhythm of human cortex: an electrophysiologic study with subdural electrodes. *Electroencephalogr Clin Neurophysiol* 87:76–87.
- Artemenko DP (1973) Role of hippocampal neurons in theta-wave generation. *Neurophysiology* 4:409–415.
- Aru J, Aru J, Priesemann V, Wibral M, Lana L, Pipa G, Singer W, Vicente R (2015) Untangling cross-frequency coupling in neuroscience. *Curr Opin Neurobiol* 31:51–61.
- Belluscio MA, Mizuseki K, Schmidt R, Kempter R, Buzsáki G (2012) Cross-frequency phase-phase coupling between θ and γ oscillations in the hippocampus. *J Neurosci* 32:423–435.
- Berger RJ, Olley P, Oswald I (1962) The EEC, Eye-Movements and Dreams of the Blind. *Q J Exp Psychol (Colchester)* 14:183–186.
- Bland BH, Andersen P, Ganes T, Sveen O (1980) Automated analysis of rhythmicity of physiologically identified hippocampal formation neurons. *Exp Brain Res* 38:205–219.
- Buonviso N, Amat C, Litaudon P, Roux S, Royet J-P, Farget V, Sicard G (2003) Rhythm sequence through the olfactory bulb layers during the time window of a respiratory cycle. *European Journal of Neuroscience* 17:1811–1819.
- Buzsáki G, Buhl DL, Harris KD, Csicsvari J, Czéh B, Morozov A (2003) Hippocampal network patterns of activity in the mouse. *Neuroscience* 116:201–211.
- Buzsáki G, Czopf J, Kondákor I, Kellényi L (1986) Laminar distribution of hippocampal rhythmic

slow activity (RSA) in the behaving rat: current-source density analysis, effects of urethane and atropine. *Brain Res* 365:125–137.

Buzsáki G, Draguhn A (2004) Neuronal oscillations in cortical networks. *Science* 304:1926–1929.

Buzsáki G, Rappelsberger P, Kellényi L (1985) Depth profiles of hippocampal rhythmic slow activity (“theta rhythm”) depend on behaviour. *Electroencephalogr Clin Neurophysiol* 61:77–88.

Buzsáki G, Watson BO (2012) Brain rhythms and neural syntax: implications for efficient coding of cognitive content and neuropsychiatric disease. *Dialogues Clin Neurosci* 14:345–367.

Canolty RT, Knight RT (2010) The functional role of cross-frequency coupling. *Trends Cogn Sci (Regul Ed)* 14:506–515.

Chandran K S S, Mishra A, Shirhatti V, Ray S (2016) Comparison of Matching Pursuit Algorithm with Other Signal Processing Techniques for Computation of the Time-Frequency Power Spectrum of Brain Signals. *J Neurosci* 36:3399–3408.

Clemens Z, Mölle M, Eross L, Barsi P, Halász P, Born J (2007) Temporal coupling of parahippocampal ripples, sleep spindles and slow oscillations in humans. *Brain* 130:2868–2878.

Coenen AML, Van Luijtelaar ELJM (2003) Genetic animal models for absence epilepsy: a review of the WAG/Rij strain of rats. *Behav Genet* 33:635–655.

de Hemptinne C, Ryapolova-Webb ES, Air EL, Garcia PA, Miller KJ, Ojemann JG, Ostrem JL, Galifianakis NB, Starr PA (2013) Exaggerated phase-amplitude coupling in the primary motor cortex in Parkinson disease. *Proc Natl Acad Sci U S A* 110:4780–4785.

Dowsett J, Herrmann CS (2016) Transcranial Alternating Current Stimulation with Sawtooth Waves: Simultaneous Stimulation and EEG Recording. *Front Hum Neurosci* 10:135.

Dvorak D, Fenton AA (2014) Toward a proper estimation of phase-amplitude coupling in neural oscillations. *J Neurosci Methods* 225:42–56.

Fabricius M, Fuhr S, Willumsen L, Dreier JP, Bhatia R, Boutelle MG, Hartings JA, Bullock R, Strong AJ, Lauritzen M (2008) Association of seizures with cortical spreading depression and peri-infarct depolarisations in the acutely injured human brain. *Clin Neurophysiol* 119:1973–1984.

Fontanini A, Katz DB (2005) 7 to 12 Hz activity in rat gustatory cortex reflects disengagement from a fluid self-administration task. *J Neurophysiol* 93:2832–2840.

Fransen AMM, Dimitriadis G, van Ede F, Maris E (2016) Distinct α - and β -band rhythms over rat

somatosensory cortex with similar properties as in humans. *J Neurophysiol* 115:3030–3044.

Fries P (2005) A mechanism for cognitive dynamics: neuronal communication through neuronal coherence. *Trends Cogn Sci (Regul Ed)* 9:474–480.

Fröhlich F, McCormick DA (2010) Endogenous electric fields may guide neocortical network activity. *Neuron* 67:129–143.

Gerber EM, Sadeh B, Ward A, Knight RT, Deouell LY (2016) Non-Sinusoidal Activity Can Produce Cross-Frequency Coupling in Cortical Signals in the Absence of Functional Interaction between Neural Sources. *PLoS ONE* 11:e0167351.

Green JD, Petsche H (1961) Hippocampal electrical activity II. Virtual generators. *Electroencephalogr Clin Neurophysiol* 13:847–853.

Hentschke H, Perkins MG, Pearce RA, Banks MI (2007) Muscarinic blockade weakens interaction of gamma with theta rhythms in mouse hippocampus. *Eur J Neurosci* 26:1642–1656.

Jones SR (2016) When brain rhythms aren't "rhythmic": implication for their mechanisms and meaning. *Curr Opin Neurobiol* 40:72–80.

Klimesch W (1999) EEG alpha and theta oscillations reflect cognitive and memory performance: a review and analysis. *Brain Res Rev* 29:169–195.

Konopacki J, Bland BH, Roth SH (1988) Carbachol-induced EEG "theta" in hippocampal formation slices: evidence for a third generator of theta in CA3c area. *Brain Res* 451:33–42.

Kramer MA, Tort ABL, Kopell NJ (2008) Sharp edge artifacts and spurious coupling in EEG frequency comodulation measures. *J Neurosci Methods* 170:352–357.

Kuhlman WN (1978) Functional topography of the human mu rhythm. *Electroencephalogr Clin Neurophysiol* 44:83–93.

Lee S, Jones SR (2013) Distinguishing mechanisms of gamma frequency oscillations in human current source signals using a computational model of a laminar neocortical network. *Front Hum Neurosci* 7:869.

Leuthardt EC, Schalk G, Wolpaw JR, Ojemann JG, Moran DW (2004) A brain-computer interface using electrocorticographic signals in humans. *J Neural Eng* 1:63–71.

Lewis LD, Weiner VS, Mukamel EA, Donoghue JA, Eskandar EN, Madsen JR, Anderson WS, Hochberg LR, Cash SS, Brown EN, Purdon PL (2012) Rapid fragmentation of neuronal networks at the onset of propofol-induced unconsciousness. *Proc Natl Acad Sci U S A*

109:E3377–E3386.

- Lockmann ALV, Laplagne DA, Leão RN, Tort ABL (2016) A Respiration-Coupled Rhythm in the Rat Hippocampus Independent of Theta and Slow Oscillations. *J Neurosci* 36:5338–5352.
- Louis RP, Lee J, Stephenson R (2004) Design and validation of a computer-based sleep-scoring algorithm. *J Neurosci Methods* 133:71–80.
- Lowet E, Roberts MJ, Bonizzi P, Karel J, De Weerd P (2016) Quantifying Neural Oscillatory Synchronization: A Comparison between Spectral Coherence and Phase-Locking Value Approaches. *PLoS ONE* 11:e0146443.
- Lozano-Soldevilla D, Huurne N Ter, Oostenveld R (2016) Neuronal Oscillations with Non-sinusoidal Morphology Produce Spurious Phase-to-Amplitude Coupling and Directionality. *Front Comput Neurosci* 10:87.
- Mäkinen VT, May PJC, Tiiainen H (2005) The use of stationarity and nonstationarity in the detection and analysis of neural oscillations. *Neuroimage* 28:389–400.
- Massimini M, Huber R, Ferrarelli F, Hill S, Tononi G (2004) The sleep slow oscillation as a traveling wave. *J Neurosci* 24:6862–6870.
- Mazaheri A, Jensen O (2008) Asymmetric amplitude modulations of brain oscillations generate slow evoked responses. *J Neurosci* 28:7781–7787.
- Mazaheri A, Jensen O (2010) Rhythmic pulsing: linking ongoing brain activity with evoked responses. *Front Hum Neurosci* 4:177.
- Mazzoni A, Lindén H, Cuntz H, Lansner A, Panzeri S, Einevoll GT (2015) Computing the Local Field Potential (LFP) from Integrate-and-Fire Network Models. *PLoS Comput Biol* 11:e1004584.
- Merritt HH (1938) A new series of anticonvulsant drugs tested by experiments on animals. *Archives of Neurology & Psychiatry* 39:1003.
- Mölle M, Marshall L, Gais S, Born J (2002) Grouping of spindle activity during slow oscillations in human non-rapid eye movement sleep. *J Neurosci* 22:10941–10947.
- Montgomery SM, Betancur MI, Buzsáki G (2009) Behavior-dependent coordination of multiple theta dipoles in the hippocampus. *J Neurosci* 29:1381–1394.
- Muthukumaraswamy SD, Johnson BW, McNair NA (2004) Mu rhythm modulation during observation of an object-directed grasp. *Brain Res Cogn Brain Res* 19:195–201.
- Ngo H-VV, Martinetz T, Born J, Mölle M (2013) Auditory closed-loop stimulation of the sleep slow oscillation enhances memory. *Neuron* 78:545–553.

- Nikulin VV, Linkenkaer-Hansen K, Nolte G, Lemm S, Müller KR, Ilmoniemi RJ, Curio G (2007) A novel mechanism for evoked responses in the human brain. *Eur J Neurosci* 25:3146–3154.
- Ouedraogo DW, Lenck-Santini P-P, Marti G, Robbe D, Crépel V, Epsztein J (2016) Abnormal UP/DOWN Membrane Potential Dynamics Coupled with the Neocortical Slow Oscillation in Dentate Granule Cells during the Latent Phase of Temporal Lobe Epilepsy. *eNeuro* 3.
- Pavlov AN, Hramov AE, Koronovskii AA, Sitnikova EY, Makarov VA, Ovchinnikov AA (2012) Wavelet analysis in neurodynamics. *Physics-Uspekhi* 55:845–875.
- Pearl PL, LaFleur BJ, Reigle SC, Rich AS, Freeman AAH, McCutchen C, Sato S (2002) Sawtooth wave density analysis during REM sleep in normal volunteers. *Sleep Med* 3:255–258.
- Pfurtscheller G, Brunner C, Schlogl A, Lopes da Silva FH (2006) Mu rhythm (de)synchronization and EEG single-trial classification of different motor imagery tasks. *Neuroimage* 31:153–159.
- Pfurtscheller G, Stancák A, Edlinger G (1997) On the existence of different types of central beta rhythms below 30 Hz. *Electroencephalogr Clin Neurophysiol* 102:316–325.
- Pietersen ANJ, Patel N, Jefferys JGR, Vreugdenhil M (2009) Comparison between spontaneous and kainate-induced gamma oscillations in the mouse hippocampus in vitro. *Eur J Neurosci* 29:2145–2156.
- Pineda JA (2005) The functional significance of mu rhythms: translating “seeing” and “hearing” into “doing”. *Brain Res Brain Res Rev* 50:57–68.
- Pittman-Polletta B, Hsieh W-H, Kaur S, Lo M-T, Hu K (2014) Detecting phase-amplitude coupling with high frequency resolution using adaptive decompositions. *J Neurosci Methods* 226:15–32.
- Polack P-O, Guillemain I, Hu E, Deransart C, Depaulis A, Charpier S (2007) Deep layer somatosensory cortical neurons initiate spike-and-wave discharges in a genetic model of absence seizures. *J Neurosci* 27:6590–6599.
- Ray S, Maunsell JHR (2011) Different origins of gamma rhythm and high-gamma activity in macaque visual cortex. *PLoS Biol* 9:e1000610.
- Salmelin R, Hari R (1994) Spatiotemporal characteristics of sensorimotor neuromagnetic rhythms related to thumb movement. *Neuroscience* 60:537–550.
- Sherman MA, Lee S, Law R, Haegens S, Thorn CA, Hämaläinen MS, Moore CI, Jones SR (2016) Neural mechanisms of transient neocortical beta rhythms: Converging evidence from humans, computational modeling, monkeys, and mice. *Proc Natl Acad Sci U S A*

113:E4885–E4894.

- Siapas AG, Lubenov EV, Wilson MA (2005) Prefrontal phase locking to hippocampal theta oscillations. *Neuron* 46:141–151.
- Sigurdsson T, Stark KL, Karayiorgou M, Gogos JA, Gordon JA (2010) Impaired hippocampal-prefrontal synchrony in a genetic mouse model of schizophrenia. *Nature* 464:763–767.
- Slaght SJ, Paz T, Chavez M, Deniau J-M, Mahon S, Charpier S (2004) On the activity of the corticostriatal networks during spike-and-wave discharges in a genetic model of absence epilepsy. *J Neurosci* 24:6816–6825.
- Somers D, Kopell N (1993) Rapid synchronization through fast threshold modulation. *Biol Cybern* 68:393–407.
- Stam CJ, Pijn JP, Suffczynski P, Lopes da Silva FH (1999) Dynamics of the human alpha rhythm: evidence for non-linearity? *Clin Neurophysiol* 110:1801–1813.
- Steriade M, Contreras D, Curró Dossi R, Nuñez A (1993) The slow (< 1 Hz) oscillation in reticular thalamic and thalamocortical neurons: scenario of sleep rhythm generation in interacting thalamic and neocortical networks. *J Neurosci* 13:3284–3299.
- Tiihonen J, Kajola M, Hari R (1989) Magnetic mu rhythm in man. *Neuroscience* 32:793–800.
- Tort ABL, Fontanini A, Kramer MA, Jones-Lush LM, Kopell NJ, Katz DB (2010) Cortical networks produce three distinct 7–12 Hz rhythms during single sensory responses in the awake rat. *J Neurosci* 30:4315–4324.
- Trimper JB, Stefanescu RA, Manns JR (2014) Recognition memory and theta-gamma interactions in the hippocampus. *Hippocampus* 24:341–353.
- van Dijk H, van der Werf J, Mazaheri A, Medendorp WP, Jensen O (2010) Modulations in oscillatory activity with amplitude asymmetry can produce cognitively relevant event-related responses. *Proc Natl Acad Sci U S A* 107:900–905.
- van Driel J, Cox R, Cohen MX (2015) Phase-clustering bias in phase-amplitude cross-frequency coupling and its removal. *J Neurosci Methods* 254:60–72.
- Vaz AP, Yaffe RB, Wittig JH, Inati SK, Zaghloul KA (2017) Dual origins of measured phase-amplitude coupling reveal distinct neural mechanisms underlying episodic memory in the human cortex. *Neuroimage* 148:148–159.
- Voytek B, Knight RT (2015) Dynamic network communication as a unifying neural basis for cognition, development, aging, and disease. *Biol Psychiatry* 77:1089–1097.
- Weiner RD, Rogers HJ, Davidson JR, Kahn EM (1986a) Effects of electroconvulsive therapy upon brain electrical activity. *Ann N Y Acad Sci* 462:270–281.

- Weiner RD, Rogers HJ, Davidson JR, Squire LR (1986b) Effects of stimulus parameters on cognitive side effects. *Ann N Y Acad Sci* 462:315–325.
- Wiest MC, Nicolelis MAL (2003) Behavioral detection of tactile stimuli during 7-12 Hz cortical oscillations in awake rats. *Nat Neurosci* 6:913–914.
- Womelsdorf T, Valiante TA, Sahin NT, Miller KJ, Tiesinga P (2014) Dynamic circuit motifs underlying rhythmic gain control, gating and integration. *Nat Neurosci* 17:1031–1039.
- Yeh C-H, Lo M-T, Hu K (2016) Spurious cross-frequency amplitude-amplitude coupling in nonstationary, nonlinear signals. *Physica A* 454:143–150.

CHAPTER 1: Nonsinusoidal beta oscillations reflect cortical pathophysiology in Parkinson's disease

Abstract

Oscillations in neural activity play a critical role in neural computation and communication. There is intriguing new evidence that the nonsinusoidal features of the oscillatory waveforms may inform underlying physiological and pathophysiological characteristics. Time-domain waveform analysis approaches stand in contrast to traditional Fourier-based methods, which alter or destroy subtle waveform features. Recently it has been shown that the waveform features of oscillatory beta (13-30 Hz) events—a prominent motor cortical oscillation—may reflect near-synchronous excitatory synaptic inputs onto cortical pyramidal neurons. Here we analyze data from invasive human primary motor cortex (M1) recordings from patients with Parkinson's disease (PD) implanted with a deep brain stimulator (DBS) to test the hypothesis that the beta waveform becomes less sharp with DBS, suggesting that M1 input synchrony may be decreased. We find that, in PD, M1 beta oscillations have sharp, asymmetric, nonsinusoidal features, specifically asymmetries in the ratio between the sharpness of the beta peaks compared to the troughs. This waveform feature is nearly perfectly correlated with beta-high gamma phase-amplitude coupling ($r = 0.94$)—a neural index previously shown to track PD-related motor deficit. Our results suggest that the pathophysiological beta generator is altered by DBS, smoothing out the beta waveform. This has implications not only for the interpretation of the physiological mechanism by which DBS reduces PD-related motor symptoms, but more broadly for our analytic toolkit in general. That is, the often-overlooked time-domain features of oscillatory waveforms may carry critical physiological information about neural processes and dynamics.

Introduction

Oscillatory activity is abundant in electrophysiological recordings in a variety of species, brain regions, and spatial scales (Engel et al., 2001; Buzsáki and Draguhn, 2004; Schnitzler and

Gross, 2005; Buzsáki, 2006). These neural oscillations are critical for efficient communication within and across brain structures (Fries, 2005, 2015; Voytek and Knight, 2015). The vast majority of research examining the relationship between neural oscillations and cognition or disease utilizes Fourier-based methods to filter the signals into semi-arbitrary frequency bands of interest. While powerful, these methods inherently smooth the signal, altering or removing finer temporal features. This is especially striking given the mounting evidence that features of the oscillatory waveform—such as its general shape, sharpness, rise-to-decay symmetry, etc.—may inform underlying physiology (Sherman et al., 2016; Cole and Voytek, 2017). In particular, some cortical oscillations in the beta (13-30 Hz) range have been shown to have characteristic waveforms that are sharper and steeper than a canonical sinusoid (Sherman et al., 2016). Computational modeling suggests these nonsinusoidal features may reflect the temporal synchrony of excitatory input currents onto cortical pyramidal neurons (Sherman et al., 2016), such that a sharper waveform reflects greater synchrony in synaptic input. That is, careful consideration of oscillatory waveform shape may provide critical clues about underlying neurophysiology and neural communication.

We examine the hypothesis that deep brain stimulation (DBS) treatment in patients with Parkinson's disease (PD) changes the waveform shape of beta oscillations in the primary motor cortex (M1), indicating input synchrony to M1 may be altered. Previous reports have associated untreated PD with excessive beta synchronization in the basal ganglia (Brown, 2003). Additionally, recent evidence in M1 has shown increased phase-amplitude coupling (PAC) between beta phase and high gamma (50-200 Hz) amplitude in PD patients (de Hemptinne et al., 2013). This pathologically strong PAC is reduced during DBS (de Hemptinne et al., 2015). This is particularly intriguing, as high gamma amplitude has been shown to index local population firing rate (Mukamel et al., 2005; Ray et al., 2008; Manning et al., 2009; Miller et al., 2009a, 2014). Such exaggerated PAC in PD has been broadly interpreted to represent an

oversynchronization of local spiking in the cortex (de Hemptinne et al., 2015; Voytek and Knight, 2015).

Here we observe that PD patients show a change in beta waveform shape during DBS, in line with the hypothesis that PD is associated with oversynchronized cortical inputs that are ameliorated via DBS. Additionally, the sharpness of a patient's beta oscillations predicted motor rigidity such that sharper beta (more synchronized inputs) was associated with greater rigidity. We extend the previous report showing decreased beta-high gamma PAC in PD patients during DBS, finding that beta waveform sharpness strongly tracks PAC across subjects. While previous reports have shown that sharp transients can lead to "spurious" PAC (Kramer et al., 2008; Tort et al., 2013; He, 2014; Aru et al., 2015; Gerber et al., 2016; Lozano-Soldevilla et al., 2016), we emphasize here that these sharp beta features are not artefactual, in the sense that they are not the apparent result of mechanical or electrical noise. Rather these features may provide novel insights into the physiological processes that generate them, with PAC being one method of detecting sharp waveforms that may reflect oversynchronized inputs. Because qualitatively different waveforms can underlie increased PAC (Vaz et al., 2017), we contend that a more thorough analysis of PAC should include time-domain characteristics in conjunction with spectral features.

Materials & Methods

Note that recordings analyzed in this report are the same as those analyzed in a previous report of 23 PD patients before and during DBS (de Hemptinne et al., 2015).

Data collection

M1 recordings were obtained from 23 PD patients (20 male, 3 female) as previously described (de Hemptinne et al., 2013, 2015; Panov et al., 2016). Patients were recruited at the University of California at San Francisco (UCSF) or the San Francisco Veteran Affairs Medical Center. Patients were diagnosed with idiopathic PD with mild to moderate bradykinesia/rigidity and UPDRS III (Unified Parkinson's Disease Rating Scale part III) scores between 30 and 60.

Patients underwent DBS implantation in the awake state and provided written informed consent. Patients were excluded if they had prominent tremor or peak-to-peak M1 LFP amplitude below 50 microvolts. Data collection was approved by the institutional ethics committees and was in agreement with the Declaration of Helsinki.

Deep Brain Stimulation (DBS) was as previously described (de Hemptinne et al., 2015). T2-weighted magnetic resonance imaging was used to target the STN, with adjustments made based on movement-related spiking activity. Intraoperative computed tomography scans coregistered with preoperative MRI were used to confirm electrode placement of the DBS lead (model 3389 in 17 patients and 3387 in 6 patients; Medtronic, Inc., Minneapolis, Minnesota, USA). An analog neurostimulator (Medtronic model 3625) was used to set therapeutic stimulation parameters. Because optimal stimulation settings were not found prior to recording, an increased voltage (4V) was used for stimulation between the motor territory of STN and its dorsal border. More details on patients and stimulation can be found in the previous reports (de Hemptinne et al., 2013, 2015).

A six-contact subdural electrocorticography (ECoG) strip was placed on the cortical surface using the burr hole for DBS lead placement. The target was the arm area of M1, 3cm from midline and medial to the hand knob. Electrode contacts were platinum with a 4mm total diameter, 2.3mm exposed diameter, and 1cm spacing between contacts (Ad-Tech, Racine, WI). Correct placement of electrodes was confirmed using intraoperative computed tomography merged with preoperative MRI or lateral fluoroscopy. Additionally, physiological confirmation was obtained using median nerve stimulation (frequency = 2 Hz, pulse width = 200 μ s, pulse train length = 160, amplitude = 25–40 mAmp) to evoke somatosensory potentials. The most posterior contact showing a negative N20 waveform was defined as the closest electrode to M1.

Antiparkinsonian medication was stopped 12 hours before surgery. Data were collected 5–60 minutes after lead insertion to minimize the confounding effect of a temporary ‘microlesion’ associated with lead insertion. In bilateral DBS implantation surgeries, brain activity was

recorded on the second side implanted in order to allow more time between the cessation of propofol sedation and the start of ECoG recording. First, data were collected and evaluated after lead insertion, before any stimulation (“before DBS”). Second, data were collected when DBS was turned on for the first time (“during DBS”), before searching for optimal contact and stimulation parameters. Third, ‘after DBS’ data were collected after DBS turned off for several minutes.

Recordings were collected using Alpha Omega Microguide Pro (Alpha Omega, Inc, Nazareth, Israel) or the Guideline 4000 customized clinical recording system (FHC Inc, Bowdoin, ME) with a sampling rate between 1000 Hz and 3000 Hz. A needle electrode in the scalp was used as the ground. Signals were band-pass filtered 1–500 Hz and amplified 7000x. While the analyzed data was collected, subjects were relaxing with eyes open, fixating on a point approximately 1 meter away. The first 30 seconds of data without obvious electrical noise or movement were selected for analyses.

Data pre-processing

Data was processed in the same way as previously reported (de Hemptinne et al., 2013, 2015). Recordings were referenced using a bipolar montage in which each channel was referenced to the immediately anterior channel. Data were downsampled to 1000 Hz. Line noise was removed with a notch filter between 58 Hz and 62 Hz (Butterworth, order = 3). Additionally in this paper, all signals were cleaned of high frequency artifacts by low-pass filtering at 200 Hz (FIR filter, window method, order = 250ms) and applying narrowband notch filters (Butterworth, order = 3) to remove any sharp peaks in power spectra above 80 Hz caused by DBS stimulation and electronic noise. The same filters were applied to all recordings from the same subject (before DBS and during DBS).

Oscillation sharpness

The procedure for estimating the sharpness of beta oscillations is illustrated in Figure 1.1A-B and begins with finding oscillatory peaks and troughs. First, the raw voltage trace is

band-pass filtered using an FIR filter (window method, cutoff frequencies = 13 and 30 Hz, order = 231ms). Time points of rising and falling zero-crossings are identified. Returning to the raw signal, the time point of maximal voltage between a rising zero-crossing and a subsequent falling zero-crossing is defined as the peak. Similarly, the time point of minimal voltage between a falling zero-crossing and a subsequent rising zero-crossing is defined as a trough. Sharpness of each peak and trough is defined in Equation 1 in which V_{peak} is the voltage at the oscillatory peak and $V_{peak-5ms}$ and $V_{peak+5ms}$ correspond to the voltage 5ms before and after the peak, respectively.

$$Sharp_{peak} = \frac{(V_{peak} - V_{peak-5ms}) + (V_{peak} - V_{peak+5ms})}{2} \quad (1)$$

Trough sharpness is calculated in the same manner. Intuitively, extrema sharpness increases as the absolute voltage difference between the extrema and the surrounding time points increases. While 5 ms is chosen as the temporal width to quantify sharpness, results are similar for other choices of sharpness width (data not shown).

The mean sharpness throughout a recording is calculated for peaks and troughs separately (around 600 each in each 30 second recording). The reported sharpness ratio metric is the ratio of the sharpness of the two extrema, such that the ratio is always greater than 1 as in Equation 2.

$$\text{sharpness ratio} = \max\left(\frac{\frac{1}{N_{peaks}} fSharp_{peak}}{\frac{1}{N_{troughs}} fSharp_{trough}}, \frac{\frac{1}{N_{troughs}} fSharp_{trough}}{\frac{1}{N_{peaks}} fSharp_{peak}}\right) \quad (2)$$

This ratio accounts for differences in the amplitudes across subjects that can be caused by variance in electrode conductance. Note in Figure 1.2 that this ratio is not fixed to be greater than 1, but rather mean peak sharpness is divided by mean trough sharpness.

Oscillation steepness

Steepness of the rises and decays of each oscillation is calculated using the peaks and troughs identified as described above. For rise steepness, the time series of interest is the raw voltage between each trough and the subsequent peak as in Equation 3.

$$steepness_{rise} = \max(|V(t+1) - V(t)|, t_{trough} \leq t \leq t_{peak}-1) \quad (3)$$

The maximum value of the instantaneous first derivative (`numpy.diff`) of this signal is defined as the steepness for this single rise period. The steepness of decay periods are similarly calculated using the raw voltage time series between each peak and the subsequent trough. The average rise and decay steepness is calculated for each recording across all rise and decay periods. A steepness ratio is then calculated for each recording by dividing the average steepness for all rises/decays by the average steepness for all decays/rises (such that the ratio is greater than 1) as in Equation 4. Note in Figure 1.2, this ratio is not fixed to be greater than 1, but rather rise steepness is divided by decay steepness.

$$steepness\ ratio = \max\left(\frac{steepness_{decays}}{steepness_{rises}}, \frac{steepness_{rises}}{steepness_{decays}}\right) \quad (4)$$

Specific code for the novel metrics introduced, along with tutorials, is available at <https://github.com/voytekresearch/misshapen>.

Spectral analysis

The power spectrum of a signal is calculated by squaring the absolute value of its Fourier transform (`numpy.fft.fft`). Beta power (Fig. 1.5) is calculated for each 30-second signal by summing the coefficients in the power spectrum in the beta frequency range (13-30 Hz). Spectrograms of signals (Fig. 1.4E) are calculated using a continuous wavelet transform (7-cycle complex Morlet wavelets 1 Hz to 200Hz with a 1Hz step size, `scipy.signal.morlet` with `s=0.5`). Beta frequency for each recording is estimated by counting the number of peaks identified as described above and dividing by the duration of the recording.

The beta and high gamma components of the signal are obtained by using FIR filters (window method, `scipy.signal.firwin`). Two-pass zero-phase filtering is performed with these filters (`scipy.signal.filtfilt`). Filter orders are chosen in order to obtain both a desirable frequency response and reasonable temporal resolution. Beta band-pass filters have cutoff frequencies 13 Hz and 30 Hz and an order of 231ms. High gamma band-pass filters have cutoff frequencies 50 Hz and 200 Hz and an order of 240ms. Amplitude of the high gamma component (Fig. 1.6A,B) is calculated by the magnitude of its Hilbert transform. The high gamma amplitude is sampled at the peaks and troughs in each beta oscillation (Fig. 1.4B).

Statistical PAC is estimated using the normalized modulation index metric (Ozkurt and Schnitzler, 2011). PAC was estimated using the open-source package, `pacpy`, available at <https://github.com/voytekresearch/pacpy>. The high gamma amplitude is calculated as described above. The beta phase is similarly calculated by the angle of the Hilbert transform of this component. Results are similar when applying four alternative metrics of statistical PAC (Canolty et al., 2006; Penny et al., 2008; Tort et al., 2010), or when a comodulogram method is used as in the previous report (de Hemptinne et al., 2015) (data not shown). The preferred phase of coupling for each recording (Fig. 1.3G) is determined by the angle of the circular sum of the instantaneous beta phase, weighted by the instantaneous high gamma amplitude.

Comodulograms (Fig. 1.3A-B and Fig. 1.6C-D) are calculated similar to the previous report (de Hemptinne et al., 2015). The frequency range for the phase-providing oscillation ranges from 6 Hz to 40 Hz with a step size and bandwidth of 2 Hz. For the amplitude-providing oscillation, the frequency ranges from 20 Hz to 200 Hz with a step size and bandwidth of 4 Hz. At each frequency step, a 7-cycle complex Morlet wavelet is used as a bandpass filter, and either the instantaneous angle or magnitude of the filtered signal is calculated in order to extract phase or amplitude time series, respectively. The modulation index method (Tort et al., 2010) is used to quantify statistical PAC between each combination of filtered signals in the comodulogram.

Statistical PAC histograms (Fig. 1.3D-F) are calculated from the beta phase time series and high gamma amplitude time series used to calculate statistical PAC. The high gamma amplitude is then averaged across 10 equally-sized bins of beta phase. A similar phase estimate as described previously (Siapas et al., 2005; Belluscio et al., 2012; Trimper et al., 2014) is applied to account for the nonsinusoidal shape of neural oscillations. Time points of peaks and troughs are identified as in the “Oscillation Sharpness” section above. The time points of these extrema are then used to linearly interpolate a theoretical phase value for each sample.

Analysis of individual beta cycles is performed by separating the cycles trough-to-trough or peak-to-peak using the extrema found as described above. The sharpness of each cycle is measured and they are split into 5 groups based on this value in order to compare extrema-locked high gamma amplitude (Fig. 1.4C) or statistical PAC (Fig. 1.4D). In Fig. 1.5C, the sharpness ratio between each trough and subsequent peak is correlated with the voltage difference between these two extrema.

In order to visualize potential coupling between beta and gamma oscillations, event-related averages of the raw data (Fig. 1.4F) were calculated by triggering on the peaks of the high gamma component (obtained with the filter described above). High gamma peaks were only used as triggers if the amplitude at that time point was in the top 10th percentile, in order to limit triggering during periods with negligible high gamma power in which the peak phase is essentially random.

Generation of canonical asynchronous PAC

A canonical signal with beta-high gamma asynchronous PAC (Fig. 1.6B) is simulated in three steps: 1. A beta oscillation is simulated by band-pass filtering 30 seconds of white noise with a band-pass FIR filter (13-30 Hz). 2. High gamma is similarly simulated by band-pass filtering 30 seconds of white noise with a 50-200 Hz band-pass FIR filter. The amplitude of the high gamma is then modulated by the beta phase by multiplying its time series by $(1 - \text{abs}(\phi_\beta)/\pi)$

and scaling by 0.03 in order to decrease its amplitude relative to the simulated beta oscillation.

3. The beta oscillation and high gamma components are added together.

Statistics

The Scipy package (v 0.16.0) in Python (v 2.7) is used for all statistical analysis. Unless indicated otherwise, all correlations are Pearson and all p-values are two-tailed.

Results

M1 beta oscillations in PD are flattened by DBS

To quantify beta waveform shape, peaks and troughs were first identified throughout each 30-second recording (Fig. 1.1A, Materials & Methods). After locating the extrema, the sharpness of each peak and trough was quantified (Fig. 1.1B, Materials & Methods). Importantly, the metric we use for extrema sharpness is higher for oscillations with sharp transients, e.g., sawtooth waves, compared to sinusoids. The symmetry in the sharpness of oscillatory peaks and troughs is visualized by the degree of overlap in the distributions of sharpness over all extrema in the signal (Fig. 1.1C-D) and is quantified as the “sharpness ratio.” We find that DBS treatment decreases sharpness ratio in PD patients (Fig. 1.1E, paired *t*-test, $t_{22} = 2.5$, $p = 0.019$), and thus, asymmetrically affects peak and trough sharpness. Furthermore, PD patients’ clinical rigidity scores before DBS positively correlate with sharpness ratio (Fig. 1.1F, Spearman $r = 0.54$; $n = 23$; $p = 0.014$). However, the changes in rigidity score and sharpness ratio do not correlate with each other (Spearman $r = 0.17$; $n = 23$; $p = 0.48$).

Differences in sharpness ratio can be caused by increases and/or decreases in the sharpness of one or both extrema. Here, we find that the average sharpness of peaks and troughs decrease with DBS application (paired *t*-test, $t_{45} = 2.4$, $p = 0.027$). Additionally, the extrema sharpness itself does not correlate with the clinical rigidity score (Spearman correlation, $r = -0.17$, $p = 0.49$), indicating it is the *ratio* of peak to trough sharpness that is changed after DBS, and not their sharpness in general.

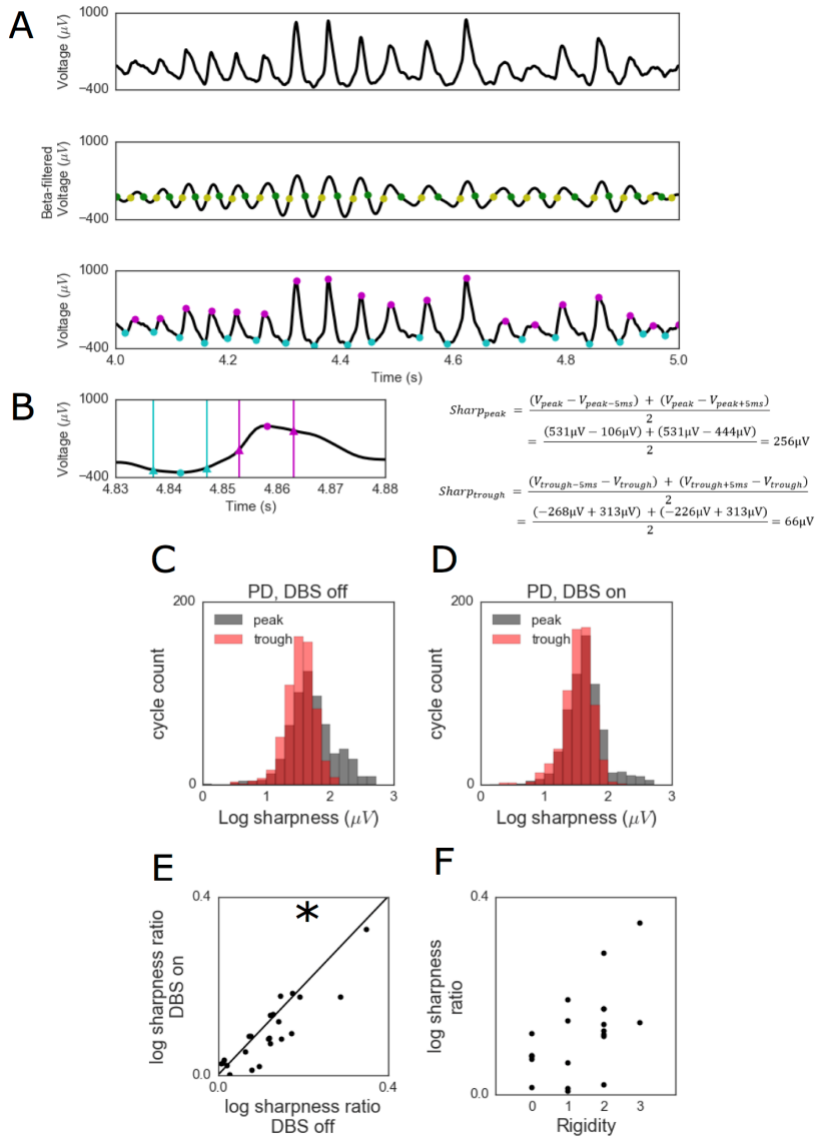


Figure 1.1. Waveform shape of M1 beta oscillation changes in PD. (A) Estimation of beta oscillatory extrema. Row 1: A raw voltage signal. Row 2: The raw voltage is bandpass-filtered in the beta frequency range in order to identify rising phases (yellow dots) and falling phases (green dots). Row 3: In between each rise and decay, peaks (purple circles) and troughs (teal circles) are identified in the raw voltage signal. (B) Sharpness of each extrema is calculated as shown by the formulas on the right. The extrema sharpness is the average voltage difference between the extrema and the voltage at 5ms before and after the extrema. These time points are indicated by teal vertical lines around the trough and purple vertical lines around the peak. Notice that the voltage +/- 5ms around the trough is around the same as the trough voltage (blue triangles and circle), and the voltage +/- 5ms around the peak changes more (purple triangles, relative to purple circle). (C-D) Distributions of peak and trough sharpness across a 30-second recording for a PD patient (C) before and (D) during DBS and (E) the same patient during DBS. (E) The sharpness ratio (between peak sharpness and trough sharpness) is decreased by DBS. (F) Clinical rigidity scores are positively correlated with sharpness ratio in PD patients before DBS. Each dot represents 1 patient in panels E and F. * indicates $p < 0.05$.

M1 beta has a consistent sawtooth-like waveform

To characterize the waveform of M1 beta, we additionally compute a steepness ratio, similar to the sharpness ratio, across subjects. The steepness ratio quantifies the asymmetry between the steepness of the rise and the steepness of the decay period within a beta cycle (see Materials & Methods). Across recordings, steepness ratio is strongly correlated with sharpness ratio (Fig. 1.2A, $r = 0.84$, $p < 10^{-12}$). That is, beta oscillations whose peaks are sharper than their troughs have rise phases that are steeper than their decay phases (Fig. 1.2B, top right). In contrast, oscillations whose troughs are sharper than their peaks have decay phases that are steeper than their rise phases (Fig. 1.2B, bottom left). Example recordings from two PD patients before DBS show these sawtooth-like waveform shapes in raw data (Fig. 1.2C). The neural dynamics in M1 seem to produce field potentials that have a consistent sawtooth-like waveform in which the extremum following a steep voltage change is sharper than the extremum preceding the steep voltage change.

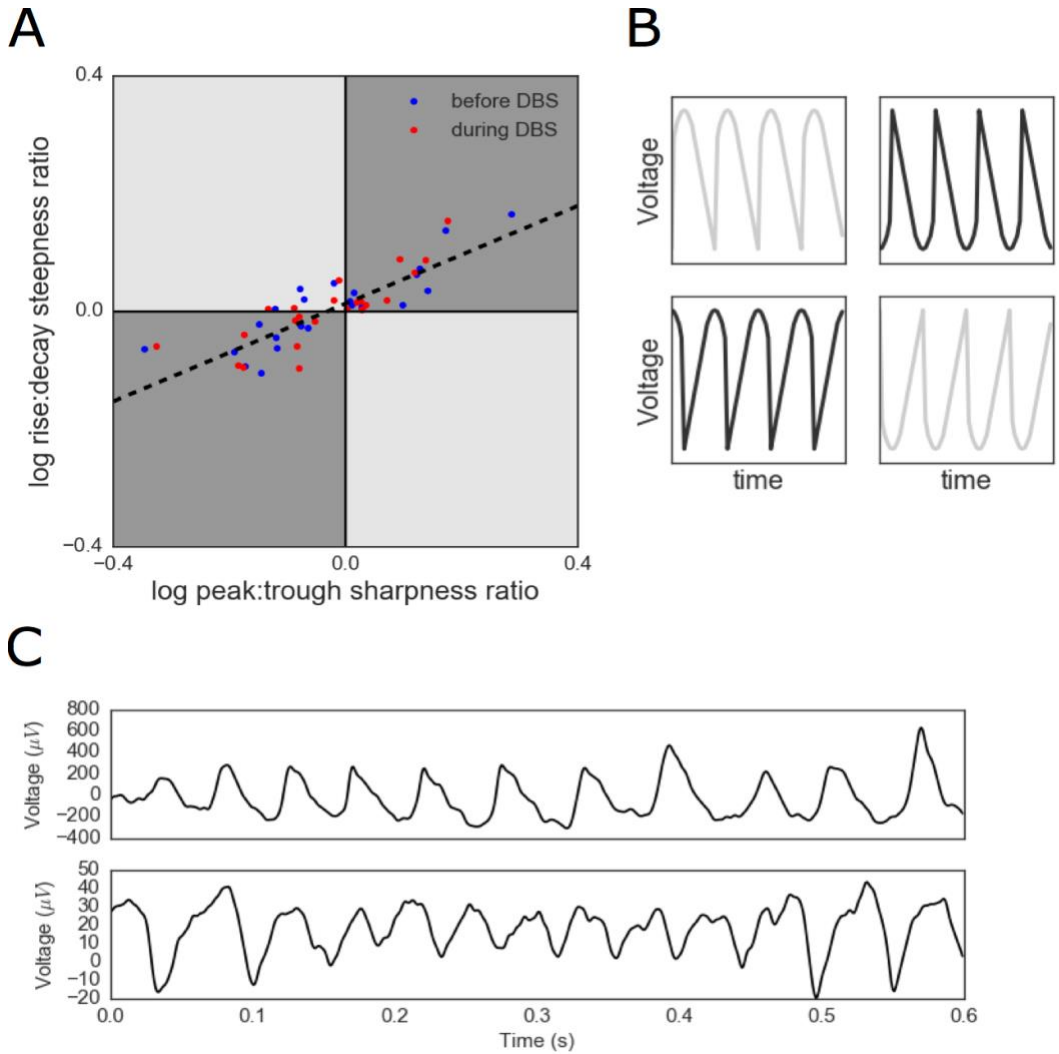


Figure 1.2. M1 beta oscillations have a consistent sawtooth shape. (A) Positive correlation between the relative sharpness of a patient's oscillatory peaks and the relative steepness of a patient's voltage rises. Each marker represents the average sharpness and steepness in a 30-second recording from a PD patient either before DBS (blue) or during DBS (red). (B) Schematic voltage traces corresponding to each quadrant of (A). M1 beta falls in the gray quadrants (quadrants I and III) of this two-dimensional space. (C) Example voltage traces from 2 PD patients corresponding to the sawtooth waveforms in quadrants I and III. These waveform shapes are consistent with the dark gray, but not the light gray, sawtooth shapes in panel B.

Beta oscillation sharpness increases statistical PAC

Previous work showed that beta-high gamma PAC is also changed by DBS application (de Hemptinne et al., 2015), and additionally showed that PAC in PD patients was higher relative to epilepsy and cervical dystonia patients (de Hemptinne et al., 2013). In the following, we extend these findings by relating PAC to sharpness ratio. This is interesting, because the relation of these past results to waveform shape can lead to novel hypotheses regarding the relevant pathophysiological processes in PD (Cole and Voytek, 2017). Due to recent reports (Gerber et al., 2016; Lozano-Soldevilla et al., 2016; Vaz et al., 2017), we make it explicit that our measure of PAC is agnostic to the type of processes that generates it; we will refer to it as statistical PAC in the remainder. Importantly, we reiterate that this by no means indicates that the PAC we quantify is *artefactual* (*i.e.*, due to non-brain sources), only that it can reflect multiple generative mechanisms within the brain. The statistical relationship between these two frequency bands is true, though the common physiological interpretation of two coupled processes differs from the interpretation as changes in waveform sharpness.

First, we show that M1 beta-high gamma statistical PAC was decreased during DBS application, following previous reports. The comodulograms for 1 example patient (Fig. 1.3A,B), shows higher coupling between beta phase and broadband high gamma amplitude before DBS compared to during DBS. In general, DBS application to PD patients decreases the statistical PAC (Fig. 1.3C, paired *t*-test, $t_{45} = 2.7$, $p = 0.013$), as previously reported. We newly observe that, in general, high gamma amplitude is specifically coupled to the peaks and troughs of the beta oscillations, as opposed to non-extrema phases of the beta cycle (such as the rise or decay periods of the oscillation). This is shown for three example PD patients before DBS, with the strongest high gamma at the peak (Fig. 1.3D), trough (Fig. 1.3E), or both (Fig. 1.3F), and for all PD patients in Fig. 1.3G. This pattern of increased PAC at peaks and troughs is statistically observed as a positive correlation between the modulation index and the absolute value of the cosine of the preferred phase (Spearman correlation, $r = 0.58$, $n = 23$, $p = 0.003$).

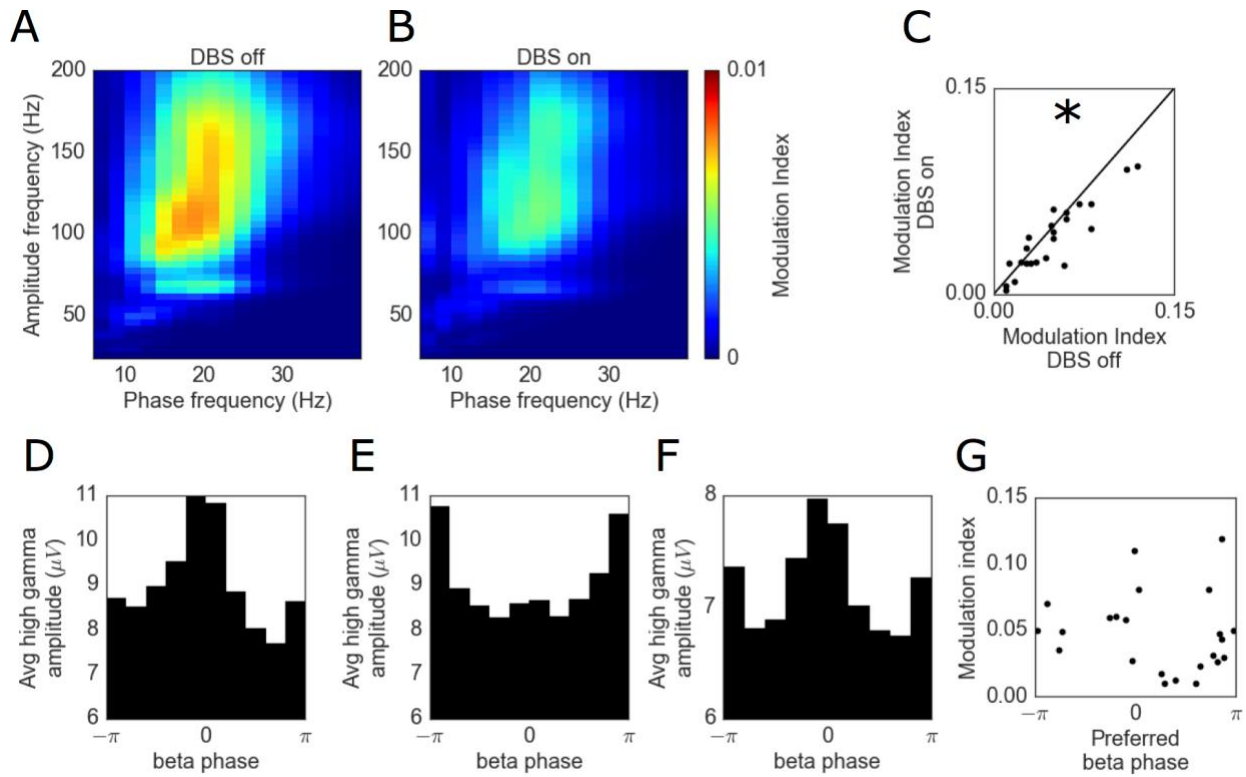


Figure 1.3. Estimates of phase-amplitude coupling in PD. (A) Comodulogram showing estimated beta-high gamma PAC in an example PD patient before DBS. (B) The estimated PAC decreases with DBS application. (C) PD patients decrease in estimated PAC with DBS application. (D-F) Distributions of high gamma amplitude as a function of beta phase for 3 example PD patients showing increased high gamma amplitude at the (D) peak of the beta oscillation, (E) trough of the beta oscillation, and (F) both extrema of the beta oscillation. (G) High estimated PAC is observed specifically in recordings in which the high gamma amplitude is increased around the peak (phase = 0) or trough (phase = $-\pi, \pi$). Each dot represents 1 patient in panels C and G. * indicates $p < 0.05$.

We now extend the above by presenting a converging sequence of results that shows the extrema sharpness of beta waveforms is strongly related to statistical PAC (Fig 4), providing strong evidence that sharpness is the main contributor to phase-locked high gamma. First, we find that the sharpness ratio of beta oscillations is strongly correlated with beta-high gamma statistical PAC across PD patients before DBS (Fig. 1.4A, $r = 0.94$, $p < 10^{-10}$) and during DBS ($r = 0.89$, $p < 10^{-7}$). The remaining results are illustrated for one representative subject before DBS (Fig 4B-F), and similar results were obtained in all other recordings. Second, we find a positive correlation between extrema sharpness and high gamma amplitude at that extrema (Fig. 1.4B). The correlation between these features is similar for both peaks and troughs. Third, providing a time-resolved view of the above, the strength of high gamma amplitude increases as a function of extrema sharpness (Fig. 1.4C). Fourth, the strength of phase-locking of high gamma amplitude across the beta cycle increases as a function of extrema sharpness (Fig. 1.4D). This is known to be the case when PAC is driven by sharp temporal features (He, 2014). Note that the asymmetry in high gamma amplitude around the beta peak (phase 0) indicates stronger high gamma amplitude in the rise phase of the beta oscillation relative to its decay phase. This follows from the sawtooth-like shape of the beta oscillations (quadrants 1 and 3 of Fig. 1.2B), in that high frequency sinusoids are necessary to reconstruct steep voltage rises. Fifth, we show a time-frequency representation of amplitude (Fig 4E) for an example burst of beta oscillations (white trace, peaks numbered) of varying sharpness (values printed above plot). We observe that the high frequency amplitude is strongest (highest PAC) for the sharper peaks (peaks 2, 3, 4, and 6), and weakest (lowest PAC) at the smoother peaks (peaks 1 and 5). Sixth, and finally, we show an event-related average triggered on the peaks of the high gamma component (see Materials & Methods). This is a common type of visualization for PAC. Typically, in the case of two coupled oscillations, this reveals a waveform in which the high frequency oscillation appears around $t=0$, together with the low-frequency oscillation at an offset matching the phase of the statistical PAC (Tort et al., 2013). However, in Fig. 1.4F we do not observe a high frequency

oscillation, but rather see a sharp voltage transient, as would be expected from a sawtooth-like waveform (Tort et al., 2013).

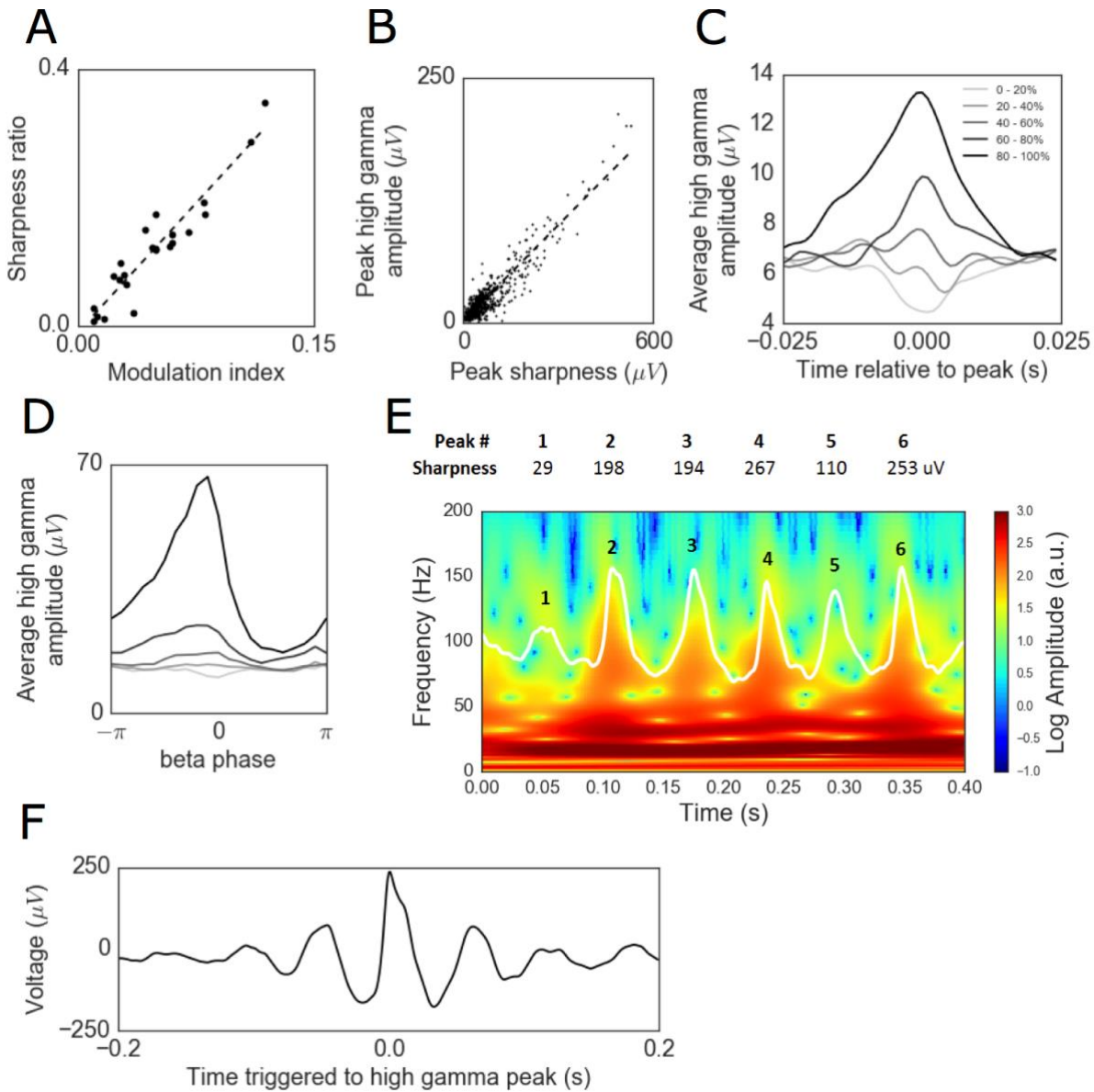


Figure 1.4. Sharp beta oscillations yield phase-locked high gamma amplitude. (A) Sharpness ratio is highly correlated with estimated PAC across all subjects before DBS. (B-F) Illustration of the relationship between extrema sharpness and phase-locked high gamma amplitude for an example PD patient before DBS. (B) Extrema sharpness is positively correlated with the high gamma amplitude at the extrema. (C) High gamma amplitude is locked to the peak of beta oscillations specifically for the sharpest beta oscillations. Beta cycles were split into 5 groups based on the peak sharpness. The line color varies from the least sharp beta cycles (light gray) to the sharpest beta cycles (black). (D) The distribution of high gamma amplitude as a function of beta phase is uniform for beta cycles with low sharpness (light gray) and nonuniform for sharp beta cycles. (E) Spectrogram of a 400ms period of raw voltage recording exhibiting beta oscillations. The sharpest beta oscillations (peaks 2, 3, 4, and 6) have increased amplitude in the high gamma frequency range compared to the cycles with lower sharpness (peaks 1 and 5). (F) Event-related average of raw voltage triggered at the peaks of high gamma oscillations (with the top 10% of amplitude).

Caveats of the relation between waveform sharpness and statistical PAC

A positive correlation between sharpness ratio and statistical PAC could be caused by sharp, phase-locked high gamma rhythms, instead of the sharpness of beta oscillations highlighted above. To gain more certainty that sharpness came from beta instead of high gamma, sharpness ratio was re-calculated on data that was low-pass filtered at 50 Hz (FIR filter, window method, order = 250ms). This removes the high gamma component used to estimate PAC (Fig. 1.5A). This new sharpness ratio measure (after low-pass filtering) is still correlated with the statistical PAC computed prior to low-pass filtering (Fig. 1.5B, $r = 0.80, p < 10^{-5}$). Note that some decrease in correlation strength (in this case, $r = 0.94$ to 0.80) is expected, since sharp extrema are (by definition) broadband in their spectrum, and are necessarily flattened by the 50Hz low-pass filter. Crucially, although the beta waveform is only mildly affected by the low-pass filter, the high gamma fluctuations are suppressed to the level of noise floor of the amplifier. This makes it extremely unlikely that any residual high gamma fluctuations cause a correlation, let alone one of $r = 0.80$. As such, the correlation provides strong evidence that the sharpness measures are not influenced by high gamma fluctuations, but instead originated from the shape of the beta waveform.

In our approach, the sharpness is calculated at each beta cycle throughout the recording, even if no beta oscillation is evident in the raw voltage. One concern with this approach is that noise in a regime of low beta amplitude could cause spurious results in waveform analysis. In order to test for this potential confound, we restrict our analysis to only the cycles in the top 10% of beta amplitude for each recording. The main results still hold under this control analysis: 1) there is a decrease in sharpness ratio with DBS application (paired t -test, $t_{22} = 2.6, p = 0.015$), and; 2) there is a strong correlation between sharpness ratio and PAC ($r = 0.84, p < 10^{-6}$).

Because sharpness ratio is calculated using the raw electrophysiological signal of each extremum and two samples (sampled at 1 kHz) around it, it is worth noting that 90% of the

variance in statistical PAC is captured by only using about 12% of the data (6 samples per period which contains around 50 samples). However, sharpness ratio is not the only dimension of shape that correlates with statistical PAC, as many other waveform features determine the precise Fourier decomposition (such as steepness ratio). Sharpness ratio and steepness ratio both individually correlate with statistical PAC after holding the other metric constant (partial correlations, sharpness ratio: $r = 0.70$, $p = 0.0002$; steepness ratio: $r = 0.44$, $p = 0.034$) and together explain 93% of the variance in statistical PAC of PD patients before DBS.

Another potential caveat in the analysis of waveform sharpness is that increases in beta frequency could underlie increases in the sharpness, as a shorter cycle of the same amplitude is necessarily sharper. However, this is likely not the case, as we find no effect of DBS on the beta frequency in PD patients (paired t -test, $t_{22} = -0.84$, $p = 0.41$, see Materials & Methods). Note that power does not confound the sharpness ratio measure because multiplicative scaling of a waveform to increase its power would have no effect on the sharpness ratio.

Beta oscillation asymmetry correlates with power

During visual inspection of the raw data, high-power beta oscillations seemed to be more asymmetric (*i.e.*, higher sharpness ratio) compared to low-power beta oscillations. If true, this trend could provide additional insight into the physiological process generating beta oscillations. We quantified this trend by correlating the sharpness ratio of an individual cycle with the peak-to-trough amplitude of that cycle. In order to avoid confounding the results with periods of no beta oscillatory activity, only cycles in the top 10th percentile of peak-to-trough amplitude for each recording were analyzed. Across recordings before and during DBS, there is a consistent subject-by-subject positive correlation between the amplitude of a cycle and its sharpness ratio (Fig. 1.5C, one-sample t -test, $t_{45} = 6.10$, $p < 10^{-6}$).

Because beta power is positively correlated with both sharpness ratio (Fig. 1.5C) and statistical PAC (Fig. 1.5D, $r = 0.37$, $p = 0.011$), it could be the case that the correlation between waveform shape and statistical PAC is merely due to a common power bias. However, this is

likely not the case, as sharpness ratio is still correlated with statistical PAC after holding beta power constant (Fig. 1.5E, partial correlation, $r = 0.87$, $p < 10^{-7}$). Additionally, we note that the average power spectra are similar before and during DBS (Fig. 1.5F), and so it is unlikely that the changes in waveform shape and statistical PAC with DBS are merely due to changes in narrowband power.

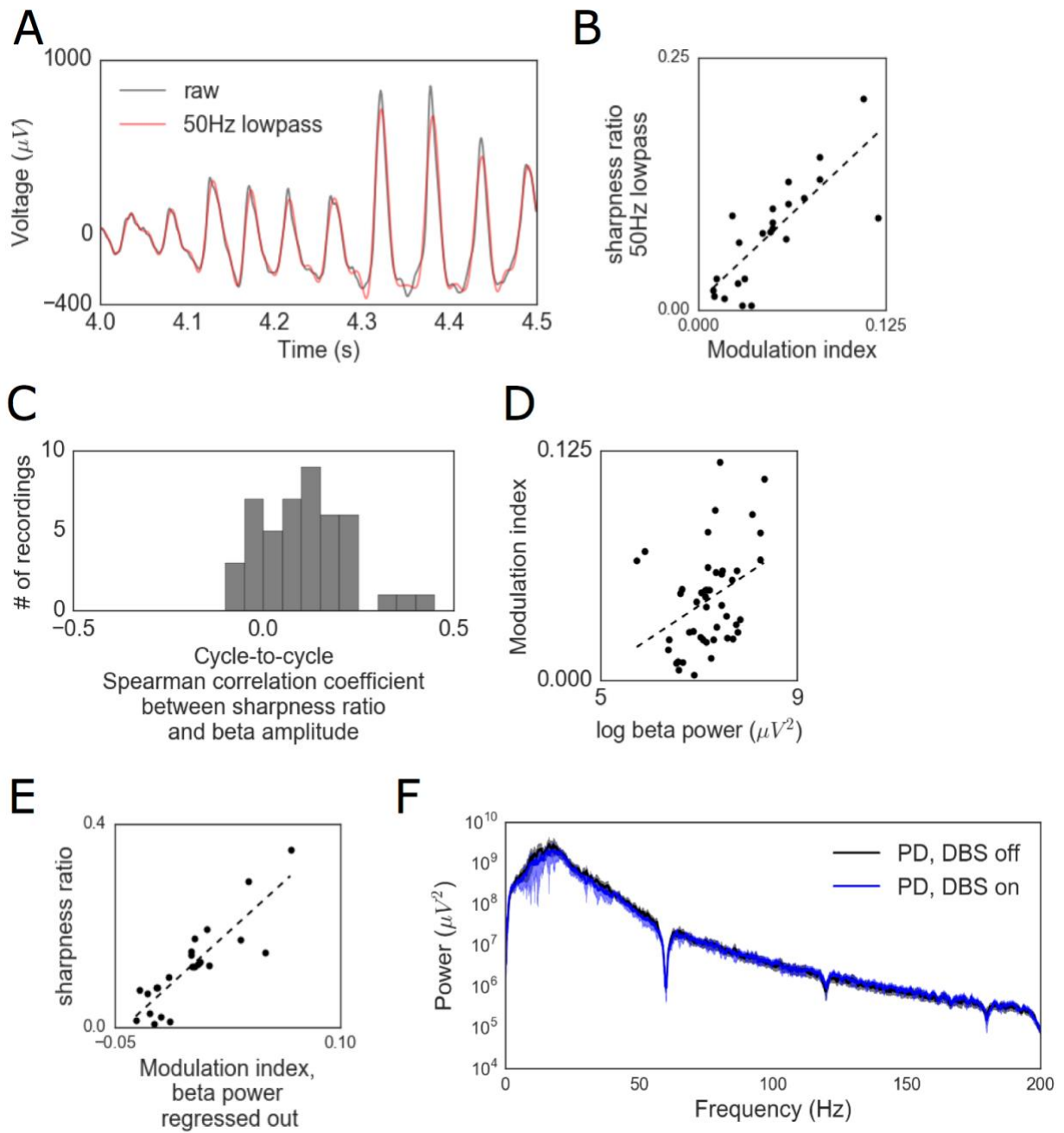


Figure 1.5. Power spectral properties of motor cortical recordings and relation to estimated phase-amplitude coupling. (A) A 50 Hz lowpass filter was applied to attenuate high gamma power. (B) When extrema sharpness was re-calculated on these lowpass-filtered signals, there remained a strong positive correlation with statistical PAC in the original signal. (C) Histogram of correlation coefficients between sharpness ratio and amplitude across all beta cycles in a recording. Each count is one 30-second recording. (D) There is a positive correlation between estimated PAC and beta power. (E) A strong positive correlation between sharpness ratio and estimated PAC (modulation index) remains even after beta power is regressed out. (F) Average power spectra across all subjects before (black) and during DBS (blue), shaded region shows 1 SEM. Each dot represents 1 30-second recording in panels B, D and E.

Discussion

Increased sharpness ratio in motor cortical beta oscillations in Parkinson's Disease

Though beta oscillations are a normal feature of the basal ganglia-thalamocortical loop, PD is associated with excessive neuronal synchronization in the beta frequency band (Kuhn et al., 2005; Moran et al., 2008). Despite an established relationship between beta band neuronal synchronization and PD, the physiological mechanism causing PD-related motor dysfunction has been unclear. However, the recent reports showing that statistical PAC is pathologically strong in PD hypothesize that this overcoupling impairs information flow and in turn causes motor dysfunction (de Hemptinne et al., 2013). Specifically, PD is associated with an increase in beta-high gamma statistical PAC in M1 (de Hemptinne et al., 2013, 2015; Kondylis et al., 2016). Similarly, elevated alpha-high gamma statistical PAC has been observed in the sensorimotor cortex of essential tremor patients (Kondylis et al., 2016). These observations have been critical given that oscillatory coupling, and specifically PAC, is thought to be crucial for the control of information flow in human cortex (Fries, 2005; Canolty et al., 2006; Peterson and Voytek, 2015; Voytek and Knight, 2015; Voytek et al., 2015).

We confirm and extend the previous report of exaggerated statistical PAC in PD by analyzing oscillation shape, given the recent reports that oscillation waveform shape may provide information about their physiological generators (Sherman et al., 2016; Cole and Voytek, 2017). Specifically, recent modeling work suggests that cortical beta waveform sharpness may index the degree of synchrony of input onto cortical pyramidal cells (Sherman et al., 2016). Therefore, here we leveraged analytic approaches on time series to test the hypothesis that beta waveform sharpness is decreased by DBS, suggesting that the synchrony of synaptic input to M1 is decreased. For M1, synchronous bursts of distal excitatory input may reflect the previously reported increase in beta synchrony in the basal ganglia (Sharott et al. 2005; Mallet et al. 2008a; Mallet et al. 2008b; Devergnas et al. 2014). Just as exaggerated PAC has been hypothesized to overwhelm neural processing, too much synchrony consumes an

excessive amount of “neural bandwidth” (Reyes, 2003; Rossant et al., 2011; Brette, 2012; Börgers et al., 2014), hampering, rather than enhancing, neural communications. Given how potent synchronous activity can be in driving downstream population spiking (Reyes, 2003; Wang et al., 2010; Rossant et al., 2011), we suggest that excessive synchrony in M1 may be key to understanding PD pathology. Therefore, our results support previous hypotheses that DBS reduces PD-related movement symptoms by decorrelating the excessively synchronized neural activity in the basal ganglia-thalamocortical loop (Rubin and Terman, 2004; Moran et al., 2012; Wilson, 2013; Voytek and Knight, 2015). Notably, the reported change in waveform shape with DBS leads to a similar interpretation as the decrease in estimated PAC. However, the critical difference between these two interpretations is that the former invokes a modification of a single process whereas the latter invokes a decrease in coupling between two processes.

We note that the higher power beta oscillations tend to be the most asymmetric in terms of extrema sharpness (Fig. 1.5C). If the beta waveform reflects the strength and synchrony of the afferent synaptic currents, as reasoned above, this trend may reflect that beta periods with the strongest synaptic input also have the most synchronous input.

The current description of nonsinusoidal waveforms in motor cortex is reminiscent of previously described mu rhythms. Mu rhythms are arch-shaped (i.e., high sharpness ratio, unity steepness ratio) oscillations around 10 Hz (Tiihonen et al., 1989; Pfurtscheller et al., 1997). Similarly, the present analysis observed more extreme sharpness ratios than steepness ratios (Figure 1.2). Therefore, it may be tempting to relate the oscillations in the current study to the mu rhythm. However, the oscillations here are at a beta frequency whereas mu rhythms characteristically oscillate at an alpha frequency. Therefore, the oscillations in the present study are likely related to previous reports of sensorimotor beta rhythms (e.g., Miller et al. 2012) and distinct from previous reports of mu rhythms.

Nonsinusoidal oscillations can underlie statistical PAC

Cross-frequency coupling (CFC) analysis techniques quantify interactions between neural oscillations. One example of CFC is phase-amplitude coupling (PAC), in which the phase of an oscillation is correlated with the amplitude of a higher-frequency oscillation or broadband high frequency activity (Canolty et al., 2006). The degree of interaction between these two frequency components has been estimated using PAC metrics, often with the assumption that low frequency oscillatory phase organizes neuronal cell assembly spiking (Canolty et al., 2006; de Hemptinne et al., 2013, 2015; Lisman and Jensen, 2013; Voytek et al., 2015; Watrous et al., 2015). In this view, there are two separate interacting neural processes: a low frequency oscillator that modulates local spiking probability.

However it is helpful to distinguish several biophysical processes that can contribute to statistical PAC: coupling can occur between two oscillatory processes; alternatively, a low frequency oscillator associated with synaptic currents (Mazzoni et al. 2015; Buzsáki et al. 2012; Miller et al. 2009; Okun et al. 2010; Einevoll et al. 2013), may be coupled to high gamma activity, associated with asynchronous spiking activity (Manning et al. 2009; Ray et al. 2008; Miller et al. 2014; Miller et al. 2009). Furthermore, statistical PAC is increased by nonsinusoidal waveforms, as previously been shown in synthetic data (Kramer et al., 2008; Lozano-Soldevilla et al., 2016), high-voltage spindles (Tort et al., 2013), and cortical alpha oscillations (Lozano-Soldevilla et al., 2016). These previous reports, as well as a recent review (Aru et al., 2015) have offered suggestions for determining the nature of PAC, which can be diverse across the human cortex, simultaneously exhibiting both oscillatory and nonsinusoidal modes (Vaz et al., 2017). We here emphasize the importance of visually inspecting the raw time series to judge whether statistical PAC is driven by sharp voltage changes, as shown here, by true oscillation-to-oscillation coupling, or by sustained asynchronous activity during particular low frequency oscillatory phases.

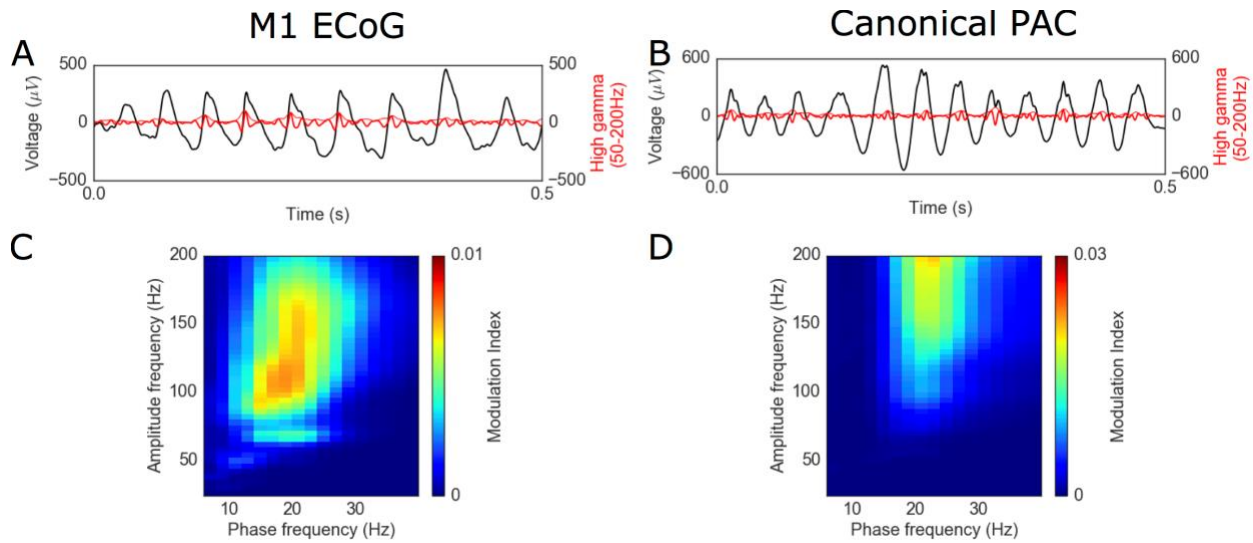


Figure 1.6. Sharp beta oscillations produce similar cross-frequency coupling estimates compared to canonical phase-amplitude coupling. (A) Raw voltage recording in a PD patient before DBS (black) overlaid with the high gamma component (thick red line) and its analytic amplitude (thin red lines). (B) Same format as (A) with a simulated signal with canonical PAC between the phase of beta oscillations and high gamma amplitude. (C-D) Comodulograms showing similar estimated PAC between beta phase and high gamma amplitude in both the (C) M1 recording and (D) canonical PAC signal.

The sharp waveforms reported here produce similar statistical PAC results compared to canonical asynchronous PAC waveforms (Fig. 1.6). The difference between the temporal dynamics in these waveforms (Fig. 1.6A-B) suggest a difference in the underlying neural activity, which is not differentiated by statistical PAC. While high gamma amplitude correlates with local population spiking activity (Manning et al. 2009; Ray et al. 2008; Miller et al. 2014; Miller et al. 2009), the magnitude of previously reported high gamma changes are low, on the order of a few microvolts. In contrast, the apparent high gamma resulting from the sharp time-domain deflections seen here are an order of magnitude stronger—over 100 microvolts in some cases (Fig. 1.6A). This extreme difference in magnitude suggests that the underlying phenomena of high gamma may not be the same in these two cases.

In summary, we offer a new perspective in which sharp voltage transients within an oscillation may carry physiological information. These often-overlooked temporal domain features should complement spectral CFC analyses. When used in conjunction, temporal

domain analysis can offer novel insights into the biophysical processes generating the statistical PAC. Here, we demonstrate that the sharpness of motor cortical beta waveforms, previously shown to reflect synchronous input, are decreased with DBS treatment of PD. Furthermore, the sharpness ratio measure positively correlates with clinical rigidity measures. This synchrony interpretation offers new insight into the pathophysiology of PD, serving as an example of how a combination of both spectral and temporal analyses may be useful in extracting critical information from electrophysiological signals.

Chapter 1, in full, is a reprint of the material as it appears in: Cole SR, van der Meij R, Peterson EJ, de Hemptinne C, Starr P, Voytek B. (2017) Nonsinusoidal oscillations underlie pathological phase-amplitude coupling in the motor cortex in Parkinson's disease. *Journal of Neuroscience*, 37(18) 4830-4840. The dissertation author was the primary investigator and author of this paper.

References

- Aru J, Aru J, Priesemann V, Wibral M, Lana L, Pipa G, Singer W, Vicente R (2015) Untangling cross-frequency coupling in neuroscience. *Curr Opin Neurobiol* 31:51–61 Available at: <http://dx.doi.org/10.1016/j.conb.2014.08.002>.
- Belluscio M, Mizuseki K, Schmidt R, Kempter R, Buzsaki G (2012) Cross-Frequency Phase-Phase Coupling between Theta and Gamma Oscillations in the Hippocampus. *J Neurosci* 32:423–435.
- Börgers C, Li J, Kopell N (2014) Approximate, not Perfect Synchrony Maximizes the Downstream Effectiveness of Excitatory Neuronal Ensembles. *J Math Neurosci* 4:10 Available at: <http://www.mathematical-neuroscience.com/content/4/1/10>.
- Brette R (2012) Computing with neural synchrony. *PLoS Comput Biol* 8.
- Brown P (2003) Oscillatory nature of human basal ganglia activity: relationship to the pathophysiology of Parkinson's disease. *Mov Disord* 18:357–363.
- Buzsáki G (2006) Rhythms of the Brain. Oxford University Press.
- Buzsáki G, Anastassiou C a., Koch C (2012) The origin of extracellular fields and currents — EEG, ECoG, LFP and spikes. *Nat Rev Neurosci* 13:407–420 Available at: <http://dx.doi.org/10.1038/nrn3241>.
- Buzsáki G, Draguhn A (2004) Neuronal oscillations in cortical networks. *Science* 304:1926–1929 Available at: <http://www.ncbi.nlm.nih.gov/pubmed/15218136>.
- Canolty RT, Edwards E, Dalal SS, Soltani M, Nagarajan SS, Berger MS, Barbaro NM, Knight RT (2006) High Gamma Power is Phase-Locked to Theta Oscillations in Human Neocortex. *313:1626–1628*.
- Cole S, Voytek B (2017) Brain oscillations and the importance of waveform shape. *Trends Cogn Sci* 21:137–149 Available at: <http://dx.doi.org/10.1016/j.tics.2016.12.008>.
- de Hemptinne C, Ryapolova-Webb ES, Air EL, Garcia PA, Miller KJ, Ojemann JG, Ostrem JL, Galifianakis NB, Starr PA (2013) Exaggerated phase-amplitude coupling in the primary motor cortex in Parkinson disease. *Proc Natl Acad Sci U S A* 110:4780–4785 Available at: <http://www.pnas.org/content/110/12/4780.abstract>.
- de Hemptinne C, Swann NC, Ostrem JL, Ryapolova-Webb ES, San Luciano M, Galifianakis NB, Starr P a (2015) Therapeutic deep brain stimulation reduces cortical phase-amplitude coupling in Parkinson's disease. *Nat Neurosci* 18:779–786 Available at: <http://dx.doi.org/10.1038/nn.3997>.
- Devergnas A, Pittard D, Bliwise D, Wichmann T (2014) Relationship between oscillatory activity in the cortico-basal ganglia network and parkinsonism in MPTP-treated monkeys. *Neurobiol Dis* 68:156–166 Available at: <http://dx.doi.org/10.1016/j.nbd.2014.04.004>.

- Einevoll GT, Kayser C, Logothetis NK, Panzeri S (2013) Modelling and analysis of local field potentials for studying the function of cortical circuits. *Nat Rev Neurosci* 14:770–785 Available at: <http://dx.doi.org/10.1038/nrn3599>.
- Engel A, Fries P, Singer W (2001) Dynamic predictions: oscillations and synchrony in top-down processing. *Nat Rev Neurosci* 2:704–716 Available at: <http://www.ncbi.nlm.nih.gov/pubmed/11584308>.
- Fries P (2005) A mechanism for cognitive dynamics: Neuronal communication through neuronal coherence. *Trends Cogn Sci* 9:474–480.
- Fries P (2015) Rhythms for Cognition: Communication through Coherence. *Neuron* 88:220–235 Available at: <http://dx.doi.org/10.1016/j.neuron.2015.09.034>.
- Gerber EM, Sadeh B, Ward A, Knight RT, Deouell LY (2016) Non-Sinusoidal Activity Can Produce Cross-Frequency Coupling in Cortical Signals in the Absence of Functional Interaction between Neural Sources. *PLoS One* 11:e0167351.
- He BJ (2014) Scale-free brain activity: Past, present, and future. *Trends Cogn Sci* 18:480–487 Available at: <http://dx.doi.org/10.1016/j.tics.2014.04.003>.
- Kondylis ED, Randazzo MJ, Alhourani A, Lipski WJ, Wozny TA, Pandya Y, Ghuman AS, Turner RS, Crammond DJ, Richardson RM (2016) Movement-related dynamics of cortical oscillations in Parkinson's disease and essential tremor. *Brain* 139:2211–2223.
- Kramer MA, Tort ABL, Kopell NJ (2008) Sharp edge artifacts and spurious coupling in EEG frequency comodulation measures. *J Neurosci Methods* 170:352–357.
- Kuhn AA, Trottenberg T, Kivi A, Kupsch A, Schneider GH, Brown P (2005) The relationship between local field potential and neuronal discharge in the subthalamic nucleus of patients with Parkinson's disease. *Exp Neurol* 194:212–220.
- Lisman JE, Jensen O (2013) The Theta-Gamma Neural Code. *Neuron* 77:1002–1016 Available at: <http://dx.doi.org/10.1016/j.neuron.2013.03.007>.
- Lozano-Soldevilla D, Huurne N, Oostenveld R (2016) Neuronal Oscillations with Non-sinusoidal Morphology Produce Spurious Phase-to-Amplitude Coupling and Directionality. *Front Comput Neurosci* 10:1–17.
- Mallet N, Pogosyan A, Márton LF, Bolam JP, Brown P, Magill PJ (2008a) Parkinsonian beta oscillations in the external globus pallidus and their relationship with subthalamic nucleus activity. *J Neurosci* 28:14245–14258.
- Mallet N, Pogosyan A, Sharott A, Csicsvari J, Bolam JP, Brown P, Magill PJ (2008b) Disrupted dopamine transmission and the emergence of exaggerated beta oscillations in subthalamic nucleus and cerebral cortex. *J Neurosci* 28:4795–4806 Available at: http://www.ncbi.nlm.nih.gov/entrez/query.fcgi?cmd=Retrieve&db=PubMed&dopt=Citation&list_uids=18448656%5Cnhttp://www.jneurosci.org/content/28/18/4795.full.pdf.
- Manning JR, Jacobs J, Fried I, Kahana MJ (2009) Broadband Shifts in Local Field Potential Power Spectra Are Correlated with Single-Neuron Spiking in Humans. *J Neurosci*

29:13613–13620 Available at:
<http://www.jneurosci.org/cgi/doi/10.1523/JNEUROSCI.2041-09.2009>.

Mazzoni A, Lindén H, Cuntz H, Lansner A, Panzeri S, Einevoll GT (2015) Computing the Local Field Potential (LFP) from Integrate-and-Fire Network Models. PLoS Comput Biol 11:1–38.

Miller KJ, Hermes D, Honey CJ, Hebb AO, Ramsey NF, Knight RT, Ojemann JG, Fetz EE (2012) Human Motor Cortical Activity Is Selectively Phase-Entrained on Underlying Rhythms. PLoS Comput Biol 8:e1002655.

Miller KJ, Honey CJ, Hermes D, Rao RPN, denNijs M, Ojemann JG (2014) Broadband changes in the cortical surface potential track activation of functionally diverse neuronal populations. Neuroimage 85:711–720 Available at:
<http://dx.doi.org/10.1016/j.neuroimage.2013.08.070>.

Miller KJ, Sorensen LB, Ojemann JG, Den Nijs M (2009a) Power-law scaling in the brain surface electric potential. PLoS Comput Biol 5:e1000609.

Miller KJ, Zanos S, Fetz EE, den Nijs M, Ojemann JG (2009b) Decoupling the cortical power spectrum reveals real-time representation of individual finger movements in humans. J Neurosci 29:3132–3137 Available at:
<http://www.jneurosci.org/cgi/doi/10.1523/JNEUROSCI.5506-08.2009>.

Moran A, Bergman H, Israel Z, Bar-Gad I (2008) Subthalamic nucleus functional organization revealed by parkinsonian neuronal oscillations and synchrony. Brain 131:3395–3409.

Moran A, Stein E, Tischler H, Bar-Gad I (2012) Decoupling neuronal oscillations during subthalamic nucleus stimulation in the parkinsonian primate. Neurobiol Dis 45:583–590 Available at: <http://dx.doi.org/10.1016/j.nbd.2011.09.016>.

Mukamel R, Gelbard H, Arieli A, Hasson U, Fried I, Malach R (2005) Coupling Between Neuronal Firing, Field Potentials, and fMRI in Human Auditory Cortex. Science (80-) 309:951–954 Available at: <http://www.sciencemag.org/cgi/doi/10.1126/science.1110913>.

Okun M, Nain A, Lampl I (2010) The subthreshold relationship between cortical local field potential and neuronal firing unveiled by intracellular recordings in awake rats. J Neurosci 20:4440–4448.

Ozkurt TE, Schnitzler A (2011) A critical note on the definition of phase-amplitude cross-frequency coupling. J Neurosci Methods 201:438–443.

Panov F, Levin E, de Hemptinne C, Swann NC, Qasim S, Miocinovic S, Ostrem JL, Starr PA (2016) Intraoperative electrocorticography for physiological research in movement disorders: principles and experience in 200 cases. J Neurosurg:1–10 Available at:
<http://thejns.org/doi/10.3171/2015.11.JNS151341>.

Penny WD, Duzel E, Miller KJ, Ojemann JG (2008) Testing for nested oscillation. J Neurosci Methods 174:50–61.

- Peterson EJ, Voytek B (2015) Balanced Oscillatory Coupling Improves Information Flow. bioRxiv:30304 Available at: <http://biorxiv.org/content/early/2015/10/30/030304.abstract>.
- Pfurtscheller G, Stancák A, Edlinger G (1997) On the existence of different types of central beta rhythms below 30 Hz. *Electroencephalogr Clin Neurophysiol* 102:316–325.
- Ray S, Crone NE, Niebur E, Franaszczuk PJ, Hsiao SS (2008) Neural correlates of high-gamma oscillations (60-200 Hz) in macaque local field potentials and their potential implications in electrocorticography. *J Neurosci* 28:11526–11536.
- Reyes AD (2003) Synchrony-dependent propagation of firing rate in iteratively constructed networks in vitro. *Nat Neurosci* 6:593–599.
- Rossant C, Leijon S, Magnusson a. K, Brette R (2011) Sensitivity of Noisy Neurons to Coincident Inputs. *J Neurosci* 31:17193–17206.
- Rubin JE, Terman D (2004) High frequency stimulation of the subthalamic nucleus eliminates pathological thalamic rhythmicity in a computational model. *J Comput Neurosci* 16:211–235.
- Schnitzler A, Gross J (2005) Normal and pathological oscillatory communication in the brain. *Nat Rev Neurosci* 6:285–296 Available at: <http://www.ncbi.nlm.nih.gov/pubmed/15803160>.
- Sharott A, Magill P.J, Harnack D, Kupsch A, Meissner W, Brown P (2005) Dopamine depletion increases the power and coherence of ??-oscillations in the cerebral cortex and subthalamic nucleus of the awake rat. *Eur J Neurosci* 21:1413–1422.
- Sherman MA, Lee S, Law R, Haegens S, Thorn CA, Hämäläinen MS, Moore CI, Jones SR (2016) Neural mechanisms of transient neocortical beta rhythms: Converging evidence from humans, computational modeling, monkeys, and mice. *Proc Natl Acad Sci* 113:E4885–E4894.
- Siapas AG, Lubenov E V., Wilson MA (2005) Prefrontal phase locking to hippocampal theta oscillations. *Neuron* 46:141–151.
- Tiihonen J, Kajola M, Hari R (1989) Magnetic mu rhythm in man. *Neuroscience* 32:793–800.
- Tort ABL, Komorowski R, Eichenbaum H, Kopell N (2010) Measuring Phase-Amplitude Coupling Between Neuronal Oscillations of Different Frequencies. *J Neurophysiol* 104:1195–1210 Available at: <http://jn.physiology.org/cgi/doi/10.1152/jn.00106.2010%5Cnhttp://www.ncbi.nlm.nih.gov/pubmed/20463205>.
- Tort ABL, Scheffer-Teixeira R, Souza BC, Draguhn A, Brankack J (2013) Theta-associated high-frequency oscillations (110-160Hz) in the hippocampus and neocortex. *Prog Neurobiol* 100:1–14.
- Trimper JB, Stefanescu RA, Manns JR (2014) Recognition memory and theta-gamma interactions in the hippocampus. *Hippocampus* 24:341–353.

Vaz AP, Yaffe RB, Wittig JH, Inati SK, Zaghloul KA, Branch SN, Scientist M, Program T (2017) Dual origins of measured phase-amplitude coupling reveal distinct neural mechanisms underlying episodic memory in the human cortex. *Neuroimage* Available at: <http://dx.doi.org/10.1016/j.neuroimage.2017.01.001>.

Voytek B, Kayser AS, Badre D, Fegen D, Chang EF, Crone NE, Parvizi J, Knight RT, D'Esposito M (2015) Oscillatory dynamics coordinating human frontal networks in support of goal maintenance. *Nat Neurosci* 18:1–10 Available at: <http://www.nature.com/doifinder/10.1038/nn.4071>.

Voytek B, Knight RT (2015) Dynamic network communication as a unifying neural basis for cognition, development, aging, and disease. *Biol Psychiatry* 77:1089.

Wang H-P, Spencer D, Fellous J-M, Sejnowski TJ (2010) Synchrony of Thalamocortical Inputs. *Science* (80-) 328:106–110.

Watrous AJ, Deuker L, Fell J, Axmacher N (2015) Phase-amplitude coupling supports phase coding in human ECoG. *Elife* 4:e07886.

Wilson CJ (2013) Active decorrelation in the basal ganglia. *Neuroscience* 250:467–482 Available at: <http://dx.doi.org/10.1016/j.neuroscience.2013.07.032>.

CHAPTER 2: Cycle-by-cycle analysis of neural oscillations

Abstract

Neural oscillations are widely studied using methods based on the Fourier transform, which models data as sums of sinusoids, to successfully uncover links between oscillations and cognition or disease. However, because of the fundamental sinusoidal basis, these methods do not fully capture neural oscillatory dynamics, because neural data are both non-sinusoidal and non-stationary. Here, we present a new, complementary analysis framework that quantifies oscillatory features in the time domain on a cycle-by-cycle basis. For each cycle, the amplitude, period, and waveform symmetry are measured, the latter of which is missed using conventional approaches. Additionally, oscillatory bursts are algorithmically identified, which restricts oscillation analysis solely to time periods when an oscillation is present. A side effect of this is that it provides the ability to investigate relationships between oscillatory bursting features with individual oscillatory cycle features. This approach is validated on simulated data and minimizes erroneous results derived from conventional metrics, such as Hilbert-based measures, which conflates event-related changes in oscillatory burst duration as increased oscillatory amplitude. Further, these methods are applied to empirical recordings—including hippocampal theta, motor cortical beta, and visual cortical alpha—and differentiate behavioral conditions.

Introduction

As a prominent feature of brain recordings, neural oscillations are frequently correlated to both pathologies (Uhlhaas and Singer, 2010; Voytek and Knight, 2015) and healthy behaviors such as movement, sleep, perception, and cognitive performance (Klimesch, 1999; Massimini et al., 2004; Hanslmayr et al., 2007; Miller et al., 2007). Standard approaches for studying these oscillations are based on the Fourier transform, which decomposes a signal into component sinusoids. However, brain rhythms are neither strictly sinusoidal nor stationary, as they come and go with varying amplitudes, frequencies, and waveforms (van Dijk et al., 2010; Jones, 2016;

Cole and Voytek, 2017). Therefore, decomposition of the neural signal using the Fourier transform does not parsimoniously capture all of the interesting structure present in neural signals. This is suboptimal given that nonsinusoidal oscillatory features carry physiological information (Buzsáki et al., 1986; Hentschke et al., 2007; Pietersen et al., 2009; Mazaheri and Jensen, 2010; Belluscio et al., 2012; Lewis et al., 2012; Lee and Jones, 2013; Trimper et al., 2014; Sherman et al., 2016; Cole and Voytek, 2017; Cole et al., 2017), and non-stationarities of low-frequency cortical oscillations may reflect different physiological processes (Peterson and Voytek, 2017). Not properly accounting for these nonsinusoidal waveforms make conventional analyses susceptible to artifactual results, such as spurious phase-amplitude and cross-frequency coupling (Kramer et al., 2008; Gerber et al., 2016; Lozano-Soldevilla et al., 2016; Scheffer-Teixeira and Tort, 2016; Cole et al., 2017; Vaz et al., 2017).

Methods used to analyze temporal properties of oscillations are also usually based on the Fourier transform. “Instantaneous” measures of oscillatory amplitude and frequency are widely used to estimate these time-varying properties of an oscillation of interest (Canolty et al., 2006; Samaha and Postle, 2015). However, computation of such instantaneous features does not directly measure them in the raw (unbiased) recording, but always in a transformed version of the data, in which the signal is usually limited to a narrow sinusoidal frequency band (Bruns, 2004). The mathematical nature of these approaches is such that they will always give a numerical result; they will always return an instantaneous amplitude, phase, and frequency value, even if there is no oscillation present in the signal, during which those instantaneous measures should be undefined. This means that these kinds of narrowband analyses can lead to misleading results. This can lead to mischaracterizations of the data, such phase slips, oscillatory frequency fluctuating within a single cycle, or an apparent increase in high frequency amplitude caused by a sharp transient (Kramer et al., 2008; Nelli et al., 2017).

Other complementary tools are therefore necessary to extract information from neural signals that Fourier-based analysis does not concisely capture. Matching pursuit is a tool for

decomposing a signal using a dictionary of functions, and has been used to analyze transient components of brain signals (Ray et al., 2003; Chandran K S et al., 2016). However, this approach has only so far been applied with a basis of Gaussian-modulated sinusoids, and it is nontrivial to decide how to parametrize the output to compare experimental conditions. Another approach, empirical mode decomposition (EMD), decomposes signals without forcing a basis function, such as the sinusoidal basis assumed in Fourier-based approaches (Liang et al., 2005; Pittman-Polletta et al., 2014). However, applications of EMD in neural signals have been limited by critical issues such as “mode mixing” in which an oscillator of interest is split among multiple components, and difficulty in identifying analogous components across different recordings (Park et al., 2013). More complicated methods have been developed to help partially overcome these issues, but EMD has rarely been applied to neural signals beyond providing features for machine learning algorithms (Diez et al., 2009; Orosco et al., 2009; Bajaj and Pachori, 2012).

Few analysis techniques have been designed specifically for characterizing the time-domain waveform shape of brain oscillations. Characterizations of oscillation waveform shape have mostly been limited to locating peaks and troughs and quantifying the relative durations of rises and decays. In the hippocampal gamma oscillation, for example, the amplitude of a cycle is positively correlated with the period of the subsequent cycle, which has been interpreted as reflecting synaptic excitation being counterbalanced by proportional inhibition (Atallah and Scanziani, 2009). The asymmetry of hippocampal theta oscillations have been characterized by the relative lengths of the rise and decay periods and correlated to memory processes (Belluscio et al., 2012; Dvorak and Fenton, 2014; Trimper et al., 2014; Amemiya and Redish, 2018). Because of its notable asymmetry, researchers studying hippocampal theta have designed an alternative instantaneous phase estimate that involves identifying extrema in each cycle (Siapas et al., 2005; Belluscio et al., 2012). Additionally, two algorithms were recently developed to extract the waveform of the *prominent* oscillator in a neural signal (Gips et al.,

2017; Jas et al., 2017), but these approaches do not capture changes in waveform shape within a recording.

We recently reviewed that waveform shape is diverse across the brain and relates to physiology, pathology, and behavior (Cole and Voytek, 2017). The hippocampal theta rhythm (Buzsáki et al., 1985), cortical slow oscillation (Amzica and Steriade, 1998), and the mu rhythm (Pfurtscheller et al., 1997) are particularly known to have stereotyped nonsinusoidal waveforms. There are a wide variety of circuit activation patterns for oscillators of each frequency (Womelsdorf et al., 2014), and the specifics of these dynamics may relate to the temporal dynamics of a single cycle of the recorded oscillation, or its waveform shape. Therefore, differences in waveform shape may hint at differences in the parameters, conditions, or even qualitative mechanisms of the oscillatory generator. One potential, or at least intuitive, interpretation of waveform shape is that sharper oscillatory extrema may be produced by more synchronous neural activity (Sherman et al., 2016; Cole et al., 2017). This may be caused by excitatory synaptic currents occurring relatively simultaneously in a cortical region and integrating in the local field to yield a sharp waveform, whereas those same currents, more spread out in time, will result in a smoother local field potential.

Here we present a time-domain approach, complementary to traditional frequency-domain analysis, designed to characterize nonsinusoidal and transient brain rhythms in order to help quantify information missed in conventional, Fourier-based neural signal processing. For each oscillatory cycle, amplitude and period (frequency) are quantified, as are its waveform symmetries. In contrast to the instantaneous features cited above, cycle-by-cycle measures are computed from straightforward features rather than relying on transforms that assume a sinusoidal structure. The only reliance on more traditional approaches is to filter out low-frequency drifts and high frequency features, which increase noise in localizing peaks and troughs. Importantly, the output also specifies whether the oscillation of interest is present or absent in the signal during each “cycle” period, as it is unlikely that the oscillator is present

throughout the whole duration of the signal (Fransen et al., 2015; Jones, 2016). This is important, as estimates of oscillatory features are meaningless if no oscillation is present.

Materials & Methods

All methods described here are available in the open-source package ‘neurodsp’, available at <https://github.com/voytekresearch/neurodsp>, and all Python code to replicate the figures in this paper are shared at https://github.com/voytekresearch/Cole_2018_cyclebycycle. All tests are nonparametric, such that correlations are Spearman, two-sample unpaired tests are Mann-Whitney U, and two-sample paired tests are Wilcoxon Signed Rank.

Segmentation of signal into cycles

The first step in characterizing individual oscillatory cycles in a neural signal is to split the entire recording into cycles. We first identify putative peaks and troughs throughout the recording. The raw data (Figure 2.1A) is optionally filtered with a broad bandpass filter to remove slow transients or high frequency activity that may interfere with peak and trough identification (Figure 2.1B). Next, the signal is bandpass filtered in the frequency band of interest, ideally verified from the power spectral density (Haller et al., 2018), and the time points of the rising and decay zero-crossings are identified (Figure 2.1C). The minima and maxima between these zero-crossings are declared as putative peaks and troughs (Figure 2.1D). Finally, the midpoints of the rise and decay flanks are computed by finding the time point at which the voltage is halfway between the peak and trough voltage (Figure 2.1E). Together, the extrema and flank midpoints can be used to estimate a “waveform phase” time series (Figure 2.1F, black) by linearly interpolating between their theoretical phases (e.g., peak has phase 0, the decay midpoint has phase $\pi/2$, etc.). If the signal is nonsinusoidal, this estimate slightly but systematically deviates from the instantaneous phase commonly computed by bandpass filtering the signal in the oscillatory frequency band and applying the Hilbert transform (Figure 2.1F, red). The waveform phase estimate more closely matches intuitions for the locations of an

oscillatory peak and trough, which can be skewed when a nonsinusoidal oscillator is filtered in a narrow frequency band (Belluscio et al., 2012; Dvorak and Fenton, 2014).

Note that this process of cycle segmentation utilizes some bandpass filtering for localizing extrema (Figure 2.1B,C). This superficially seems in contrast with the statement that a key advantage of the cycle-by-cycle method is that it is designed in a way that does not assume a sinusoidal waveform. However, statistics are not ultimately computed on this narrowband signal, as it is only a tool that is useful for estimating peaks and trough times. The filters are used in order to remove the slow transients or high frequencies that may make extrema identification more difficult. However, the filter is potentially removing some of the oscillatory signal that is outside of the broad passband. Therefore, the cutoff frequencies of the broad bandpass filter are chosen to compromise a tradeoff between the fidelity of waveform shape and the ability to localize peaks and troughs (Figure 2.1A-B).

Cycle feature computation

After the signal is segmented into cycles, each cycle is characterized by a few intuitive measures. In all analyses, cycles are chosen to start and end at consecutive peaks. The amplitude of the cycle is computed as the average voltage difference between the trough and the two adjacent peaks. The period is defined as the time between the two peaks. Rise-decay symmetry (rdsym) is the fraction of the period that was composed of the rise time (Figure 2.1G; rdsym = 0.5 is a cycle with equal durations of rise and decay). Peak-trough symmetry (ptsym) is the fraction of the period, encompassing the previous peak and current trough, that was composed of the peak (Figure 2.1G; ptsym = 0.5 is a cycle with equal durations of peak and trough). The peak period is defined as the time between a rise midpoint and subsequent decay midpoint, while the trough period is defined as the time between a decay midpoint and subsequent rise midpoint (see previous section). The distributions of these features can be computed across all cycles in a signal in order to compare oscillation properties in different neural signals (Figure 2.2).

The autocorrelation of cycle features (Figure 2.7A) was calculated in terms of cycles, in which the temporal distance between two cycles was equal to the number of cycle segments in between, plus 1. Only cycle segments that were defined to be in an oscillation regime (see next section) were included in the autocorrelation analysis, as in other analyses.

Determination of oscillatory burst periods

After computing features for each cycle, an algorithm is applied to determine whether each cycle is part of an oscillatory burst (Figure 2.3). The term “cycle” is used here not to specifically refer to a cycle of an oscillatory process, but rather a time segment of approximately one period of the oscillation of interest. This is because the entire signal is segmented into cycles, even the portions in which no oscillation is present. Oscillatory bursts are identified as time periods in which consecutive cycles in the time series had similar amplitudes, similar periods, and rise and decay flanks that are predominantly monotonic. To test this, three additional features are computed for each cycle. First, the amplitude consistency of a cycle is quantified as the relative difference in the rise and decay voltage (e.g., 0.5 corresponds to one flank being 2 times longer than another, 1.0 corresponds to the flanks being equal length, etc.). The minimum value is taken after computing this measure for each pair of adjacent flanks that includes the cycle’s rise or decay flanks. The period consistency feature is computed as the maximal relative difference between the cycle’s period and the period of the adjacent cycles (e.g., 0.5 corresponds to the previous or subsequent period being twice or half the length of the current cycle). The third and final feature, monotonicity, is the fraction of instantaneous voltage changes (difference between consecutive samples) that are positive during the rise phase and negative during the decay phase (e.g., 0.8 corresponds to 20% of the voltage time series going in the opposite direction of the current flank).

Thresholds are set for each of these three features, as well as an optional threshold for the relative oscillation amplitude, in order to match the user’s judgment for what data segments should be defined as oscillations. If the consistency and monotonicity features are all above

their respective thresholds, then they are marked as oscillating periods. The assignments are updated to require at least three consecutive cycles to be marked as an oscillating period (Figure 2.3F). In the current study, cycles were only analyzed that were defined as oscillating periods. For all hippocampal and simulated recordings, the thresholds used were those that maximized the $F\beta$ score as shown in Figure 2.4H (amplitude consistency threshold = 0.6, period consistency threshold = 0.75, monotonicity threshold = 0.8). The $F\beta$ score is used to trade off between precision and recall, where β is the relative importance weight between precision and recall.

For the motor cortical beta and visual cortical alpha analyses, thresholds were tuned in order to improve oscillatory burst detection because the signal-to-noise ratio (SNR) of the oscillations in these signals are noticeably different from the hippocampal theta and the simulated signals (amplitude consistency threshold = 0.5, period consistency threshold = 0.6, monotonicity threshold = 0.9 for beta and 0.8 for alpha). The monotonicity threshold was set higher for beta oscillations because the beta bursts were generally very large with monotonic flanks.

Simulation of oscillatory bursts with noise

Voltage time series were simulated to have properties similar to real neural recordings. Two sets of simulations were generated. First, an oscillation was simulated for 100 seconds to measure the accuracy of the cycle feature computation and the oscillatory burst detection algorithms described above (Figure 2.4). Specifically, a bursting oscillatory process (Figure 2.4B) was generated in the theta range and added to brown ($1/f^2$) noise that was highpass filtered with a cutoff frequency of 2 Hz (Figure 2.4C). The relative power of the oscillation and noise were controlled by scaling the amplitude of the brown noise using an SNR parameter. The bursting oscillator was generated one cycle at a time, and its degree of “burstiness” was defined by probabilities for entering and leaving an oscillatory regime at each cycle segment. By default, the probability of entering and leaving an oscillatory regime for each cycle was 0.2.

Furthermore, the amplitude, period, and rise-decay symmetries were randomly generated for each cycle by sampling from a Gaussian distribution defined by means and standard deviations (amplitude: mean=1, std=0.2; period: mean=1/7 seconds, std=1/70 seconds; rdsym: mean=0.5, std=0.05). To account for the positive correlation of features between cycles within a burst (Figure 2.7), an additional standard deviation term was added so that a different mean feature value was computed for each burst (amplitude: 0.1; period: 1/70 seconds; rdsym: 0.05). The broad bandpass filters applied to the simulated signals prior to cycle-by-cycle analysis matched those applied to the hippocampal theta recordings (1-25 Hz).

A second set of signals were simulated in order to compare cycle-by-cycle measures with instantaneous amplitude and frequency measures (Figure 2.5). Trials were simulated in which a 10 Hz oscillation was induced after an event. Brown noise was simulated throughout the trial (-1 to 2 seconds), and a bursting oscillator was simulated from 0 to 2 seconds in the same manner as above, except that the amplitude, period, and symmetry of oscillations were kept constant. Three conditions of 100 trials each were simulated for assessing amplitude measures. The “higher amp” condition induced alpha oscillations with a 20% greater amplitude than in the “baseline” condition. The “longer bursts” condition was half as likely to end a burst and 50% more likely to enter a burst compared to the other conditions. Similar trials were simulated for comparing cycle-by-cycle and instantaneous measures of frequency. Four conditions were simulated: “baseline”, “longer bursts”, “faster”, and “nonsinusoidal”. In the “faster” condition, an 11 Hz oscillation was simulated instead of a 10 Hz oscillation. In the “nonsinusoidal” condition, the oscillations simulated had a constant rise-decay symmetry value of 0.2 (other conditions: 0.5). The broad bandpass filters applied to these signals prior to cycle-by-cycle analysis matched those applied to the visual cortical alpha recordings (1-50 Hz).

Instantaneous amplitude and frequency computation

Instantaneous measures of amplitude and frequency were computed using common methods and applied to the simulated alpha oscillations described in the previous paragraph.

Signals were first bandpass filtered (8-12 Hz) and then the Hilbert transform was applied. The magnitude of the resultant time series was computed to obtain the instantaneous amplitude estimate, and the angle was computed to obtain the instantaneous phase estimate.

Instantaneous frequency was computed from the instantaneous derivative of the phase time series, and then iteratively median filtered using 10 window sizes linearly spaced between 10 ms and 400 ms as previously described (Samaha and Postle, 2015).

Hippocampal theta recordings

Local field potential recordings from the CA1 pyramidal cell layer of the hippocampus and layer 3 of the entorhinal cortex (EC3) were obtained from the “hc3” dataset on the Collaborative Research in Computational Neuroscience (CRCNS) database (Teeters et al., 2008; Mizuseki et al., 2014). A recording was chosen in which CA1 and EC3 were recorded simultaneously, and for which position data was also available (rat ec014, session 440, the deepest contact on shanks 3 and 11) in which the rat was performing an alternation task in a T-maze with wheel running (Pastalkova et al., 2008). Another recording of CA1 theta oscillations from the same database was used in Figure 2.7. For more information on the data collection, see (Mizuseki et al., 2014). The speed of the rat was estimated for each cycle by dividing the net distance traveled during the cycle by the duration of the cycle. “Move” periods were defined as when the speed was above the 90th percentile, and “no move” periods were defined as when the speed was below the 10th percentile. Note that this measure of movement does not include running on the wheel but only moving through the T-maze. Recording sampling rate was 1252 Hz for neural data and 39.0625 Hz for position data. Prior to cycle-by-cycle analysis, a broad bandpass filter (1-25 Hz) was applied to these signals in order to improve extrema localization. During cycle segmentation the narrow bandpass filter cutoff frequencies were 4 and 10 Hz.

Motor cortical beta recordings

Electrocorticography recordings from 23 patients with Parkinson’s disease were obtained during surgery for implantation of a deep brain stimulator and publicly released (de

Hemptinne et al., 2015). Briefly, a strip of electrodes with 1 cm contacts was inserted over the primary motor cortex (M1) and re-referenced using a bipolar montage of adjacent contacts. The signals analyzed in this study were from a single channel in which one of the electrodes was over M1. Recordings were collected for 30 seconds before and during DBS. For more information on the data collection see (de Hemptinne et al., 2015). Recording sampling rate was 1000 Hz. Prior to cycle-by-cycle analysis, signals were lowpass filtered at 200 Hz, and high frequency peaks (60 Hz and above) were removed (identical to (Cole et al., 2017)). During cycle segmentation the narrow bandpass filter cutoff frequencies were 13 and 30 Hz.

Visual cortical alpha recordings

The electroencephalography recording analyzed in Figure 2.10 was taken from a previously published study (Peterson and Voytek, 2017). Briefly, the recording contained two sections. First, the subject was at rest with eyes closed for two minutes prior to beginning an experiment. Second, two minutes of data were analyzed during which the subject was performing a task in which they fixated and pressed a button when they perceived a faint visual stimulus. The trace analyzed was collected from position Oz (occipital midline electrode), referenced to FCz (frontocentral midline electrode). For more information on the data collection, see (Peterson and Voytek, 2017). Recording sampling rate was 500 Hz. Prior to cycle-by-cycle analysis, a broad bandpass filter (2-50 Hz) was applied to these signals in order to improve extrema localization. During cycle segmentation the narrow bandpass filter cutoff frequencies were 6 and 14 Hz.

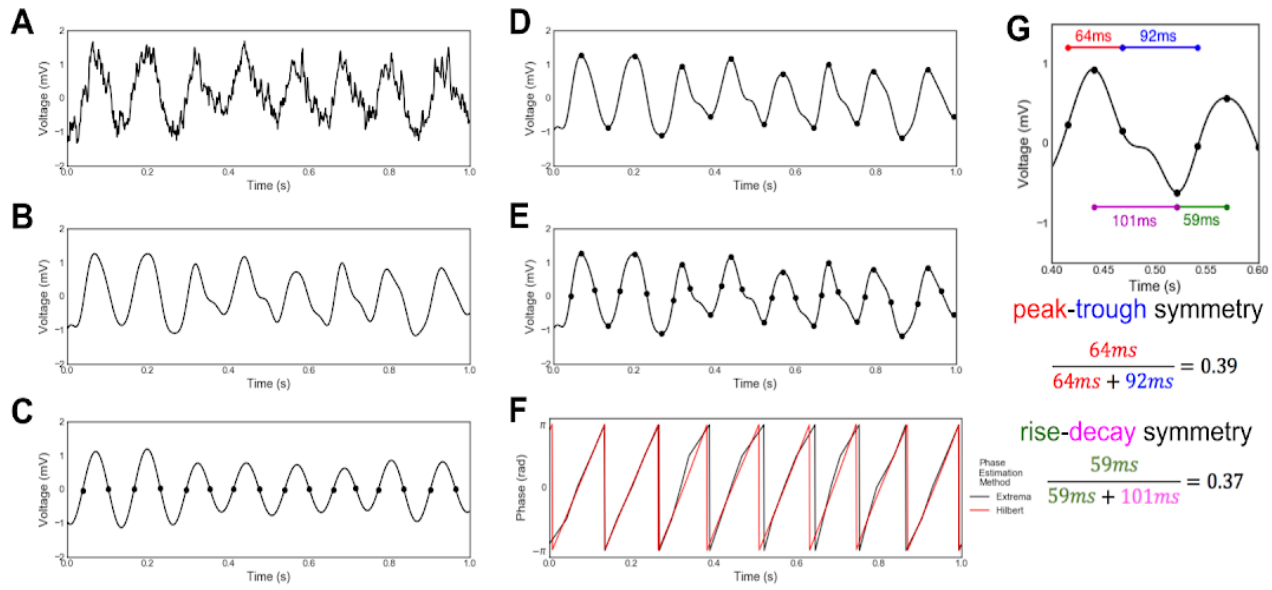


Figure 2.1. Decomposing a neural signal into individual cycles. (A) Example raw field potential recording from the CA1 layer of rat hippocampus. (B) The raw signal is broadly bandpass filtered (1-25 Hz) in order to remove high frequencies while preserving underlying theta waveform shape. (C) Zero-crossings are found after the signal has been bandpass filtered in the theta frequency range (4-10 Hz). (D) Peaks and troughs are found in the broad-bandpass filtered signal by finding the relative maxima and minima between the zero-crossings found in the theta-filtered signal (C). (E) Flank midpoints are determined by locating the time points at which the voltage is halfway between the adjacent peak and trough voltages. These points denote the boundaries between peak and trough. (F) Instantaneous phase is estimated by interpolating between extrema and flank midpoints (black). This waveform-based phase estimate is contrasted against the analytic phase estimated using the more standard, Fourier-based filtering and Hilbert transform approach (red). Discrepancies between the two approaches are notable. (G) Demonstration of computed symmetry of a single cycle. The rise-decay symmetry is computed as the fraction of the period that the cycle is in the rise phase. Similarly, the peak-trough symmetry is computed as the fraction of the period between the rise midpoint and the subsequent decay midpoint (i.e., the peak).

Results

Cycle-by-cycle oscillatory feature distributions

In order to demonstrate the usefulness of our method, we applied our cycle-by-cycle analysis technique (Figure 2.1, see Methods) to recordings of theta oscillations in the pyramidal layer of CA1 and layer 3 of the entorhinal cortex (EC3) in a rat (Mizuseki et al., 2014).

Example traces from CA1 and EC3 are shown in Figure 2.2A-B, and the remaining panels summarize the oscillatory properties of these recordings. While the amplitude of the CA1 oscillation varies roughly between 1-2.5 mV, the theta oscillations in EC3 extend up to 4 mV (Figure 2.2C). However, the frequency of these two oscillators were very consistent with one another, as the distribution of periods mainly ranged between 100-150 ms, corresponding to 7-10 Hz (Figure 2.2D) in both CA1 and EC3. Theta oscillations in both regions exhibited reliable rise-decay asymmetry (rdsym) such that the rise period was systematically shorter than the decay period (Figure 2.2E). The peak around rdsym=0.4 represents that the rise period generally made up around 40% of the cycle, or in other words, that the decay period was about 50% longer than the rise period. The theta oscillation rdsym in CA1 was more variable than in EC3, shown by the broader distribution (Figure 2.2E, black). The CA1 and EC3 differed most in terms of their peak-trough symmetry (ptsym). Figure 2.2F shows that the CA1 theta oscillations tend to have shorter peaks than troughs ($\text{ptsym} < 0.5$) while EC3 theta oscillations tend to have shorter troughs and longer peaks ($\text{ptsym} > 0.5$). While ptsym is opposite between CA1 and EC3, this cannot be explained by a simple inversion in polarity, because that would require opposite rise-decay symmetries, which is not the case (Figure 2.2E).

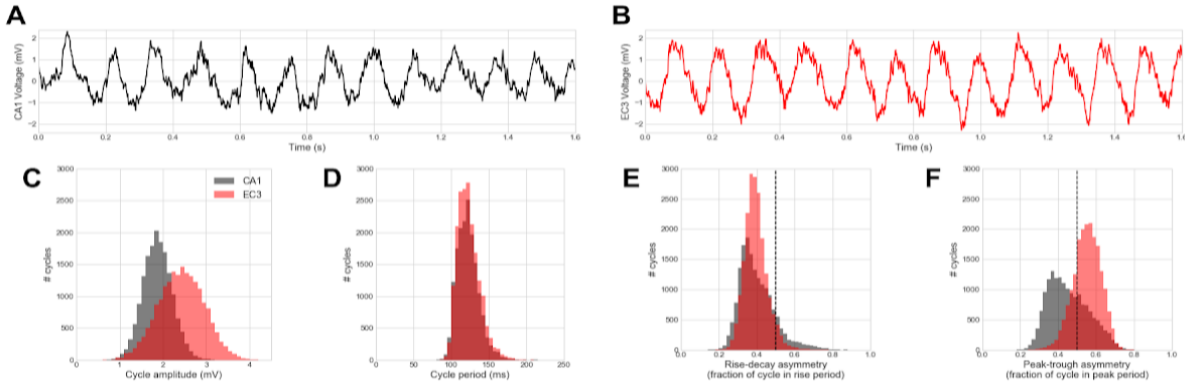


Figure 2.2. Distributions of cycle features differ between theta oscillations recorded in the CA1 pyramidal layer and layer 3 of the entorhinal cortex (EC3). (A,B) Raw voltage recording of theta oscillations in (A) CA1 and (B) EC3. (C-F) Distributions of cycle: (C) amplitude, (D) period, (E) rise-decay symmetry, and (F) peak-trough symmetry for CA1 (black) and EC3 (red) theta oscillations. Vertical dashed lines at 0.5 in E,F note relative rise-decay and peak-trough symmetry, respectively. Note that EC3 oscillations are (C) relatively higher amplitude and (F) have relatively longer peaks than CA1 oscillations, while the two show little difference in (D) their period (frequency) or (E) rise-decay asymmetry. This emphasizes the uniqueness of information provided by these different measures and how they might be used to uncover new physiological insight.

It is interesting to consider the correlations between features in order to determine whether they contain redundant information. For example, cycle asymmetry may be unidimensional in theta oscillations, meaning that those cycles that are more rise-decay asymmetric are also the ones that are more peak-trough asymmetric. However, there is only a weak correlation between these two symmetries in the analyzed CA1 recording (Spearman correlation, $r=-0.07$). Additionally, there was a positive correlation between the rise-decay symmetry and the period ($r=0.18$), but there was no correlation between this symmetry of the theta oscillations and their amplitudes ($r=0.0002$). Note that p-values are not reported for this single-recording analysis because they should be interpreted with caution. The statistics assume that each cycle is independent, while in fact there are significant autocorrelations in cycle-by-cycle features (see below).

In order to restrict our oscillatory feature analysis to only the portions of the signal in an oscillatory regime, we applied an algorithm to determine which “cycles” that the original signal

had been segmented into are truly part of an oscillation. We set requirements for the amplitude and periods of consecutive cycles to be similar, for flanks to be monotonic, and for a minimum number of cycles in each oscillatory period (Figure 2.3A-F, see Methods). These requirements can all be controlled by hyperparameters. For example, Figure 2.3G shows how increasing the amplitude and period consistency requirements decreases the fraction of the hippocampal recording that is defined to be in a theta oscillatory regime (minimum monotonicity = 0.8, see Methods).

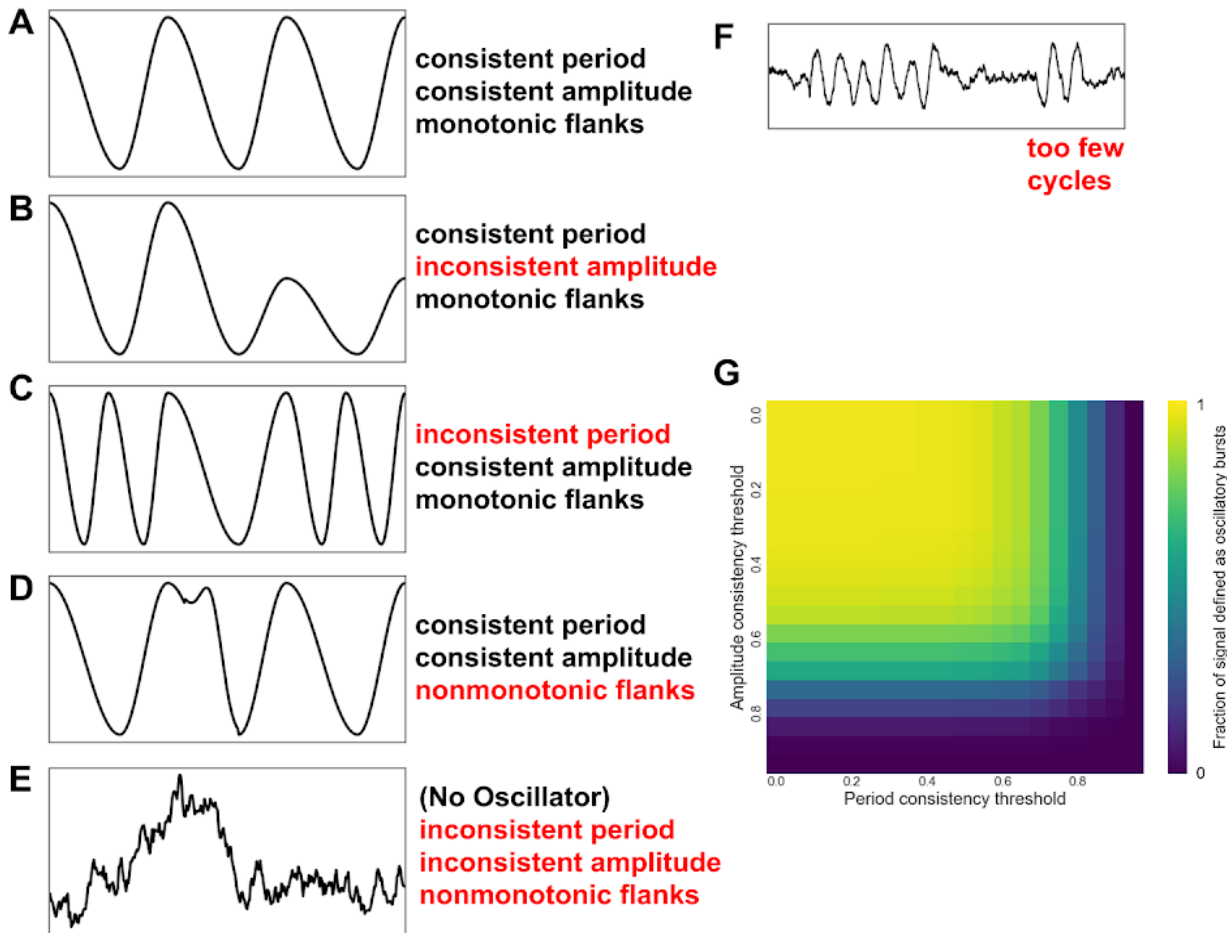


Figure 2.3. Determining oscillatory bursts in a neural signal. (A-F) In order for cycle-by-cycle measures to be meaningful, first a cycle must be determined to be a part of an oscillation. To determine this, its amplitude and period must be about the same as the adjacent cycles. Additionally, the rise and decay flanks should be mostly monotonic. According to these criteria: (A) passes all these requirements; (B) fails because the amplitudes are inconsistent; (C) fails because the period is inconsistent; (D) fails because the decay flank is considerably nonmonotonic, and; (E) fails because the peaks and troughs found in this noisy signal would violate all of the aforementioned requirements. The second burst in (F) would fail to be considered oscillatory because there are too few cycles present (minimum is 3 cycles). (G) Because these decision points are flexible, we examined how they interact. The fraction of cycles marked as oscillating in a hippocampal theta recording decreases as the amplitude and period consistency requirements are set to be more strict (closer to 1).

Accuracy of detecting and characterizing oscillatory bursts

In order to assess the accuracy of our cycle-by-cycle oscillatory detection and characterization, we simulated a neural signal with a bursting oscillatory process and noise (Figure 2.4A-D, see Methods). This simulated signal had four times the power in the oscillation compared to the brown noise process (SNR=4). First, we tested if the algorithm can determine which periods of the signal were simulated in an oscillatory regime. Figure 2.4E-F shows the precision and recall of this algorithm with different amplitude and period consistency requirements. Intuitively, as the requirements become more strict (increase), a higher fraction of the cycles declared as oscillating are truly oscillating (high precision), but a lower fraction of the truly oscillating cycles are detected (low recall). The F_β score is used to trade off between precision and recall, where β is the relative importance weight between precision and recall. For example, the F1 score (Figure 2.4G) weights precision and recall equally. For this signal, the F1 score is maximized when the amplitude consistency hyperparameter is set to 0.4 and the period consistency hyperparameter is set to 0.55. In this case, the algorithm's precision is 75% and its recall is 82%. However, if we are more concerned that the cycles we analyze are truly oscillating than capturing all truly oscillating cycles, we can weight precision more than recall by setting $\beta < 1.0$. In this scenario, the F_β score ($\beta = 0.2$) is maximized when the amplitude consistency hyperparameter is set to 0.6 and the period consistency hyperparameter is set to 0.75 (Figure 2.4H, precision = 97%, recall = 29%). That is, we are most accurate at determining oscillatory periods when we require adjacent cycles to be at least 60% similar (i.e., differ by no more than 40%) in amplitude and 75% similar in period. Note that the monotonicity requirement was fixed to 0.8 (see Methods).

Additionally, we assessed how well the properties of each cycle of the simulated oscillation matched the feature measurements after noise was introduced. Figures 2.4I-K show positive correlations between the simulated and measured values of amplitude ($r=0.64$), period ($r=0.82$), and rise-decay symmetry ($r=0.67$). The cycle amplitude tended to be overestimated

because the measurement is positively biased by noise (Figure 2.4I). The cycles were also estimated to be more asymmetric than their true simulated structure (Figure 2.4K).

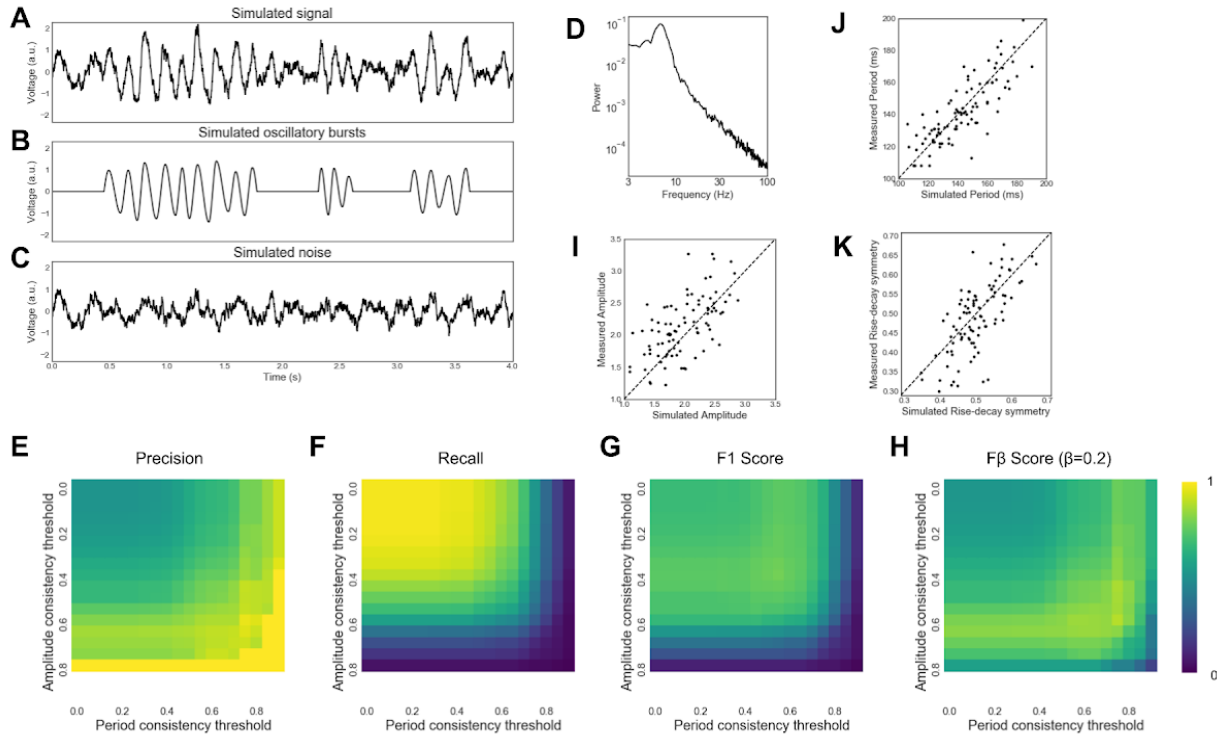


Figure 2.4. Validating cycle-by-cycle analysis with simulated data. (A-C) (A) A neural signal was simulated by adding, (B) a non-stationary bursting oscillation to, (C) brown noise. (D) Power spectral density of the simulated neural signal contains a peak at 7 Hz and a $1/f^2$ aperiodic process. (E-H) Accuracy of the algorithm used to determine if a cycle is in an oscillation. Amplitude and period consistency requirements were varied and accuracy was measured by (E) precision, (F) recall, (G) accuracy (F1 score), and (H) effectiveness ($F\beta$ score; $\beta = 0.2$). (I-K) There was a positive correlation between a cycle's simulated (I) amplitude, (J) period, and (K) rise-decay symmetry and their measured values. These results show that our approach, using the decision parameters outlined, are successfully capturing the ground-truth data.

Cycle-by-cycle vs. instantaneous measures of amplitude and frequency

We believe that measuring amplitude and frequency measures on a cycle-by-cycle basis could provide a better estimate of these properties compared to conventionally used instantaneous Hilbert-based measures, because the latter are not direct measurements of these properties but rather are based on filtering and nonlinear transformations. Therefore, we compared how these measures could differentiate conditions in a simulated experiment that elicit oscillations with differing amplitude and frequency (see Methods). This hypothetical experiment caused a 10 Hz oscillation after an event. There were three conditions: “baseline”, “higher amp”, and “longer bursts” (Figure 2.5A). The oscillations in the “higher amp” condition were 20% greater in amplitude than in the other conditions. The “longer bursts” condition was 50% more likely to enter an oscillatory burst and 50% less likely to leave a burst relative to the other conditions. Instantaneous and cycle-by-cycle amplitudes were computed for the simulated trials (100 per condition) and averaged across each condition. The average instantaneous amplitude trace for “higher amp” was appropriately greater compared to the “baseline” condition (Figure 2.5B). However, the instantaneous amplitude for the “longer bursts” trials was even greater, even though these cycles had the same amplitude as the “baseline” trials. This undesirable trait is the result of averaging non-stationary processes across many trials (Latimer et al., 2015; Jones, 2016). Therefore, a consistent oscillation at a high amplitude may not be distinguishable from an inconsistent oscillation at a lower amplitude. In contrast, the cycle-by-cycle amplitude measure was appropriately increased specifically only for the “higher amp” condition (Figure 2.5C). Additionally, the cycle-by-cycle approach allows analysis of whether the signal is in an oscillatory burst, and so we can observe that the “longer bursts” condition was more commonly oscillating than the other two conditions (Figure 2.5D). This shows how cycle-by-cycle measures can capture features of oscillatory amplitude better than conventional Fourier-based methods.

Further, we compared how these two approaches to measuring oscillatory amplitude can statistically differentiate these conditions. To do this, the mean amplitude was computed between 500 and 1000 ms in each trial. The mean trial instantaneous amplitude only weakly differentiated the “baseline” and “higher amp” conditions (Figure 2.5E, $U=4232$, $p=0.03$) while the mean cycle amplitude more significantly differentiated these conditions (Figure 2.5F, $U=123$, $p<10^{-13}$). This is due in large part to the ability of the cycle-by-cycle method to focus only on the portions of the signal in which the oscillation is present. When a conventional burst detection algorithm (Feingold et al., 2015) was applied to limit the scope of analysis to only time periods containing an oscillation, this improved the instantaneous amplitude estimate to better differentiate the “baseline” and “higher amp” conditions ($U=1963$, $p<10^{-5}$), though still not as well differentiated as the cycle amplitude estimates.

Additionally, instantaneous amplitude analysis falsely found a significant difference in oscillation amplitude between the “baseline” and “longer burst” conditions (Figure 2.5G, $U=2457$, $p<10^{-9}$), while the cycle-by-cycle amplitude analysis successfully found no significant difference (Figure 2.5H, $U=1797$, $p=0.18$). This can be attributed partially to the inability of the instantaneous amplitude analysis to focus on the segments of the signal with an oscillation, but applying the conventional burst detection technique still yields a false (albeit, smaller) significant difference in oscillation amplitude between these conditions ($U=2362$, $p<10^{-5}$).

Similarly, we simulated conditions of this experiment that frequency measures should be able to differentiate (Figure 2.6A). The “faster” condition simulates an 11 Hz (instead of 10 Hz) oscillation and the “nonsinusoidal” condition simulates an oscillation with relatively steep rises ($rdsym = 0.2$). The instantaneous frequency was averaged across trials for each condition (Figure 2.6B). Similarly, frequency was computed from the cycle-by-cycle period measures and averaged across trials (Figure 2.6C). Both Hilbert and cycle-by-cycle approaches were able to differentiate between the 10 Hz and 11 Hz oscillators (Figure 2.6D-E, instantaneous $U=1800$, $p<10^{-14}$; cycle $U=70$, $p<10^{-15}$). However, when using Hilbert-based methods, there was a

spurious increase in instantaneous frequency in the “longer bursts” condition compared to the “baseline” condition (Figure 2.6F, $U=3395$, $p<10^{-4}$). This is likely because instantaneous frequency is biased by aperiodic portions of the signal, depending on the distribution of power in the filtered frequency band, relative to periodic portions. For example, the average instantaneous frequency measure of white noise after an 8-12 Hz bandpass filter will be 10Hz. In the case of colored noise, the average instantaneous frequency would be slightly lower than 10Hz. In contrast to the instantaneous frequency measure, there was no difference in the cycle frequency measured in the “baseline” and “longer bursts” conditions (Figure 2.6G, $U=1729$, $p=0.20$). Both approaches correctly measured no frequency difference between the sinusoidal and nonsinusoidal oscillations (Figure 2.6H-I, instantaneous $U=4939$, $p=0.44$; cycle $U=1017$, $p=0.20$).

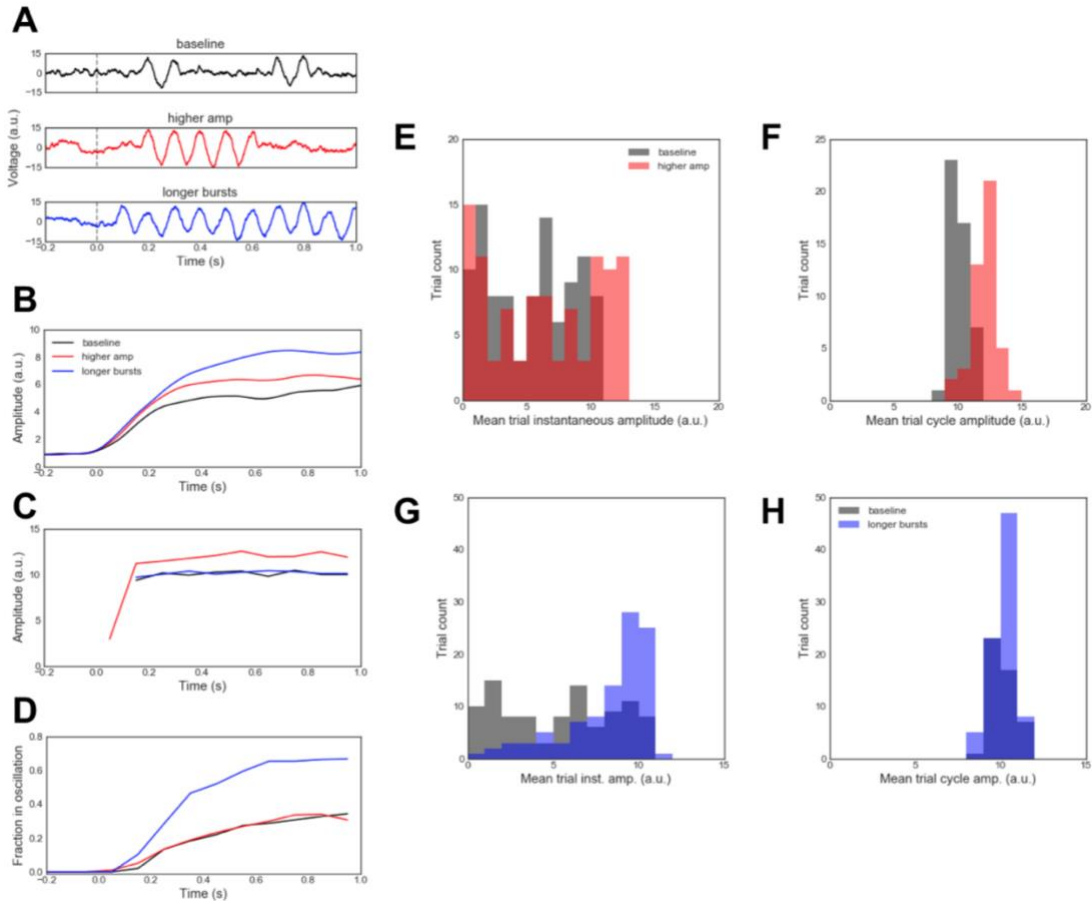


Figure 2.5. Comparison of cycle-by-cycle and instantaneous amplitude analysis on simulated event-related data. (A) Three different event-related oscillatory changes were simulated for an event occurring at 0.0 seconds: (1, black) a “baseline” condition in which short, 10 Hz oscillatory bursts were injected into the data after a simulated event onset; (2, red) a “higher amp” condition in which oscillations had 20% higher amplitude than in the “baseline” condition, and; (3, blue) a “longer bursts” condition wherein bursts were half as likely to end and 50% more likely to begin compared to the other conditions. (B) Event-related instantaneous amplitude changes, using conventional Fourier and Hilbert approaches, were averaged across three types of trials: “baseline”, “higher amp”, and “longer bursts”. (C) Same as (B), but using cycle-by-cycle approaches introduced here. Amplitude estimates were averaged across trials and binned at 100 ms intervals. This amplitude estimate is not defined when no oscillating bursts are detected, hence the lack of an average before the event. (D) Same as (C), but showing the fraction of cycles that were defined as oscillating for each condition, binned at 100 ms intervals. Note that this approach is not standard for Fourier-based analyses. (E,F) Distributions of the average (E) instantaneous amplitude and (F) cycle amplitude between 500 ms and 1000 ms for each trial in the “baseline” (black) and “higher amp” (red) conditions. Note that conventional Fourier and Hilbert approaches only weakly identify event-related amplitude increases as such (B,E) while misclassifying longer bursts as increased amplitude (B). This is the result of averaging across trials. This mischaracterization is mitigated by the cycle-by-cycle approach introduced here, which successfully differentiates event-related changes in amplitude (C,F) from changes in burst duration (D). (G,H) Similar to panels (E,F) but showing the difference in amplitude distributions between the “baseline” (black) and “longer bursts” (blue) conditions. Note that the conventional Hilbert approach detects an increase in amplitude during the longer bursts condition because the oscillation is more present, even though it has the same amplitude when present.

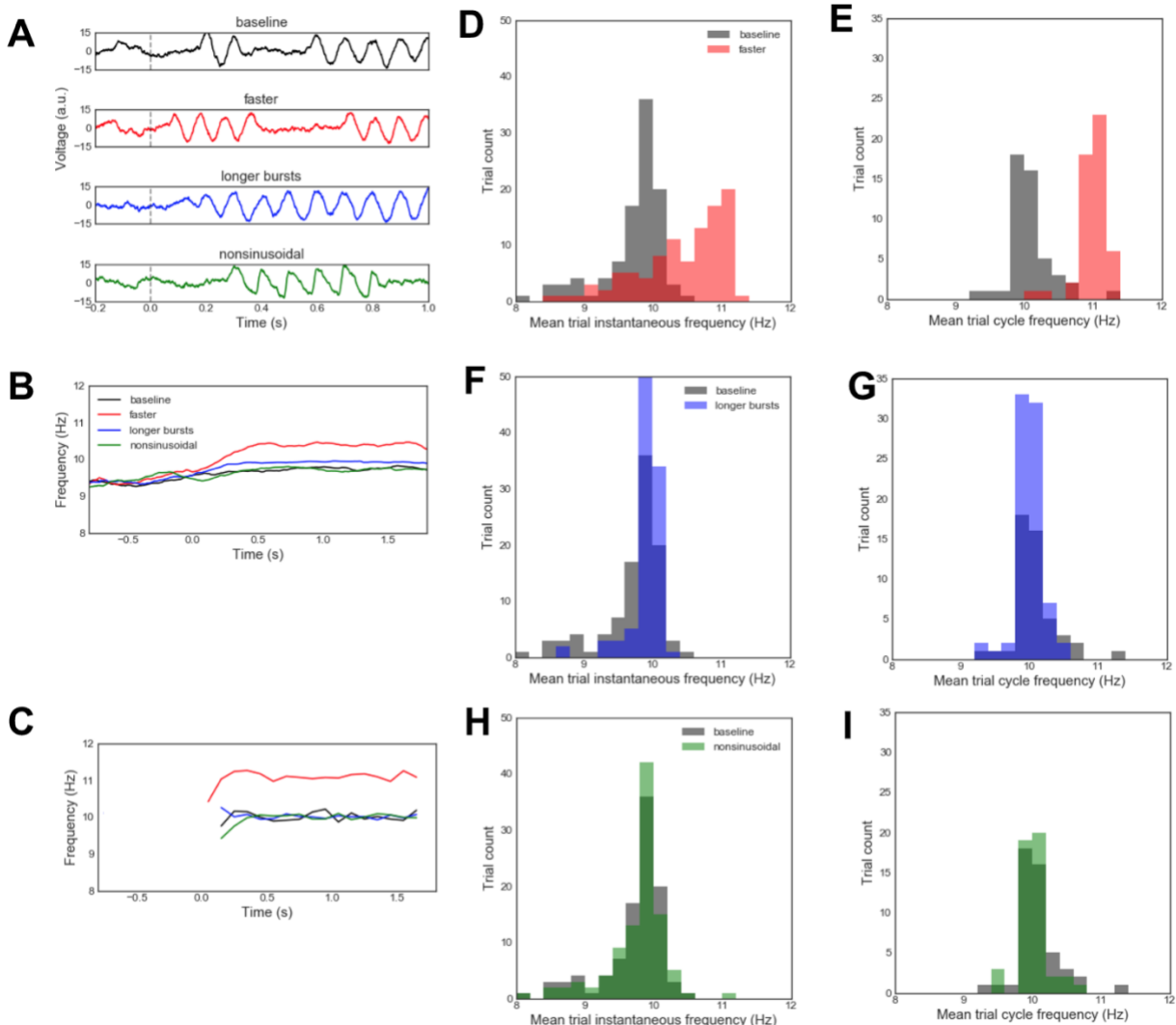


Figure 2.6. Comparison of cycle-by-cycle and instantaneous frequency analysis on simulated data. (A) Four different event-related oscillatory changes were simulated for an event occurring at 0.0 seconds: (1,2) “baseline” and “longer bursts” conditions, similar to (Figure 2.4); (3) a “faster” condition wherein an 11 Hz oscillation was simulated instead of a 10 Hz oscillation, and; (4) a “nonsinusoidal” condition where oscillations had a constant rise-decay symmetry value of 0.2 (other conditions: 0.5). (B) Instantaneous Hilbert frequency profiles averaged across the four trial types: “baseline” (black), “faster” (red), “longer bursts” (blue), and “nonsinusoidal” (green). (C) Same as (B), but the cycle-by-cycle frequency estimate was averaged across trials and binned at 100 ms intervals. This frequency estimate is not defined when no oscillating bursts are detected, hence the lack of an average before the event. (D,E) Distributions of the average (D) instantaneous frequency and (E) cycle frequency between 500 ms and 1000 ms for each trial in the “baseline” and “faster” conditions. (F-I) Same as panels C-D but comparing the “baseline” condition to the (F,G) “longer bursts” condition and the (H,I) “nonsinusoidal” oscillation condition. Note that conventional Fourier and Hilbert approaches capture event-related frequency increases (B,D) but also mischaracterize longer bursts as faster oscillations (F). This mischaracterization is mitigated by the cycle-by-cycle approach introduced here, which successfully differentiates event-related changes in frequency from other conditions (C,E,G,I).

Autocorrelations of cycle features

An advantage of this cycle-by-cycle analysis framework is that it allows us to study the similarity of features between oscillatory cycles. For example, nearby cycles may have more similar symmetry properties compared to distant cycles. Through visual inspection, we observed that in nearby oscillatory bursts, the cycles in one may consistently have longer rise periods, whereas the cycles in the other burst may have relatively shorter rise periods. This would suggest that cycles within a burst have similar symmetry properties, which is shown by a significantly positive autocorrelation (Figure 2.7A). Additionally, nearby cycles are more likely to have similar amplitude and period, but these correlations are slightly confounded by the period and amplitude consistency requirements imposed in defining whether a cycle is to be considered for analysis. Therefore, we reran the analysis using an oscillatory burst detection algorithm based solely on an amplitude threshold (Feingold et al., 2015). Adjacent cycles remained correlated in their amplitudes ($r=0.30$), rise-decay symmetry ($r=0.41$), and peak-trough symmetry ($r=0.23$), but less so for period ($r=0.06$). Results were similar in another control analysis that selectively removed the amplitude (or period) consistency requirement and then assessed similarity between adjacent cycles (amplitude: $r=0.48$, period: $r=-0.002$).

Because our analysis framework splits the recording into distinct oscillatory bursts, we also tested if consecutive bursts have correlated features. For this, we computed the burst feature (amplitude, period, or symmetry) as the mean of its cycles' features. Whereas consecutive cycles had a strong positive correlation in their amplitudes, there was no correlation between the average amplitudes of consecutive bursts (Figure 2.7B, $r=0.06$, $p=0.17$). There was a modest correlation between the theta period (frequency) in adjacent bursts (Figure 2.7C, $r=0.17$, $p<0.001$), weak correlation between rise-decay symmetries (Figure 2.7D, $r=0.09$, $p=0.03$), and no correlation between peak-trough symmetries (Figure 2.7E, $r=-0.02$, $p=0.65$) of adjacent bursts. Together, this analysis suggests that the theta generative process during this

recording is similar between cycles within a burst, but that there was a substantial change in the physiological parameters between oscillatory bursts.

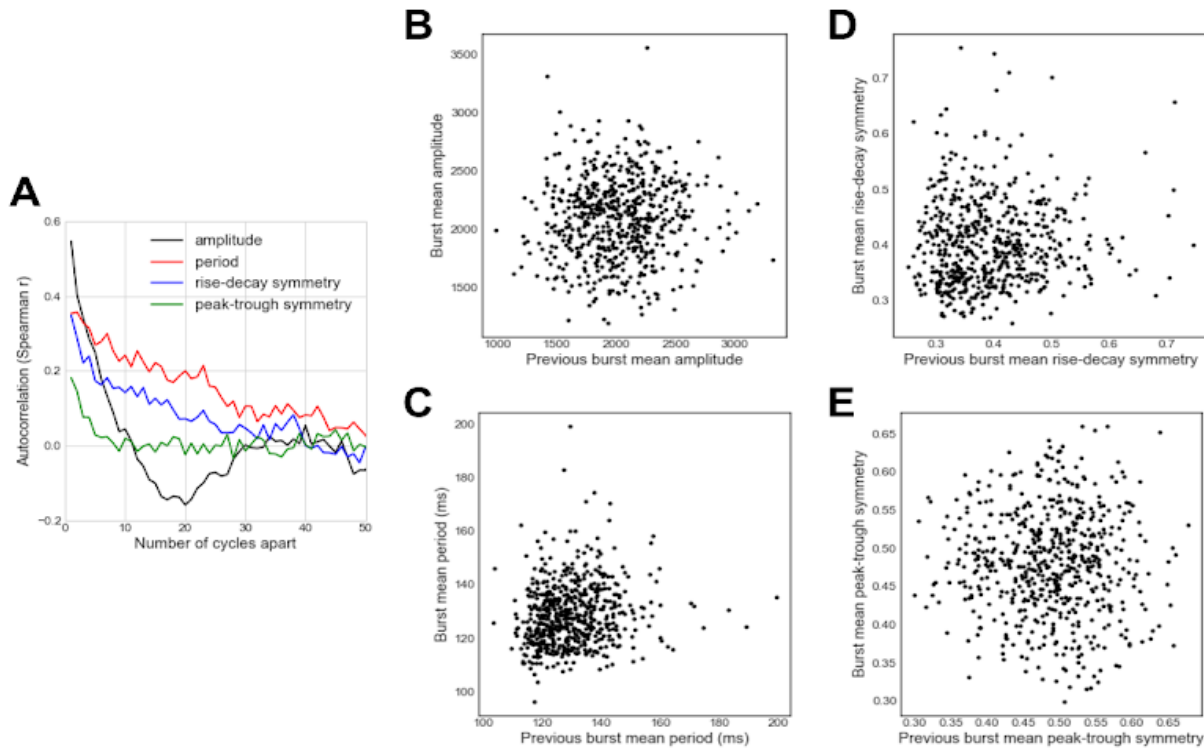


Figure 2.7. Autocorrelation of cycle features within, but not between, bursts of the hippocampal theta oscillation. (A) Autocorrelation of amplitude, period, and symmetry show that these features tend to be positively correlated for nearby cycles of the hippocampal theta oscillation recorded in an example rat. Note that the amplitude and peak-trough symmetry autocorrelations decay most rapidly. (B-E) The mean (B) amplitude, (C) period, (D) rise-decay symmetry, and (E) peak-trough symmetry of a burst are largely uncorrelated with the features of the previous burst. These results are not meant to conclusively demonstrate a physiological rule, but rather are used to highlight how novel information can be extracted using cycle-by-cycle approaches.

Cycle-by-cycle analysis to differentiate conditions

We demonstrate how the cycle-by-cycle analysis technique can be applied to three commonly analyzed oscillations: hippocampal theta, motor cortical beta, and visual cortical alpha. We compared a rat's CA1 hippocampal theta oscillations between periods when it was moving and not moving (see Methods). Figures 2.8A-B show example recording segments in which the rat is moving and not moving, with its position plotted in Figure 2.8C. Figure 2.8D-G

compare the theta oscillatory features between cycles in which its measured speed was below the 10th percentile (not moving, 1430 cycles), and cycles in which the measured speed was above the 90th percentile (moving, 1430 cycles). There was a slight increase in theta amplitude with running (Figure 2.8D) and a notable decrease in period (Figure 2.8E), as previously reported (McFarland et al., 1975; Sławińska and Kasicki, 1998). Additionally, previous studies have qualitatively reported that theta oscillations are more rise-decay asymmetric (shorter rise) when running (Buzsáki et al., 1985; Hentschke et al., 2007; Belluscio et al., 2012), and we quantify that effect here (Figure 2.8F), as well as identify an increase in peak-trough asymmetry (Figure 2.8G, shorter peak). Additionally, scatter plots in Figures 2.8H-K show these effects when considering each individual cycle. Most notably in these plots, the time periods with the highest speed ($\log(\text{speed}) > 1.5$ a.u.) tend to have different feature distributions compared to the cycles at which the rat was running at lower speeds.

Next, we re-analyzed motor cortical recordings from a previous study in which it was shown that “sharpness asymmetry” of motor cortical beta oscillations was decreased with deep brain stimulation (DBS) treatment of Parkinson’s disease (Cole et al., 2017). The current “peak-trough asymmetry” measure was designed to measure the same intuitive sense of “sharpness,” but it differs in that it is computed as a temporal ratio that is independent of amplitude (Figure 2.1G, see Methods), whereas the previously used “sharpness asymmetry” was confounded with amplitude. Figure 2.9A-B show recordings from an example subject before and during DBS. In this subject, DBS decreased the amplitude of beta oscillations (Figure 2.9C), but did not affect their period (Figure 2.9D) or rise-decay symmetry (Figure 2.9E). Across the patient population (N=23), there was no consistent effect of DBS on amplitude (Wilcoxon Signed Rank test, W=86, p = 0.11), period (W=85, p=0.11), or rise-decay asymmetry (W=132, p=0.86). However, DBS did elongate the relative peak time in the example subjects(Figure 2.9F), and consistently caused the beta oscillations to become more peak-trough symmetric (Figure 2.9G, W=53, p=0.01), consistent with the previously published sharpness ratio results (Cole et al., 2017).

Note that peak-trough asymmetry here is measured as the difference from a symmetric oscillation, such that 0 represents equal duration peaks and troughs, and 0.1 represents an oscillation in which the average cycle was 60% peak or 60% trough (i.e., $0.6 - 0.5 = 0.1$ and $0.4 - 0.5 = -0.1$). This was done because the polarity was not consistent across recordings.

Lastly, raw EEG recordings are shown for a subject while resting with eyes closed (Figure 2.10A) and while performing a visual target detection task (Figure 2.10B). We replicate the well-known observation that alpha amplitude is increased in the visual cortex while eyes are closed (Figure 2.10C). This is shown both by higher values in the amplitude distribution and by the increased number of alpha cycles detected. However, we do not observe as substantial of a difference in the period, rise-decay symmetry, or peak-trough symmetry (Figure 2.10D-F).

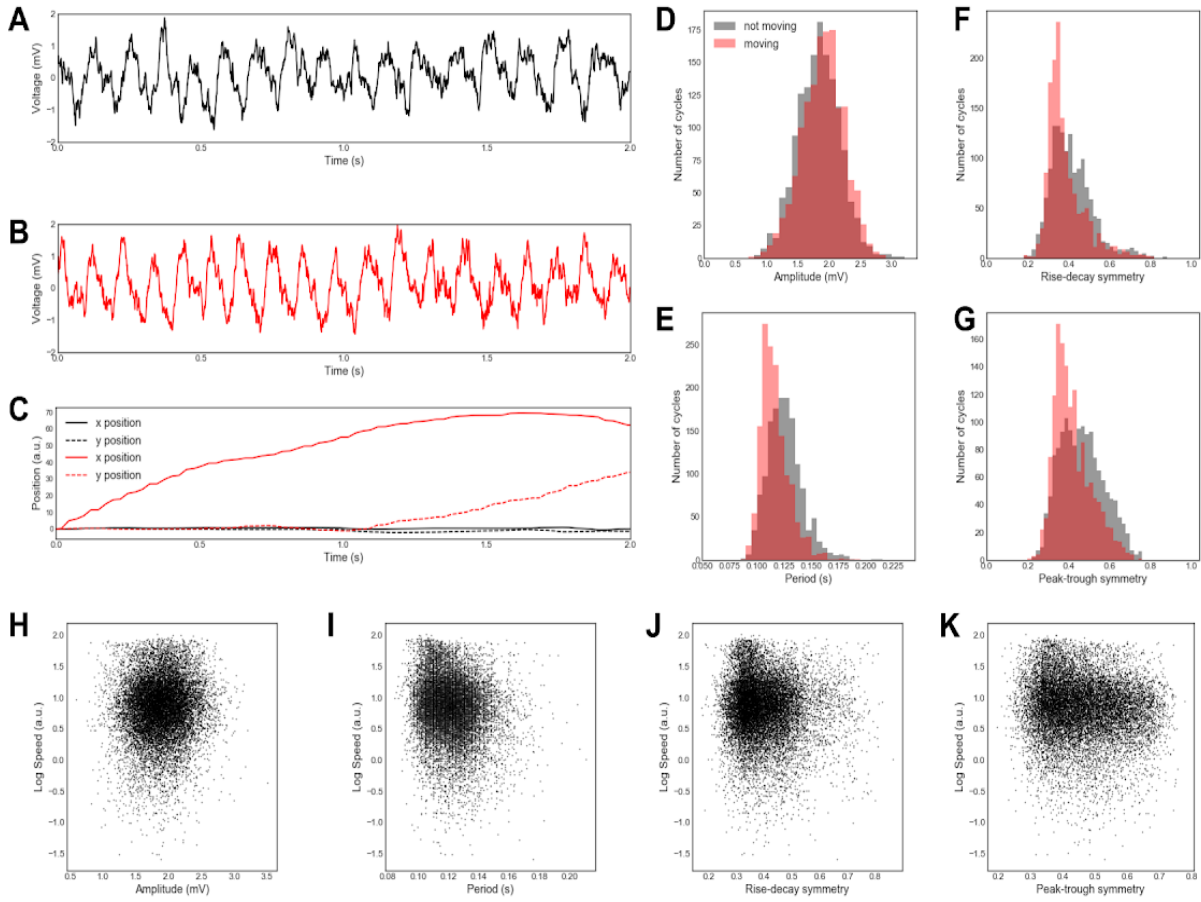


Figure 2.8. Difference between hippocampal theta oscillations between running and not running in an example rat. (A-B) Raw field potential in CA1 pyramidal layer during a period of (A) not running and (B) running during the same recording. (C) Position of the rat at rest (black) and while running (red). (D-G) Comparison of (D) amplitude, (E) period, (F) rise-decay symmetry, and (G) peak-trough symmetry of theta oscillations in the same example recording during running (red) and not running (black). Our approach shows in this recording that running is (D) not associated with a change in theta amplitude, but is associated with, (E) a shorter period (faster frequency) and, (F,G) greater asymmetry, as previously reported. (H-K) Correlations between the average speed of a rat in a cycle and the (H) amplitude ($r=0.05, p<10^{-8}$), (I) period ($r=-0.15, p<10^{-77}$), (J) rise-decay symmetry ($r=0.06, p<10^{-11}$), and (K) peak-trough symmetry ($r=0.11, p<10^{-41}$). Note that, in this example, the symmetry measures are physiological correlates of behavior (K).

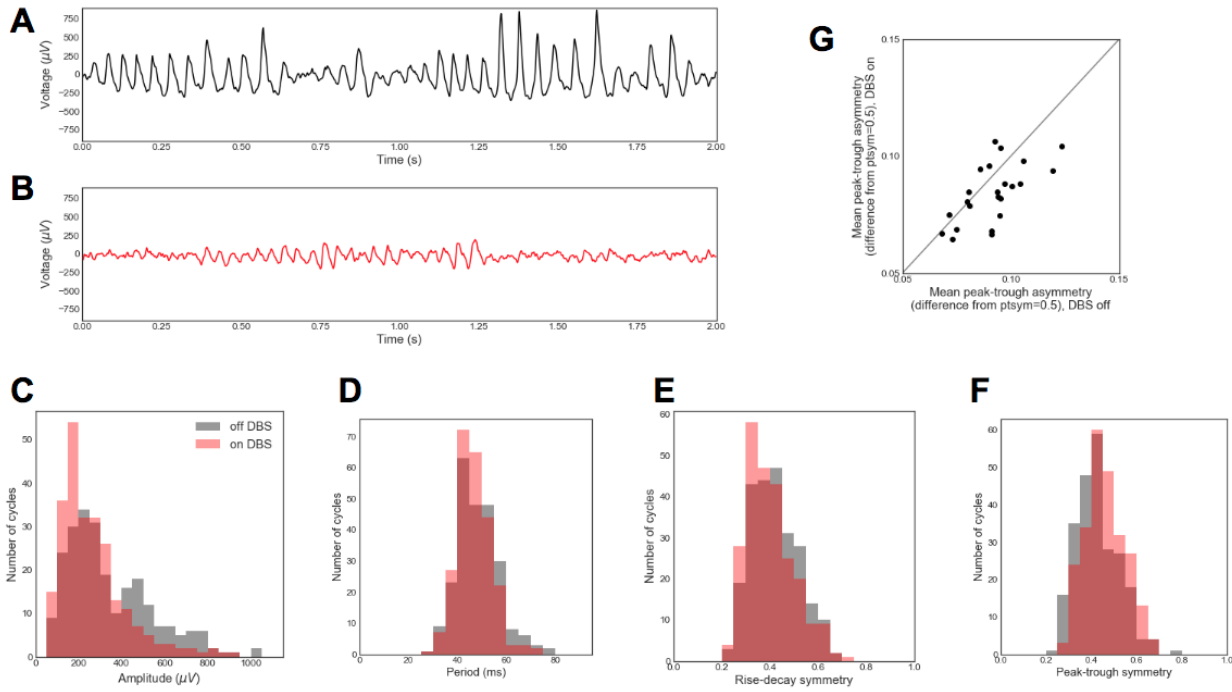


Figure 2.9. Changes in motor cortical beta oscillation shape with deep brain stimulation (DBS) treatment of Parkinson's disease. (A,B) Motor cortical electrocorticography recordings from one subject (A) before and (B) during DBS. (C-F) Comparison of (C) amplitude, (D) period, (E) rise-decay symmetry, and (F) peak-trough symmetry of beta oscillations in the same subject before (black) and during (red) DBS. (G) Comparison of peak-trough asymmetry of beta oscillations before and during DBS. This value is computed as the absolute difference between the average peak-trough symmetry and 0.5 (equal peak and trough length). Each dot represents one subject. The diagonal line represents the same peak-trough asymmetry before and during DBS. These results extend previous work, showing that peak-trough symmetry, specifically during bursts, is reduced after DBS treatment in most patients.

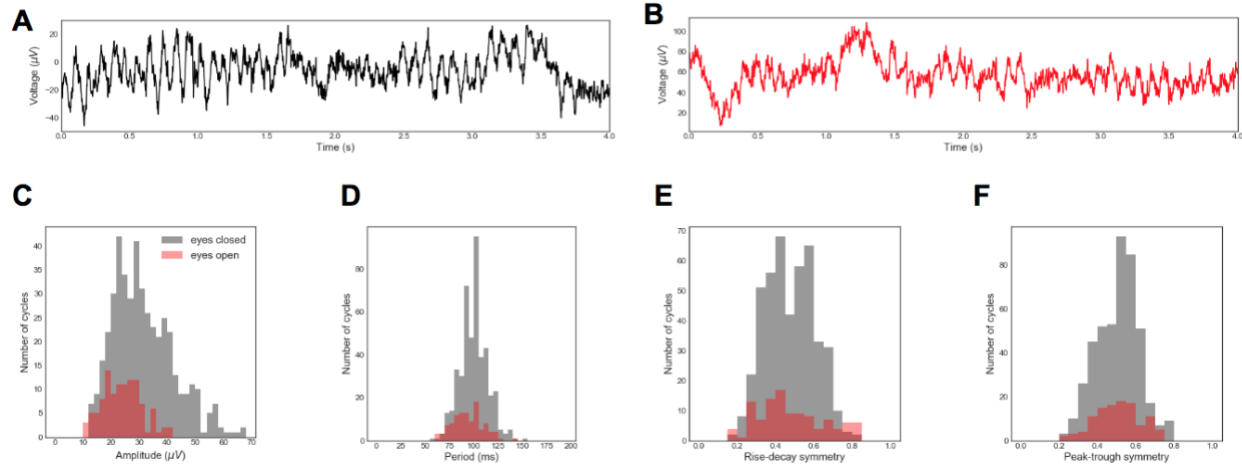


Figure 2.10. Differences in the visual alpha rhythm between periods of eyes-closed resting and eyes-open task in an example subject. (A,B) Example raw EEG traces while (A) the subject's eyes were closed and (B) the subject was performing a task with eyes open. (C-F) Comparison of (C) amplitude, (D) period, (E) rise-decay symmetry, and (F) peak-trough symmetry of alpha oscillations between recordings with eyes closed (black) and open (red). Note that in this case, the well-known effect of eyes open/closed on alpha amplitude is recapitulated by both a decrease in cycle amplitude and the number of alpha cycles detected (C). However, no substantial effect was observed on the period (D), rise-decay symmetry (E) or peak-trough symmetry (F). This demonstrates how cycle-by-cycle waveform analysis is complementary to Fourier-based approaches.

Discussion

Here we have presented a novel framework and technique for analyzing the properties of oscillations in neural signals. This cycle-by-cycle analysis approach is complementary to, and offers advantages over, conventional approaches based solely on the Fourier and Hilbert transforms. Our method offers an alternative, and arguably more intuitive, estimate of an oscillation's amplitude and frequency. These estimates are incorporated in the same framework that has previously been used to estimate rise-decay symmetry, and we have expanded it to offer a novel peak-trough symmetry measure, which quantifies an oscillatory waveform's "sharpness". Using empirical data, we showed these symmetry measures can differentiate experimental conditions. Further, using simulated data we showed that our new amplitude and frequency estimates can be more sensitive and specific than conventional techniques. This technique offers further analytic possibilities, beyond what is demonstrated in this paper. For example, rather than comparing cycles from separate recordings (e.g., DBS on vs. DBS off), cycles can be assigned to a trial and aggregated in order to analyze the effects of task conditions or correlates to responses, such as reaction time. Though we only covered four cycle features in this paper (amplitude, period, rise-decay symmetry, and peak-trough symmetry), additional features can be designed and easily added to this workflow, such as monotonicity of the flanks or gamma power. If a signal contains multiple oscillations of interest, then the analysis can be run multiple times using distinct frequency bands. Additionally, the oscillatory detection algorithm allows for quantifying bursting features such as burst duration or burst rate that may correlate meaningfully to experimental parameters.

Caveats of cycle-by-cycle analysis

Like Fourier-based analysis, there are also caveats of this cycle-by-cycle technique that need to be considered to minimize confounds. Because oscillatory features tend to be autocorrelated (Figure 2.7A), it will usually be invalid to treat each cycle as independent in

statistical tests. This is a similar caveat to trial-wise analyses, in which consecutive trials are often not independent. To bypass this issue and assess significance within a recording, the recording can be split into multiple non-overlapping segments, and a statistical test can be performed on a metric of each segment (e.g., mean difference in rdsym between conditions A and B). It is also important to keep in mind that these cycle features are not independent of one another. This can be assessed, for example, by quantifying the correlation between cycle amplitude and rise-decay symmetry to potentially uncover that higher magnitude oscillations tend to be more asymmetric, and so these features may capture redundant information. In order to tease apart some interdependencies, multiple features could be incorporated into a model to predict a condition or behavior of interest (e.g., general linear model or logistic regression), and the unique contribution of each feature can be assessed. For example, if oscillatory amplitude is greater in condition A vs. B, and amplitude is correlated with symmetry, then we will also observe that symmetry differs between conditions. However, a multidimensional model could detect whether symmetry contains any additional information beyond that provided by amplitude.

Because extrema localization is nontrivial, caution is necessary when performing analysis that considers the precise times of peaks and troughs. For example, an aperiodic process could delay the algorithm's trough localization, and so if a neuron fires most at the trough, it appears that it fires at an earlier phase when the decay period is artificially elongated. However, (Belluscio et al., 2012) reported that a rat's position could be better decoded using extrema interpolation (Figure 2.1F, black) compared to the conventional Hilbert transform-based method (Figure 2.1F, red). If it is difficult to filter the signal in order to achieve reasonable extrema localization and symmetry fidelity, then the oscillation may not be suitable for cycle-by-cycle analysis. For example, it is likely not reasonable to analyze the beta frequency band in the visual cortex because the presence of this rhythm is usually not evident in the time series, whereas alpha is prominent.

Hyperparameter selection is another notable challenge, but it is not a new one. Setting thresholds for defining oscillatory bursts requires parameter tuning in order to achieve sensible classification. This is not only true using the current method, but other methods require defining amplitude thresholds and filter lengths that will significantly impact the results (Feingold et al., 2015). For analysis of motor cortical beta and visual cortical alpha rhythms in this paper, thresholds were tuned while visualizing the algorithm's output until the oscillatory burst detection seemed most accurate. We recommend that the user runs the analysis with multiple hyperparameter choices in order to test the robustness of their results.

Cycle-by-cycle approach to defining bursts of oscillations

A key feature of this oscillatory burst detection method is that it does not need to set an amplitude threshold to define bursting periods, as is the case for previously published algorithms for burst detection (Hughes et al., 2012; Feingold et al., 2015; Watrous et al., 2017). This makes the current burst detection algorithm especially suitable for detecting oscillators that may occur at both small and large amplitudes, or may vary greatly in stationarity between recordings. In contrast using an amplitude threshold based on scaling the median oscillatory power (Feingold et al., 2015), inherently defines an upper limit on the fraction of the signal that can be oscillatory. This may not be suitable, for example, in a set of hippocampal recordings in which theta oscillations are sparse in some but are present more than 50% of the time in others.

It should be noted that the optimal hyperparameters for the current algorithm to maximize accuracy (Figure 2.4) are heavily dependent on the parameters chosen for the simulated data. For example, while the F1 score is optimized for the current signal (SNR=4) when the amplitude consistency requirement was set to 0.4 and the period consistency requirement was set to 0.55, if the signal SNR is decreased to 1, an amplitude consistency requirement of 0.3 and period consistency requirement of 0.5 optimizes F1 score. In this case, less strict requirements balanced precision and recall, likely because true oscillatory regimes are inherently more difficult to detect in the higher noise scenario. Additionally, the correlations

between simulated and measured cycle features were decreased when SNR was lowered (amplitude: $r = 0.34$, period: $r = 0.70$, rdsym: $r = 0.45$). This implies that more cycles are necessary in order to obtain an accurate estimate of cycle features when the SNR is decreased.

Very weak correlations between cycle features of adjacent bursts (Figure 2.7B-E) was a particularly surprising result. One could have expected there to be a larger correlation between features of adjacent bursts compared to features of adjacent cycles because individual cycles may be noisy estimates, and averages may lead to more accurate estimates. However, these correlations between adjacent bursts were very slight, if at all present, compared to the correlations between features of adjacent cycles. This suggests that the properties of this rat's hippocampal theta oscillation are consistent within an oscillatory burst but vary considerably from burst to burst. However, results were qualitatively different when analyzing a recording from another rat, and so this phenomena should be investigated in future, more controlled, studies.

Unlike amplitude and symmetry, we did not observe a positive correlation between the periods of adjacent cycles after controlling for the period consistency requirement of the burst detection algorithm. This is likely due to the effect of noisy extrema estimation on the period estimate. For example, if noise in the signal causes a cycle's later trough to appear delayed, the current cycle would be measured as artificially longer, and the subsequent cycle would appear artificially shorter. This would produce a negative correlation between the periods of adjacent cycles. However, we observe no correlation between consecutive periods, so it is possible that this effect is masking a positive correlation.

Instantaneous and cycle-by-cycle measure comparison

In addition to its ability to quantify waveform symmetry, we believe that the cycle-by-cycle framework's measures of amplitude and period also offer an advantage over current instantaneous estimates of amplitude and frequency. An important step in computing instantaneous amplitude is convolution with a kernel of the frequency of interest. This means

that the amplitude measure at any given point in time is actually computed using data from several cycles around that point (depending on the filter length). Because convolution is a linear operation, it is not specifically sensitive to oscillatory amplitude, but it will be strongly biased by non-oscillatory sharp transients. Instantaneous frequency, derived from instantaneous phase, is similarly based on this convolution, and fluctuates within a cycle due to the cycle's temporal dynamics. However, when applied to a relatively stationary nonsinusoidal oscillation (e.g., hippocampal theta) this will cause fluctuating within-cycle frequency estimates, which do not actually reflect a change in the theta frequency, but rather reflects its sawtooth-like waveform.

In contrast to these widely used instantaneous measures, the time-resolved estimates of amplitude and period (frequency) using cycle-by-cycle estimates are more direct and intuitive measurements of the oscillator. Specifically, the amplitude measures the mean rise and decay voltages, and the period is computed as the time between consecutive peaks of a cycle in a putative oscillatory burst. This method does not over-promise temporal resolution that it cannot reliably account for, and it is robust to issues that plague instantaneous measures like sharp transients and nonsinusoidal waveforms. Additionally, we showed that the cycle-by-cycle measures of amplitude and frequency are more robust and better at differentiating these properties in simulated oscillations (Figures 2.5-6). Specifically, both of these instantaneous measures are biased by the proportion of the signal in which the oscillator is present, so this could underlie some past reports of changes in instantaneous amplitude and frequency.

There is some empirical precedence for analyzing individual cycles of brain rhythms. (Adrian and Matthews, 1934) studied the evolution of a gamma oscillation in response to injury to the cortex of a cat. Initially, they observed rhythmic transient discharges, which gradually became more frequent and broad, producing a more sinusoidal-like rhythm. They interpreted the initial transients as bursts of activity by a few local neurons, and that this activity spread out as the transient discharges merged into a quasi-sinusoid. Therefore, each cycle could be considered as a “packet” of neural activity that can be characterized distinctly from the previous

and subsequent cycles using a cycle-by-cycle analysis framework. This view of each cycle as an informative physiological unit differs substantially from modern work on oscillations.

Conclusions

In summary, we have demonstrated a novel approach to analyzing neural oscillations using a cycle-by-cycle framework. This technique has advantages over conventional approaches that rely solely on Fourier-based techniques, including its ability to characterize oscillatory waveform symmetry and its inherent detection of whether an oscillation is present in the data or not. We demonstrate its applicability to hippocampal theta, motor cortical beta, and visual cortical alpha rhythms. Applications are not limited to the oscillations discussed here but could also include other prominent rhythms such as sensorimotor mu, visual cortical gamma, thalamocortical spindles, cortical slow oscillation, and respiratory rhythms. While this open-source analysis framework is unique in its focus on oscillatory symmetry, it is also complementary to conventional analysis of oscillatory amplitude and period, and, as such, should be a standard part of the neural oscillation analysis toolbox.

Chapter 2, in full, has been submitted for publication of the material as it currently appears in: Cole SR, Voytek B. (2018) Cycle by cycle analysis of neural oscillations. *bioRxiv*. The dissertation author was the primary investigator and author of this paper.

References

- Adrian ED, Matthews BH (1934) The interpretation of potential waves in the cortex. *J Physiol (Lond)* 81:440–471.
- Amemiya S, Redish AD (2018) Hippocampal Theta-Gamma Coupling Reflects State-Dependent Information Processing in Decision Making. *Cell Rep* 22:3328–3338.
- Amzica F, Steriade M (1998) Electrophysiological correlates of sleep delta waves. *Electroencephalogr Clin Neurophysiol* 107:69–83.
- Atallah BV, Scanziani M (2009) Instantaneous modulation of gamma oscillation frequency by balancing excitation with inhibition. *Neuron* 62:566–577.
- Bajaj V, Pachori RB (2012) Classification of seizure and non-seizure EEG signals using empirical mode decomposition. *IEEE Trans Inf Technol Biomed* 16:1135–1142.
- Belluscio MA, Mizuseki K, Schmidt R, Kempter R, Buzsáki G (2012) Cross-frequency phase-phase coupling between θ and γ oscillations in the hippocampus. *J Neurosci* 32:423–435.
- Brunn A (2004) Fourier-, Hilbert- and wavelet-based signal analysis: are they really different approaches? *J Neurosci Methods* 137:321–332.
- Buzsáki G, Czopf J, Kondákor I, Kellényi L (1986) Laminar distribution of hippocampal rhythmic slow activity (RSA) in the behaving rat: current-source density analysis, effects of urethane and atropine. *Brain Res* 365:125–137.
- Buzsáki G, Rappelsberger P, Kellényi L (1985) Depth profiles of hippocampal rhythmic slow activity ('theta rhythm') depend on behaviour. *Electroencephalogr Clin Neurophysiol* 61:77–88.
- Canolty RT, Edwards E, Dalal SS, Soltani M, Nagarajan SS, Kirsch HE, Berger MS, Barbaro NM, Knight RT (2006) High gamma power is phase-locked to theta oscillations in human neocortex. *Science* 313:1626–1628.
- Chandran K S S, Mishra A, Shirhatti V, Ray S (2016) Comparison of Matching Pursuit Algorithm with Other Signal Processing Techniques for Computation of the Time-Frequency Power Spectrum of Brain Signals. *J Neurosci* 36:3399–3408.
- Cole SR, van der Meij R, Peterson EJ, de Hemptinne C, Starr PA, Voytek B (2017) Nonsinusoidal beta oscillations reflect cortical pathophysiology in parkinson's disease. *J Neurosci* 37:4830–4840.
- Cole SR, Voytek B (2017) Brain oscillations and the importance of waveform shape. *Trends Cogn Sci (Regul Ed)* 21:137–149.
- de Hemptinne C, Swann NC, Ostrem JL, Ryapolova-Webb ES, San Luciano M, Galifianakis NB, Starr PA (2015) Therapeutic deep brain stimulation reduces cortical phase-amplitude coupling in Parkinson's disease. *Nat Neurosci* 18:779–786.

- Diez PF, Mut V, Laciar E, Torres A, Avila E (2009) Application of the empirical mode decomposition to the extraction of features from EEG signals for mental task classification. *Conf Proc IEEE Eng Med Biol Soc* 2009:2579–2582.
- Dvorak D, Fenton AA (2014) Toward a proper estimation of phase-amplitude coupling in neural oscillations. *J Neurosci Methods* 225:42–56.
- Feingold J, Gibson DJ, DePasquale B, Graybiel AM (2015) Bursts of beta oscillation differentiate postperformance activity in the striatum and motor cortex of monkeys performing movement tasks. *Proc Natl Acad Sci USA* 112:13687–13692.
- Fransen AMM, van Ede F, Maris E (2015) Identifying neuronal oscillations using rhythmicity. *Neuroimage* 118:256–267.
- Gerber EM, Sadeh B, Ward A, Knight RT, Deouell LY (2016) Non-Sinusoidal Activity Can Produce Cross-Frequency Coupling in Cortical Signals in the Absence of Functional Interaction between Neural Sources. *PLoS ONE* 11:e0167351.
- Gips B, Bahramisharif A, Lowet E, Roberts MJ, de Weerd P, Jensen O, van der Eerden J (2017) Discovering recurring patterns in electrophysiological recordings. *J Neurosci Methods* 275:66–79.
- Haller M, Donoghue T, Peterson E, Varma P, Sebastian P, Gao R, Noto T, Knight RT, Shestyuk A, Voytek B (2018) Parameterizing neural power spectra. *BioRxiv*.
- Hanslmayr S, Aslan A, Staudigl T, Klimesch W, Herrmann CS, Bäuml K-H (2007) Prestimulus oscillations predict visual perception performance between and within subjects. *Neuroimage* 37:1465–1473.
- Hentschke H, Perkins MG, Pearce RA, Banks MI (2007) Muscarinic blockade weakens interaction of gamma with theta rhythms in mouse hippocampus. *Eur J Neurosci* 26:1642–1656.
- Hughes AM, Whitten TA, Caplan JB, Dickson CT (2012) BOSC: a better oscillation detection method, extracts both sustained and transient rhythms from rat hippocampal recordings. *Hippocampus* 22:1417–1428.
- Jas M, Tour T, Şimşekli U, Re G (2017) Learning the Morphology of Brain Signals Using Alpha-Stable Convolutional Sparse Coding. *Arxiv*.
- Jones SR (2016) When brain rhythms aren't "rhythmic": implication for their mechanisms and meaning. *Curr Opin Neurobiol* 40:72–80.
- Klimesch W (1999) EEG alpha and theta oscillations reflect cognitive and memory performance: a review and analysis. *Brain Res Rev* 29:169–195.
- Kramer MA, Tort ABL, Kopell NJ (2008) Sharp edge artifacts and spurious coupling in EEG frequency comodulation measures. *J Neurosci Methods* 170:352–357.

- Latimer KW, Yates JL, Meister MLR, Huk AC, Pillow JW (2015) NEURONAL MODELING. Single-trial spike trains in parietal cortex reveal discrete steps during decision-making. *Science* 349:184–187.
- Lee S, Jones SR (2013) Distinguishing mechanisms of gamma frequency oscillations in human current source signals using a computational model of a laminar neocortical network. *Front Hum Neurosci* 7:869.
- Lewis LD, Weiner VS, Mukamel EA, Donoghue JA, Eskandar EN, Madsen JR, Anderson WS, Hochberg LR, Cash SS, Brown EN, Purdon PL (2012) Rapid fragmentation of neuronal networks at the onset of propofol-induced unconsciousness. *Proc Natl Acad Sci USA* 109:E3377-86.
- Liang H, Bressler SL, Desimone R, Fries P (2005) Empirical mode decomposition: a method for analyzing neural data. *Neurocomputing* 65–66:801–807.
- Lozano-Soldevilla D, Ter Huurne N, Oostenveld R (2016) Neuronal Oscillations with Non-sinusoidal Morphology Produce Spurious Phase-to-Amplitude Coupling and Directionality. *Front Comput Neurosci* 10:87.
- Massimini M, Huber R, Ferrarelli F, Hill S, Tononi G (2004) The sleep slow oscillation as a traveling wave. *J Neurosci* 24:6862–6870.
- Mazaheri A, Jensen O (2010) Rhythmic pulsing: linking ongoing brain activity with evoked responses. *Front Hum Neurosci* 4:177.
- McFarland WL, Teitelbaum H, Hedges EK (1975) Relationship between hippocampal theta activity and running speed in the rat. *J Comp Physiol Psychol* 88:324–328.
- Miller KJ, Leuthardt EC, Schalk G, Rao RPN, Anderson NR, Moran DW, Miller JW, Ojemann JG (2007) Spectral changes in cortical surface potentials during motor movement. *J Neurosci* 27:2424–2432.
- Mizuseki K, Diba K, Pastalkova E, Teeters J, Sirota A, Buzsáki G (2014) Neurosharing: large-scale data sets (spike, LFP) recorded from the hippocampal-entorhinal system in behaving rats [version 2; referees: 4 approved]. F1000Res.
- Nelli S, Ittipuripat S, Srinivasan R, Serences JT (2017) Fluctuations in instantaneous frequency predict alpha amplitude during visual perception. *Nat Commun* 8:2071.
- Orosco L, Lacić E, Correa AG, Torres A, Graffigna JP (2009) An epileptic seizures detection algorithm based on the empirical mode decomposition of EEG. *Conf Proc IEEE Eng Med Biol Soc* 2009:2651–2654.
- Park C, Looney D, Naveed ur Rehman, Ahrabian A, Mandic DP (2013) Classification of motor imagery BCI using multivariate empirical mode decomposition. *IEEE Trans Neural Syst Rehabil Eng* 21:10–22.
- Pastalkova E, Itskov V, Amarasingham A, Buzsáki G (2008) Internally generated cell assembly sequences in the rat hippocampus. *Science* 321:1322–1327.

- Peterson EJ, Voytek B (2017) Alpha oscillations control cortical gain by modulating excitatory-inhibitory background activity. *BioRxiv*.
- Pfurtscheller G, Stancák A, Edlinger G (1997) On the existence of different types of central beta rhythms below 30 Hz. *Electroencephalogr Clin Neurophysiol* 102:316–325.
- Pietersen ANJ, Patel N, Jefferys JGR, Vreugdenhil M (2009) Comparison between spontaneous and kainate-induced gamma oscillations in the mouse hippocampus in vitro. *Eur J Neurosci* 29:2145–2156.
- Pittman-Polletta B, Hsieh W-H, Kaur S, Lo M-T, Hu K (2014) Detecting phase-amplitude coupling with high frequency resolution using adaptive decompositions. *J Neurosci Methods* 226:15–32.
- Ray S, Jouny CC, Crone NE, Boatman D, Thakor NV, Franaszczuk PJ (2003) Human ECoG analysis during speech perception using matching pursuit: a comparison between stochastic and dyadic dictionaries. *IEEE Trans Biomed Eng* 50:1371–1373.
- Samaha J, Postle BR (2015) The Speed of Alpha-Band Oscillations Predicts the Temporal Resolution of Visual Perception. *Curr Biol* 25:2985–2990.
- Scheffer-Teixeira R, Tort AB (2016) On cross-frequency phase-phase coupling between theta and gamma oscillations in the hippocampus. *elife* 5.
- Sherman MA, Lee S, Law R, Haegens S, Thorn CA, Hämäläinen MS, Moore CI, Jones SR (2016) Neural mechanisms of transient neocortical beta rhythms: Converging evidence from humans, computational modeling, monkeys, and mice. *Proc Natl Acad Sci USA* 113:E4885-94.
- Siapas AG, Lubenov EV, Wilson MA (2005) Prefrontal phase locking to hippocampal theta oscillations. *Neuron* 46:141–151.
- Sławińska U, Kasicki S (1998) The frequency of rat's hippocampal theta rhythm is related to the speed of locomotion. *Brain Res* 796:327–331.
- Teeters JL, Harris KD, Millman KJ, Olshausen BA, Sommer FT (2008) Data sharing for computational neuroscience. *Neuroinformatics* 6:47–55.
- Trimper JB, Stefanescu RA, Manns JR (2014) Recognition memory and theta-gamma interactions in the hippocampus. *Hippocampus* 24:341–353.
- Uhlhaas PJ, Singer W (2010) Abnormal neural oscillations and synchrony in schizophrenia. *Nat Rev Neurosci* 11:100–113.
- van Dijk H, van der Werf J, Mazaheri A, Medendorp WP, Jensen O (2010) Modulations in oscillatory activity with amplitude asymmetry can produce cognitively relevant event-related responses. *Proc Natl Acad Sci USA* 107:900–905.
- Vaz AP, Yaffe RB, Wittig JH, Inati SK, Zaghloul KA (2017) Dual origins of measured phase-amplitude coupling reveal distinct neural mechanisms underlying episodic memory in the human cortex. *Neuroimage* 148:148–159.

- Voytek B, Knight RT (2015) Dynamic network communication as a unifying neural basis for cognition, development, aging, and disease. *Biol Psychiatry* 77:1089–1097.
- Watrous AJ, Miller J, Qasim SE, Fried I, Jacobs J (2017) Phase-tuned neuronal firing encodes human contextual representations for navigational goals. *BioRxiv*.
- Womelsdorf T, Valiante TA, Sahin NT, Miller KJ, Tiesinga P (2014) Dynamic circuit motifs underlying rhythmic gain control, gating and integration. *Nat Neurosci* 17:1031–1039.

CHAPTER 3: Hippocampal theta bursting and waveform shape reflect CA1 spiking patterns

Abstract

Brain rhythms are nearly always analyzed in the spectral domain in terms of their power, phase, and frequency. While this conventional approach has uncovered spike-field coupling, as well as correlations to normal behaviors and pathological states, emerging work has highlighted the physiological and behavioral importance of multiple novel oscillation features. Oscillatory bursts, for example, uniquely index a variety of cognitive states, and the nonsinusoidal shape of oscillations relate to physiological changes, including Parkinson's disease. Open questions remain regarding how bursts and nonsinusoidal features relate to circuit-level processes, and how they interrelate. By analyzing unit and local field recordings in the rodent hippocampus, we uncover a number of significant relationships between oscillatory bursts, nonsinusoidal waveforms, and local inhibitory and excitatory spiking patterns. Bursts of theta oscillations are surprisingly related to a decrease in pyramidal neuron synchrony, and have no detectable effect on firing sequences, despite significant increases in neuronal firing rates during periods of theta bursting. Theta burst duration is predicted by the asymmetries of its first cycle, and cycle asymmetries relate to firing rate, synchrony, and sequences of pyramidal neurons and interneurons. These results provide compelling physiological evidence that time-domain features, of both nonsinusoidal hippocampal theta waveform and the theta bursting state, reflects local circuit properties. These results point to the possibility of inferring circuit states from local field potential features in the hippocampus and perhaps other brain regions with other rhythms.

Introduction

Oscillations are one of the most prominent features of neural field potential recordings (Buzsáki and Draguhn, 2004; Cohen, 2017). Consequently, they have been extensively studied for decades and their features are known to relate to physiological processes, pathologies, and

behavior (Klimesch, 1999; Ward, 2003; Uhlhaas and Singer, 2010; Buzsáki and Wang, 2012; Womelsdorf et al., 2014; Cohen, 2017). Throughout this research, clear evidence has emerged showing that local spiking probability is coupled to phases of the oscillatory local field (Li et al., 1952), resulting in theories about how these oscillations may function to aid communication among brain networks (Fries, 2005; Roux and Uhlhaas, 2014; Voytek and Knight, 2015; Peterson and Voytek, 2018). Though we have a good understanding of how current sources summate and manifest as field potential fluctuations (forward model), interpretations of these oscillations is challenging because many different biological processes can yield the same field potential fluctuation (inverse model) (Buzsáki et al., 2012; Herreras et al., 2015; Herreras, 2016; Pesaran et al., 2018).

There is a general consensus that the prominent contributor to the low frequency component of the field potential (<100 Hz) is synaptic activity (Mitzdorf, 1985; Einevoll et al., 2007, 2013; Mazzoni et al., 2015; Haider et al., 2016), but interpretation remains complicated because the resultant field potential is significantly influenced by anatomical geometry, connectivity, tissue electrical properties, and nonsynaptic ionic currents (Lindén et al., 2010, 2011; Buzsáki et al., 2012; Reimann et al., 2013; Herreras, 2016; Ness et al., 2016). Though relatively simple models can capture certain relationships between the field potential and neuronal activity (Miller et al., 2009; Mazzoni et al., 2015; Gao et al., 2017), the details of the relationship between the two are mostly unknown.

Beyond the uncertainties of the specific current sources, the commonly used metrics of analysis (e.g., narrowband power) are often not specific and can be confounded with many different properties of the raw data, beyond that which is being conceptualized. For example, an increase in 10 Hz power can be a consequence of an increase in power of a: 1) stationary 10 Hz oscillator, 2) transient 10 Hz oscillator, 3) 5 Hz nonsinusoidal oscillator, 4) white noise, 5) a sharp transient, and more (Haller et al., 2018). Analyses of oscillations have mainly applied

techniques based on the Fourier transform, which parametrizes signals as sums of sine waves at varying frequencies (Bruns, 2004; Cohen, 2017; Pesaran et al., 2018).

However, after sparse interest in the past (Jasper, 1948; Amzica and Steriade, 1998), recent interest has emerged regarding significance of the nonsinusoidal and nonstationary features of brain rhythms (Feingold et al., 2015; Fransen et al., 2015; Jones, 2016; Cole and Voytek, 2017; Jas et al., 2017; Lozano-Soldevilla, 2018; Sweeney-Reed et al., 2018; van Ede et al., 2018). Careful and thorough inspection of the neural signal, in the time-domain, is necessary in order to precisely characterize changes in neural oscillations and avoid potential pitfalls of spectral representations. By better parametrizing our features of interest, we are better suited to disentangle separate neural processes. To improve on conventional techniques, we have recently demonstrated a method of analyzing neural oscillations on a cycle-by-cycle basis, wherein we first determine when the oscillator is present, and then measure not only its power and frequency, but also its waveform symmetries (see Figure 3.1) (Cole and Voytek, 2018).

Parameterizing oscillation features on a cycle-by-cycle basis in this manner allows us to interrogate novel physiological relationships between neuronal spiking activity and multiple oscillatory features heretofore unexplored. It seems reasonable to assume that the properties of the oscillatory waveform correlate with the properties of the underlying physiological generators. There are several microcircuit motifs that produce oscillations (Womelsdorf et al., 2014), so changes of the specific motif or its components should manifest as changes in the waveform.

For example, three alpha rhythms in the gustatory cortex that each have distinct behavioral correlations can be differentiated by features of their waveforms (Tort et al., 2010). It is intuitive to interpret changes in oscillation amplitude and frequency as changes in the number of active neurons, or the time between consecutive activations, respectively (Pesaran et al., 2018). However, a conceptual relationship between the oscillatory waveform and neuronal activity is less apparent. Previously we hypothesized that the effect of deep brain stimulation treatment of Parkinson's disease on making motor cortical beta oscillations more symmetric

resulted from a desynchronization effect of the stimulation treatment (Cole et al., 2017). Given spike-field coupling, it may be expected that waveform symmetry would reflect the relative activity of different neuronal populations—e.g., excitatory and inhibitory ensembles or intra- and interlaminar interactions—given that the time windows during which neuron populations are active covaries with cycle symmetry.

Leveraging our novel cycle-by-cycle analysis approach, we sought to address several specific physiological hypotheses. First, we hypothesize that cycle-by-cycle variability in waveform shape can explain variance in neuronal firing rates, synchrony, and sequences. Next, we hypothesize that the presence of an oscillation, or burst, will change the statistics of local single-unit activity by increasing spiking, and spike synchrony, while stabilizing spike sequences. Finally, we hypothesize that the duration of an oscillatory burst can be predicted by the features of the very first oscillatory cycle in the burst.

To test these hypotheses, we analyzed a public data set of simultaneous recordings of the hippocampal local field potential (LFP) and spiking data from neuron units in region CA1 (Mizuseki et al., 2014). This data set was chosen because of the physiological properties of the hippocampal theta rhythm: its asymmetric waveform is stereotyped yet variable (Buzsáki et al., 1985; Belluscio et al., 2012; Trimper et al., 2014; Amemiya and Redish, 2018), there is established spike-field coupling with many hippocampal neuronal populations (Mizuseki et al., 2009, 2011; Belluscio et al., 2012), and the symmetry of the theta waveform has been linked to memory and representation (Trimper et al., 2014; Amemiya and Redish, 2018).

Materials & Methods

Python code to replicate the figures in this paper are shared at
https://github.com/voytekresearch/Cole_2018_theta.

Data collection

Local field potentials (LFPs) and neuronal spiking were recorded from the CA1 pyramidal layer of the hippocampus in rats, and downloaded from the “hc3” dataset on the

Collaborative Research in Computational Neuroscience (CRCNS) database (Teeters et al., 2008; Mizuseki et al., 2014). Briefly, extracellular recordings were made using multichannel silicon probes with 8 channels per shank (vertical distance: 20 μ m) and either 4 or 8 shanks (200 μ m spacing). Spikes were sorted at the original sampling rate (20 kHz or 32.552 kHz) and labeled as putative pyramidal neurons or putative interneurons based on their action potential waveforms and cross-correlations. LFP recordings were downsampled to 1250 Hz or 1252 Hz. Nine rats in this database had recordings from CA1. Recordings were downloaded from 3 sessions for each rat on 3 different days, if possible (27 total recordings sessions). Recordings were roughly chosen to maximize the number of simultaneously recorded pairs of interneurons.

The LFP recordings analyzed were taken from the deepest contacts on each shank. Normally, the traces from all recording contacts looked very similar due to their close proximity, but if the deepest contact significantly deviated from the other contacts, the next deepest contact was chosen. Recordings were collected from between 2 and 11 shanks in CA1 during each session. Shanks were analyzed independently (152 total shanks), and neurons were referenced to the theta recordings from the shank on which it was detected.

Five recordings analyzed also had simultaneous tracking data of the rat's position. The speed during a theta cycle was computed as the distance traveled between the two peaks divided by the period. In order to analyze changes in hippocampal theta patterns during movement (Figure 3.3), theta cycles were conservatively classified as "moving" if the speed during that cycle was above the 90th percentile, and "stationary" if the speed was below the 10th percentile.

Theta cycle analysis

The presence and features of hippocampal theta oscillations were analyzed using our previously described cycle-by-cycle analysis approach (Cole and Voytek, 2018). Briefly, a broad bandpass filter (1-25 Hz) was applied and then peaks and troughs were localized (Figure 3.1A, dots) in order to segment the signal into theta (4-10 Hz) cycles. Note this broad bandpass filter

did not substantially affect the theta oscillation asymmetry of interest (compare gray and black traces in Figure 3.1A). A peak-to-peak segmentation was chosen because spiking was concentrated around the trough (Figure 3.4D,E) and so bursts of spiking around the trough would be analyzed in a single cycle (rather than 2 cycles if a trough-to-trough segmentation was used). For each cycle, four features were computed as shown in Figure 3.1B: amplitude, period, rise-decay symmetry, and peak-trough symmetry. Rise and decay midpoints were defined as the time points at which the voltage was halfway between the adjacent peak and trough voltages. These midpoints were used to represent the boundaries between peak and trough segments. Rise-decay symmetry is defined as the fraction of the period that is comprised of the rise phase. Peak-trough symmetry is similarly defined as the fraction of the period comprised of the peak phase, but the period in this case is bounded by consecutive rise midpoints instead of consecutive peaks.

It is important to appreciate that the neural oscillations are not present during the entire recording (Feingold et al., 2015; Jones, 2016; Lundqvist et al., 2016). Therefore, it is useful to determine the segments of the signal in which the oscillation is present because measuring theta features of a signal segment without a prominent theta oscillation will add noise to the analysis (Cole and Voytek, 2018). Therefore, only cycles that are determined to be part of a theta oscillatory burst were analyzed. However, the task of identifying the segments of the signal with oscillatory components is challenging and currently unsolved (Kosciessa et al., 2018). It is unclear if there are discrete times in which an oscillator is on and off, so perhaps there is no objective solution.

The approach for burst detection has been thoroughly described previously (Cole and Voytek, 2018), but briefly, a segment (cycle) of the signal was determined to be part of an oscillatory burst if its amplitude and period were comparable to adjacent cycles, and if its rise and decay flanks were mainly monotonic. Like with any burst detection algorithm, it relies on thresholds that must be semi-arbitrarily defined (Hughes et al., 2012; Feingold et al., 2015). In

order to address this limitation, we ran our analysis with a range of burst detection parameters to assure that results were not simply dependent on one specific choice of settings. For the results shown in the main paper, the parameters were chosen as those that optimized the F1 score (equally weighted precision and recall) of a simulated signal with a signal-to-noise ratio that appears roughly similar to the hippocampal theta rhythm (Cole and Voytek, 2018). Thresholds were set such that adjacent cycles' amplitudes and periods could be no more than 60% and 45% different, respectively, and the cycle flanks must be at least 80% monotonic. With these settings, theta oscillations were detected to be present 50-85% of the time across recordings.

Neuronal spiking analysis

Spikes were previously sorted using KlustaKwik (Harris et al., 2000) and clustering was manually adjusted using autocorrelograms, cross-correlograms, and spike waveform shape (Mizuseki et al., 2014). Spikes were compared to the LFP recorded from the same shank. Neurons with fewer than 100 spikes during putative theta oscillations were excluded from analysis, resulting in a data set of 119 putative interneurons and 760 putative pyramidal neurons.

A measure of spike-field coupling (SFC) was computed for each neuron. The instantaneous phase of the LFP was estimated by interpolating between peaks (phase 0), troughs (π , $-\pi$), rise midpoints ($-\pi/2$), and decay midpoints ($\pi/2$), and the phase was determined at each spike time (Siapas et al., 2005). The distribution of these spike phases (50 circular bins, each of width $\pi/25$) was normalized by the distribution of phases in the recording in order to compute a firing rate in each phase bin. This normalization is critical because the consistent rise-decay asymmetry of the theta waveform results in more timepoints having positive phases compared to negative phases. SFC was then parametrized by the magnitude and phase of the mean vector, defined by summing each spike as a unit vector at the phase of firing. Only spikes during theta bursts were included, as the theta phase is only reliable during these periods.

These SFC estimates differed from conventional techniques that do not have this theta burst requirement and also estimate the phase using the Hilbert transform, which has been shown to be systematically biased by waveform shape (Dvorak and Fenton, 2014).

In order to compare neuronal activity to hippocampal theta features (e.g., symmetry), firing rate was computed for each cycle by dividing the number of spikes in the cycle by the period. The correlation between firing rate and each theta feature was quantified by fitting a general linear model (GLM) to predict the firing rate from the cycle features. A one-sample Wilcoxon signed rank test was then used to assess if there is a significant bias in these model coefficients.

Neuron synchrony and sequence analysis

Spike timing relationships between simultaneously recorded pairs of neurons were analyzed in order to test if the theta rhythm contained information about the firing patterns of the CA1 population. All simultaneously recorded pairs of neurons on the same shank were analyzed to identify events in which the two neurons fired within 20 ms of one another (a synchronous event). The neuron with fewer spikes was used as the reference neuron, and if the other neuron did not fire within 20 ms of a spike, that spike was labelled as a nonsynchronous event. If two synchronous events occurred in the same cycle, only one was maintained. If a synchronous and nonsynchronous event occurred in the same cycle, all events in that cycle were excluded. A neuron pair was analyzed if at least 100 synchronous events occurred during the theta rhythm (431 putative pyramidal neuron pairs, 46 putative interneuron pairs). The mean symmetries of cycles were calculated separately for synchronous and nonsynchronous events, and the difference was recorded for analysis across all neuron pairs (Figure 3.6A-D).

The fraction of spikes that were synchronous with the other neuron in the pair was computed separately during and not during theta bursts. The effect of the theta rhythm on synchrony was measured as the difference between these fractions (Figure 3.7F,G). This analysis of fractions necessitated sufficient samples in order to prevent one or a few events

from significantly biasing results. Therefore, at least 25 synchronous and nonsynchronous events were required for both theta and non-theta periods (496 putative pyramidal neurons pairs, 45 putative interneurons pairs). Note that this is more neurons than were available for analysis with the aforementioned restriction of 100 synchronous events during the theta rhythm, because this requirement could be as few as 50 (25 pre + 25 post) synchronous events during the theta rhythm.

Synchronous events between neuron pairs (see above) were further analyzed to assess the neuron sequence. Synchronous events were defined as “pre” or “post” if the reference neuron fired before or after the other neuron. However, there are important cases in which a synchronous event should be excluded from synchrony analysis. For example, if the reference neuron fires a burst of 5 spikes, followed by a spike from the other neuron, this should not count as 5 “pre” sequences when doing statistics because these samples are not independent. In this case, in which multiple reference spikes occur within 20 ms, only the reference spike that is closest to the other neuron’s spike is kept for analysis. Additionally, If two reference spikes are recorded within 40 ms and are assigned opposite sequences, both events are removed from analysis. The ratio of “pre” and “post” sequences was computed, such that the ratio was always greater than 1, since the identity of the reference neuron was arbitrary. Thus, this “sequence ratio” corresponds to the relative bias of the neuron pair to fire among the two sequences. For example, a neuron pair in which neuron 1 fires before neuron 2 ($1 \rightarrow 2$) 50 times and neuron 1 fires after neuron 2 ($2 \rightarrow 1$) 75 times would have a sequence ratio of 1.5 ($75:50 = 1.5:1$).

Results

Cycle-by-cycle theta oscillation characterization

Field potential recordings from all shanks in CA1 were analyzed to characterize their hippocampal theta waveforms. A broad bandpass filter (1-25 Hz) was applied to the raw data in order to improve extrema localization while preserving the general shape of the theta rhythm (compare the gray and black traces in Figure 3.1A). After peaks, troughs, and flank midpoints

were identified (see Methods), four features of each theta cycle were quantified (Figure 3.1B): 1) amplitude, 2) period, 3) rise-decay symmetry (“rdsym”), and 4) peak-trough symmetry (“ptsym”). Distributions of the cycle features are shown for an example recording. Note that the theta amplitude tended to be 2-3 mV (Figure 3.1C) and its period ranged between roughly 100 and 150 ms (7 - 10 Hz, Figure 3.1D). Notably, the theta cycles exhibited consistent symmetry biases. Specifically, the rise segment tended to be shorter than the decay ($rdsym < 0.5$, Figure 3.1E), and the peak segment tended to be shorter than the trough ($ptsym < 0.5$, Figure 3.1F).

We analyzed the consistency of these theta features across recordings. Recordings from most rats yielded cycle amplitudes around 2 mV, but recordings from 3 rats exhibited average amplitudes of 4-7 mV (Figure 3.1G). The average theta period was generally consistent across different recordings from the same rat (Figure 3.1H) and ranged roughly between 110 ms to 135ms (7.5-9 Hz). Rise-decay symmetry and peak-trough symmetry were below 0.5 in the vast majority of recordings ($rdsym: 93\%$, $ptsym: 95\%$), representing that the stereotyped theta waveform with short rises and short peaks is reliable across rats (Figure 3.1I-J).

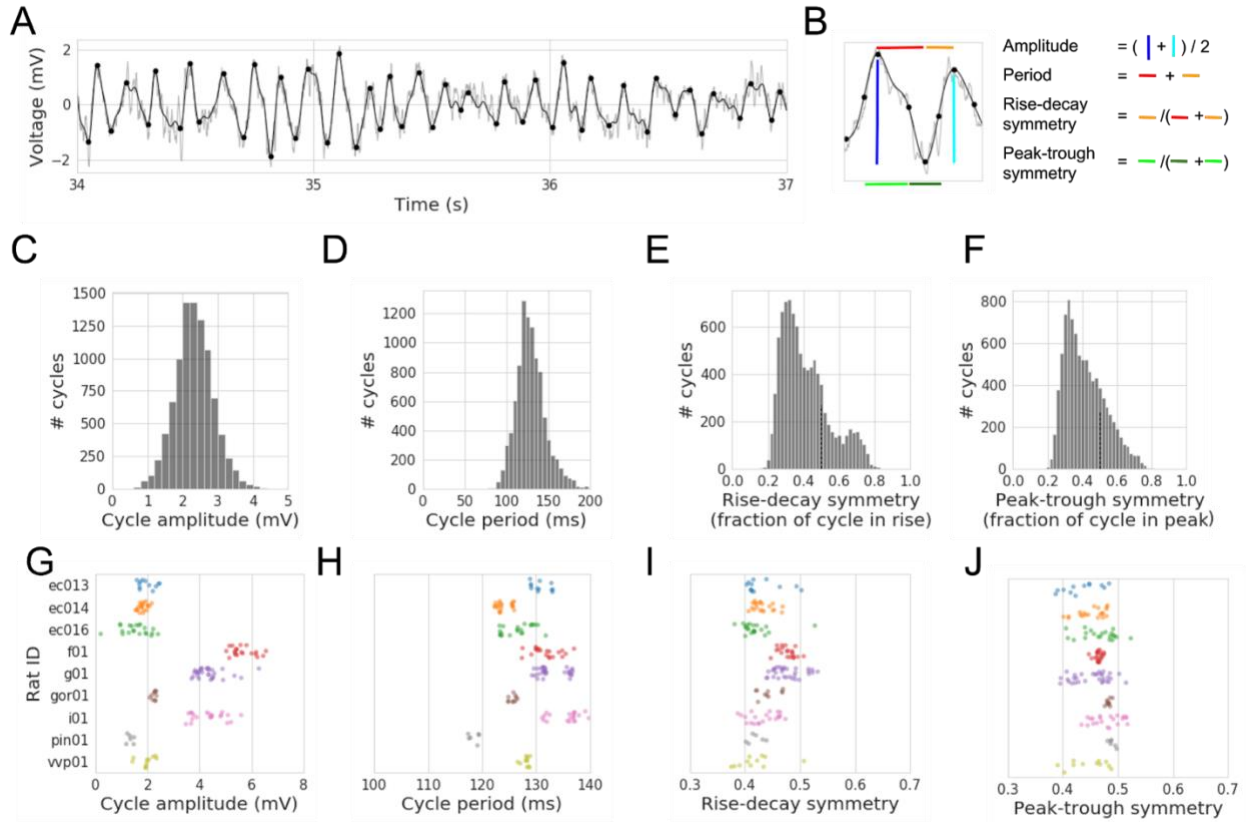


Figure 3.1. Cycle-by-cycle characterization of the rodent hippocampal theta rhythm. (A) Example trace of the local field potential recorded in the pyramidal layer of hippocampal CA1. The raw signal is plotted in light gray, and the black line shows the result of a broad bandpass filter (1-25 Hz). This broad bandpass filter reduces the high frequency noise that complicates extrema localization while still largely preserving the shape of the theta waveform. Identified peaks and troughs are denoted as black dots. (B) Illustration of how four features of the theta cycle are computed. Black dots in the middle of the rise and decay flanks denote the flank midpoints, which demarcate the boundary between peak and trough phases. Amplitude is computed by averaging the rise voltage (dark blue line) and decay voltage (light blue line). The period is the time between consecutive peaks (red and orange lines together). Rise-decay symmetry is defined as the fraction of the period in the rise phase (orange line). Peak-trough symmetry is defined as the relative length of time of the last peak (light green line) compared to the central trough (dark green line). (C-F) Distributions of (C) amplitude, (D) period, (E) rise-decay symmetry, and (F) peak-trough symmetry across all theta cycles in the example recording. Note that both symmetry measures are mostly below 0.5, indicating that these are non-sinusoidal, asymmetric oscillations wherein the rise tends to be shorter than the decay, and the peak tends to be shorter than the trough. (G-J) Distributions of the average (G) amplitude, (H) period, (I) rise-decay symmetry, and (J) peak-trough symmetry across all CA1 recordings in 9 different rats (each color). Note in (G) that 3 rats (f01, g01, and i01) have larger measured theta rhythms and in (H) that the recordings from the same rat tend to have consistent periods (i.e., steady theta frequency across recordings). Almost all recordings have, on average, relatively short (I) rise phases and (J) peak phases.

Correlations between cycle features

When analyzing the significance of a single cycle feature, it is important to also account for the other cycle features if they are correlated with one another. Therefore, we characterized how the different cycle features correlated to one another. In Figures 3.2A-C, we explore in a single recording how each other cycle feature relates to rise-decay symmetry. Note that these distributions have significant structure that indicates mutual information (i.e., dependence) between these features. In order to identify a consistency in this structure, we summarized each pairwise relationship with a nonparametric Spearman correlation coefficient (ρ) for each recording, and compared these ρ values across recordings. We observed that theta oscillations that were more rise-decay asymmetric (shorter, or faster, rise) had a larger amplitude (Figure 3.2D, Wilcoxon signed rank test, $N = 152$, $W = 2740$, $p < 10^{-7}$), shorter period (higher frequency, Figure 3.2E, $W = 2835$, $p < 10^{-7}$), and had relatively longer peaks (Figure 3.2F, $W = 28$, $p < 10^{-25}$).

Additionally, there were significant autocorrelations for each of the cycle features (Figure 3.2G). Theta amplitude (black line) is the most autocorrelated in the nearest cycles, followed by cycle period, and finally the cycle symmetries. Note that the dip in autocorrelation between periods of adjacent cycles reflects noise in peak localization, such that when a peak is detected artificially later, the latter cycle is artificially shorter and the former cycle is artificially longer. The relatively weak autocorrelations of rise-decay symmetry and peak-trough symmetry could reflect that these symmetry measures are inherently more noisy than estimates of amplitude and period and/or that oscillation asymmetry can better temporally resolve changes in physiology or behavior compared to amplitude and frequency.

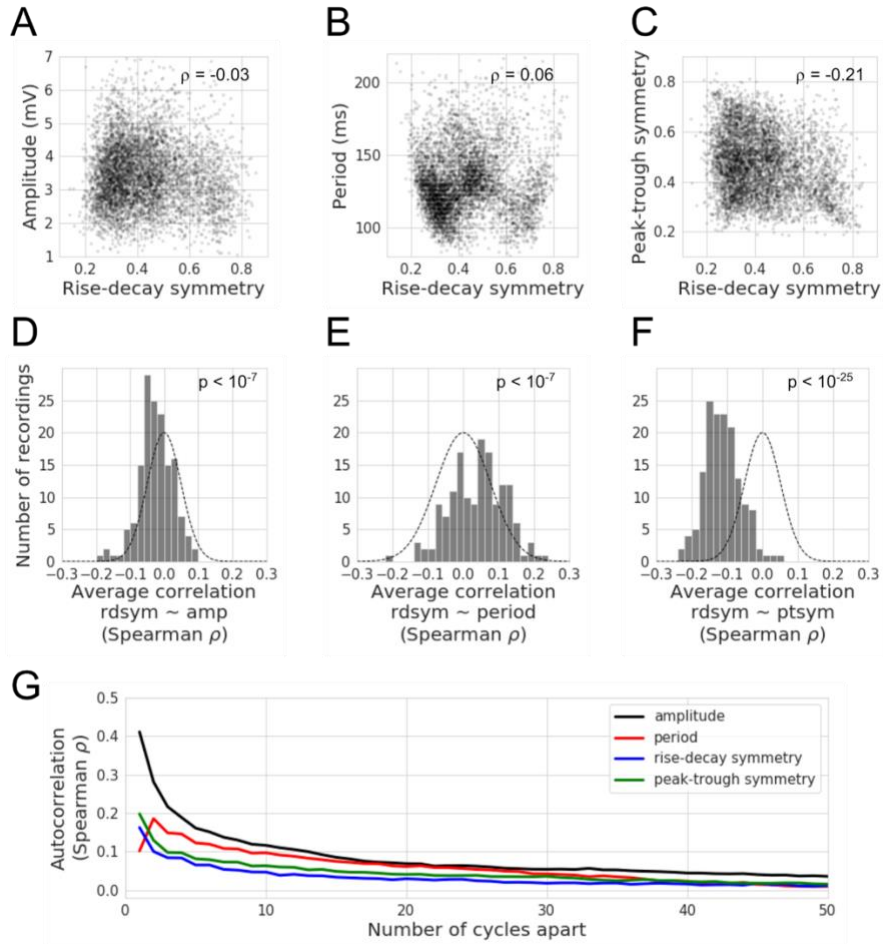


Figure 3.2. Correlations between features of hippocampal theta cycles. (A-C) For an example recording (same as in Figure 3.1A-F), there are significant correlations between the different cycle features. Each dot represents a single theta cycle. The rise-decay symmetry is slightly correlated to the cycle (A) amplitude, (B) period, and (C) peak-trough symmetry. (D-F) Distributions of Spearman correlation coefficients (ρ) across hippocampal recordings that relate the theta rise-decay symmetry on each cycle to its (D) amplitude, (E) period, and (F) peak-trough symmetry. Note that cycles that have a relatively short rise ($rdsym < 0.5$) tend to (D) have greater amplitude, (E) shorter periods, and (F) longer peaks (generally more peak-trough symmetric). Gaussian outlines are centered at zero with a variance equal to the distribution of the data, to visually compare results against the null hypothesis. (G) Lines show the correlation of features between cycles separated by increasing temporal distance (x-axis). The autocorrelations plotted are the averages across all 9 rats. Note that autocorrelations slowly decay over time, but remain consistently positive for several seconds (average cycle ~ 130 ms). Amplitude (black) is the most autocorrelated, followed by the period (red), and the symmetries (blue: rise-decay, green: peak-trough) suggesting that there is more cycle-by-cycle independence of the symmetry metrics compared to amplitude or period.

Rat movement and theta cycle features

For five sessions between two rats, spatial position data was available, and periods of fast movement and nonmovement were identified by computing the rat's speed during each theta cycle (see Methods). Average theta cycle features were computed during these two types of periods, and significant differences were observed in all of them (Figure 3.3). Specifically, relative to nonmovement, while the rat was moving, the hippocampal theta oscillation was larger in amplitude (Figure 3.3A, $N = 35$, $W = 78$, $p < 10^{-3}$), had a shorter period (faster frequency, Figure 3.3B, $W = 0$, $p < 10^{-6}$), was more rise-decay asymmetric (Figure 3.3C, $W = 4$, $p < 10^{-6}$), and was more peak-trough asymmetric (Figure 3.3D, $W = 0$, $p < 10^{-6}$). Note these p-values should be interpreted with caution because the data come from only 2 different rats, so they do not necessarily generalize across the population. That said, these results are consistent with past reports of large, asymmetric, and relatively fast theta oscillations during running (Buzsáki et al., 1985; Hentschke et al., 2007; Belluscio et al., 2012; Amemiya and Redish, 2018).

In addition to these univariate statistics, we also fit a general linear model (GLM) to predict the rat's speed during a theta cycle based on the four cycle features. This complementary approach is necessary because the cycle features are correlated to one another (Figure 3.2). Across sessions, the coefficients for period, rise-decay symmetry, and peak-trough symmetry were consistently negative, but the predictive sign of amplitude was not consistent (Figure 3.3E).

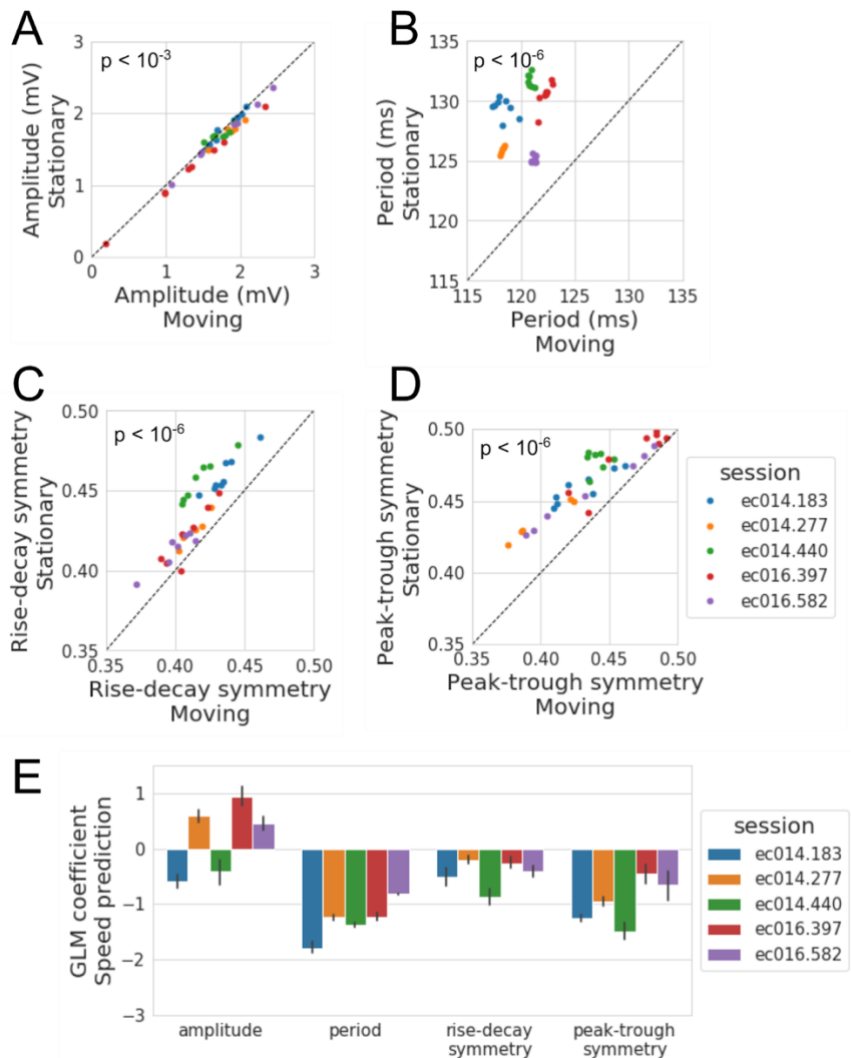


Figure 3.3. Comparison of hippocampal theta cycle features between movement and nonmovement. (A-D) Average properties of the decile of cycles in which the rat moved the most (x-axis, “Moving”) compared to the decile of cycles in which the rat moved the least (y-axis, “Stationary”). Each dot represents the recording from one shank in CA1, and each color represents a unique recording session for which position tracking was available from two rats. Note that in (A), the points mostly lie below unity (black line), indicating that theta amplitude is, on average, greater when the rat is moving. Additionally, while the rat is moving, (B) the theta period tends to be shorter, and (C) the cycles become both more rise-decay asymmetric (shorter rise) and (D) peak-trough asymmetric (shorter peak). (E) For each recording, a linear model was fit to predict the rat’s speed from the 4 cycle features. The bars show the average coefficient for each feature across all CA1 shanks simultaneously recorded in a session (error bars represent 95% confidence interval). Note that the amplitude feature does not consistently predict speed, but faster movement in all sessions was predicted by shorter periods and asymmetry values (i.e., more asymmetric with shorter rises and shorter peaks).

Spike-field coupling between CA1 neurons and hippocampal theta

We now shift focus to how the features of the hippocampal theta rhythm relate to the network activity of neurons in hippocampal region CA1. Individual units were previously sorted and classified as putative pyramidal neurons and interneurons (Mizuseki et al., 2014) (see Methods). Figure 3.4A shows an example simultaneous recording of the theta oscillation (black) and spiking of a putative pyramidal neuron (red). As expected, the pyramidal neurons have significantly lower firing rates (Figure 3.4B, generally below 2 Hz) than the interneurons (Figure 3.4C, generally 20-40 Hz).

The correlation between neuron firing and the phase of the theta rhythm (i.e., spike-field coupling, SFC) has been well established in hippocampal neurons (Mizuseki et al., 2009, 2011). Figure 3.4A shows an example of this correlation for a pyramidal neuron with particularly strong SFC. This neuron consistently fires during the rise phase of the field potential ($-\pi/2$). Indeed, most pyramidal neurons fire at higher rates in the rise phase compared to the decay phase. Figure 3.4D shows the magnitude and phase of coupling as a black vector for each neuron, and the mean vector (red, $0.11e^{0.77\pi}$) shows that the preferred phase for pyramidal neuron activity is in the rise period soon after the trough. In contrast, interneurons tend to fire in the decay phase prior to the trough (Figure 3.4E, mean vector $0.14e^{0.85\pi}$).

In our analysis, we estimated SFC using the waveform-based phase estimate (see Methods) and only during periods of the signal in which theta was bursting. However, conventional SFC analysis uses portions of the signal in which the oscillation is not present, which negatively biases the coupling magnitude estimate. Additionally, conventional approaches use a phase estimate based on the Hilbert Transform, which biases the phase estimate due to its narrowband filtering requirement and the nonsinusoidal nature of the theta rhythm. In other words, burst detection and cycle-by-cycle parametrization enhances instantaneous phase and SFC estimates.

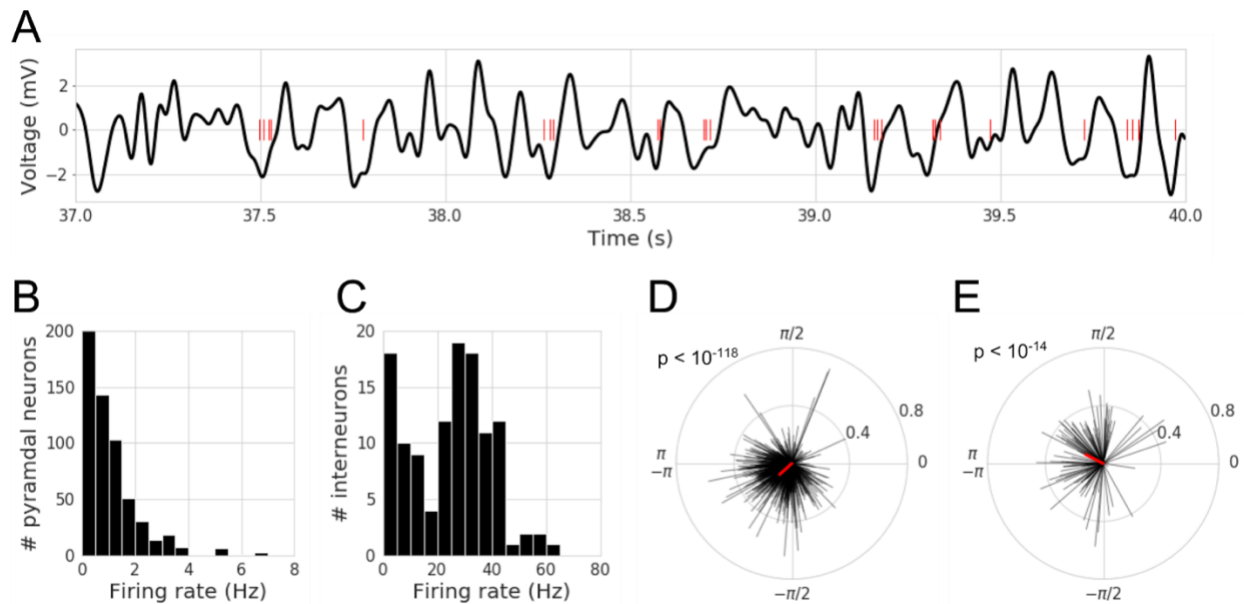


Figure 3.4. Spike-field coupling of CA1 neurons to the hippocampal theta rhythm. (A) Example CA1 field potential recording (black) and spike times (red) for a putative pyramidal neuron that tends to fire during the rise phase of theta oscillations. (B-C) Distributions of firing rates for all putative (B) pyramidal neurons, and (C) interneurons in the data set. Most pyramidal neurons have a firing rate below 2 Hz, and most interneurons fire between 20 and 40 Hz. (D-E) Distributions of spike-field coupling for putative (D) pyramidal neurons, and (E) interneurons. Each black line represents the coupling of a single neuron. The direction of the line reflects the phase at which the neuron is most likely to fire (phase 0 is the peak), and the magnitude of the line reflects the strength of the coupling. The red line shows the mean vector. Note that pyramidal neurons are most likely to fire after the trough (phase π/π), while interneurons most likely fire before the trough.

Neuronal firing rate covaries with theta cycle features

As a complement to the well-known SFC effects, we analyzed the data in order to further identify relationships between neuronal firing and the LFP. GLMs were fit to predict the firing rate of neurons during each cycle from their normalized (z-scored) cycle features: amplitude, period, rise-decay symmetry (rdsym), and peak-trough symmetry (ptsym). The model coefficients (β) were recorded for each model and distributions of model coefficients across all neurons are shown in Figure 3.5A (pyramidal neurons) and 5B (interneurons). Both neuron types had higher firing rates during theta cycles with higher amplitude (pyramidal: N=760, W = 74416, $p < 10^{-30}$, $\beta_{avg} = 0.06$, interneuron: W = 1072, $p < 10^{-10}$, $\beta_{avg} = 2.04$), shorter periods (pyramidal: W = 66820, $p < 10^{-37}$, $\beta_{avg} = -0.08$, interneuron: W = 337, $p < 10^{-16}$, $\beta_{avg} = -2.42$), relatively short rise phases (rdsym, pyramidal: W = 117298, $p < 10^{-5}$, $\beta_{avg} = -0.04$, interneuron: W = 613, $p < 10^{-14}$, $\beta_{avg} = -1.41$), and relatively short peak phases (ptsym, W = 97066, $p < 10^{-14}$, $\beta_{avg} = -0.04$, interneuron: W = 1366, $p < 10^{-8}$, $\beta_{avg} = -0.96$). Not only is neuronal firing rate reflected by the commonly analyzed amplitude and frequency features, but it is also reflected significantly in the waveform symmetry.

We noticed that the cycle features that correlated to increased movement (larger, faster, more asymmetric) were in the same direction as those correlated to increased firing rate (Figure 3.3). Therefore, for the five sessions for which position tracking data was available, we tested if the symmetry features were still significant predictors of firing rate after the speed of the rat was accounted for. The GLM coefficients for these symmetry features remained consistently negative for both pyramidal neurons (N=760, rdsym: W = 19523, $p < 10^{-94}$; ptsym: W = 14535, $p < 10^{-102}$) and interneurons (N=119, rdsym: W = 50, $p < 10^{-19}$; ptsym: W = 90, $p < 10^{-19}$).

Note that the coefficient magnitude was largest for period and amplitude and smaller for the symmetry features, potentially indicating that the former features are generally more informative than the latter. Also note that the coefficients were an order of magnitude higher for

the firing rate of interneurons, and the GLM's average explained variance was 21% for interneurons compared to only 2.9% for pyramidal neurons. This difference can largely be attributed to the differences in firing rates between these neuron types, i.e., there will be high variance in the firing rate of a pyramidal neuron between theta bursts simply because these neurons fire more sparsely. This can be confirmed by noting a high correlation between a neuron's firing rate and the GLM's explained variance (Pearson $r = 0.74$).

When exploring univariate relationships, we noticed that effect sizes increased substantially if analysis was done with the basic unit of a burst as opposed to a single cycle. This is visualized for the relationship between firing rate and rise-decay symmetry for an example neuron. Rise-decay symmetry explains greater variance in firing rate when the fundamental unit is a burst (Figure 3.5D, $\rho = -0.49$) compared to if the fundamental unit is a cycle (Figure 3.5C, $\rho = -0.17$).

One potential explanation for a correlation between a neuron's firing rate and theta asymmetry is that a neuron will fire at a higher rate if more time is spent in its preferred firing phase. In other words, if a single cycle of an oscillation has a very fast decay time, then each phase in that decay will last for less time than a more sinusoidal oscillation of the same frequency. Therefore, a neuron that prefers to fire during the decay phase will have a negative correlation between firing rate and rise decay symmetry (shorter rise, longer decay: increased firing). Therefore, we computed the circular-linear correlation (Berens, 2009) between a neuron's preferred phase and this correlation coefficient and found that this distribution was significantly nonuniform ($\rho = 0.20$, $p < 10^{-7}$). Specifically, there was a significant negative correlation between this correlation coefficient (firing rate \sim rdsym) and the difference between a neuron's preferred phase and the theoretical rise midpoint phase ($-\pi/2$) (Figure 3.5E, Spearman correlation, $\rho = -0.14$, $p < 10^{-4}$). These statistics support the aforementioned hypothesis that a neuron will fire at a higher rate if a longer part of the theta cycle is spent in its preferred phase.

This is extended by exploring the correlation between a neuron's firing rate and theta peak-trough symmetry. Again, the circular-linear correlation found a nonuniform distribution in the neuron's preferred phase and the correlation coefficient between firing rate and peak-trough symmetry ($\rho = 0.22$, $p < 10^{-9}$). Analogous to rise-decay symmetry, there was a significant negative correlation between this correlation coefficient (firing rate \sim ptsym) and the difference between a neuron's preferred phase and the peak (Figure 3.5F, Spearman correlation, $\rho = -0.13$, $p < 10^{-3}$). Given these results, the nonsinusoidal waveform shape of the hippocampal theta rhythm seems to index the degree to which different neuronal populations are active, depending on their preferred firing phase.

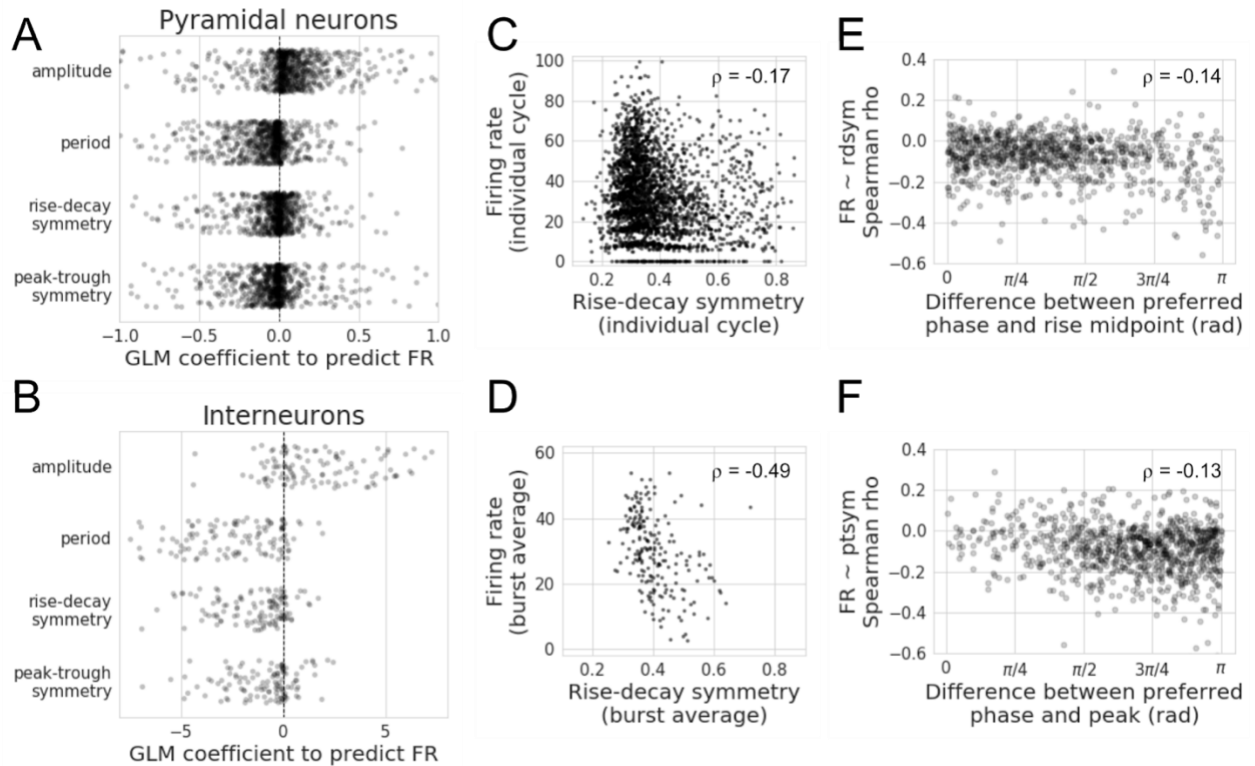


Figure 3.5. Theta cycle features are correlated to neuronal firing rate. (A-B) Linear models were fit to predict the firing rate of each neuron during a theta burst based on the average features of the component cycles. Each dot denotes the GLM coefficient for the model of the firing rate of an individual (A) pyramidal neuron or (B) interneuron. Increased theta amplitude and decreased theta period are associated with increased firing rates in both pyramidal neurons and interneurons. More rise-decay asymmetric (shorter rise) oscillations are also associated with faster firing rates in both pyramidal neurons and interneurons. More peak-trough asymmetric (shorter peak) oscillations are associated with faster firing rates in both pyramidal neurons and interneurons. (C-D) Visualization for a single putative interneuron that fires at a higher rate during cycles that are more rise-decay asymmetric (shorter rise), emphasizing the overall trend across all interneurons. Each dot represents one cycle in (C), or one burst in (D). Note that this correlation is even clearer when firing rate and rise-decay symmetry are averaged over a burst of cycles (D) compared to a single cycle (C). (E) The correlation between each neuron's firing rate and rise-decay symmetry is compared to its preferred firing phase. Specifically, the x-axis shows the difference between the preferred firing phase and the rise midpoint ($-\pi/2$). Notice the negative correlation, indicating that the more that neurons prefer the decay phase, the more their firing rates tend to be stronger when the decay period is longer. (F) Similar to (E) but comparing the difference between a neuron's preferred phase and the peak to the correlation coefficient between firing rate and peak-trough symmetry. This negative correlation indicates that if a neuron's preferred phase is the trough, its firing rate is stronger when the trough period is longer.

Theta oscillation features reflect neuronal synchrony and sequence

In addition to the firing rates of individual neurons, the coordinated activation of a population of neurons is thought to be important for neural computation. In particular, it is theorized that neurons transmit information more efficiently when they fire synchronously as opposed to asynchronously (König et al., 1996; Stevens and Zador, 1998; Salinas and Sejnowski, 2000; Roy and Alloway, 2001). We investigated how features of the theta rhythm may correlate to synchrony between pairs of neurons. If these features differentiate degrees of synchrony, this would suggest that these oscillatory features contain important information about the function of the underlying neural oscillator.

Pairs of neurons were defined as firing synchronous when they fired within 20 ms of one another (see Methods). Compared to nonsynchronous spiking, during synchronous events, theta oscillations had increased amplitudes (pyramidal: $N = 431$ pairs, $W = 24119$, $p < 10^{-17}$, 2.1% average amplitude increase; interneuron: $N = 46$ pairs, $W = 179$, $p < 10^{-4}$, 4.2% average amplitude increase) and shorter periods (pyramidal: $W = 30573$, $p < 10^{-9}$, 0.9% average period decrease; interneuron: $W = 26$, $p < 10^{-7}$, 3.0% average period decrease). Additionally, synchronous interneuronal spiking tends to occur during both more rise-decay asymmetric (Figure 3.6A, $W = 123$, $p < 10^{-5}$, 3.2% average decrease) and peak-trough asymmetric cycles (Figure 3.6B, $W = 358$, $p = 0.046$, 0.8% average decrease). The relationship between pyramidal neuron synchrony and asymmetry was weaker, if at all present (Figure 3.6C, rdsym: $W = 43440$, $p = 0.23$, 0.3% average decrease; Figure 3.6D, ptsym: $W = 39459$, $p = 0.006$, 0.5% average decrease). Together, these results show that theta cycle features contain some information about neuronal synchrony.

We further investigated if synchrony between a simultaneously recorded pyramidal neuron and interneuron correlated to theta cycle features. We found similar trends as for pairs of interneurons such that pyramidal-inhibitory synchrony was related to higher amplitude, faster period, and more asymmetric theta cycles ($N = 517$ pairs; amplitude: $W = 32508$, $p < 10^{-23}$, 2.7%

average amplitude increase; period: $W = 25841$, $p < 10^{-32}$, 1.8% average period decrease; rise-decay symmetry: $W = 51641$, $p < 10^{-5}$, 0.8% average decrease; peak-trough symmetry: $W = 47218$, $p < 10^{-8}$, 1.0% average decrease).

In addition to the importance of neuronal synchrony, the relative timing between neuron activations (sequence) is also theorized to reflect meaningful aspects of neural computation (Skaggs and McNaughton, 1996; Wehr and Laurent, 1996; Yu and Margoliash, 1996; Pastalkova et al., 2008). For example, neural circuit activation may be qualitatively different when neuron 1 (N1) fires before neuron 2 (N2) compared to when N1 fires after N2. Similarly, two oscillatory processes may be considered qualitatively different if in one, N1 and N2 have a regular sequence while in the second, N1 and N2 do not have a consistent firing sequence. Because the designation of N1 versus N2 is arbitrary, we measured sequence consistency as a “sequence ratio”, which was the ratio of synchronous instances in which N1 fired before N2 to when N1 fired after N2 (see Methods).

This allows us to analyze if the theta cycle features contained information about the underlying neuronal sequences. This could indicate that the symmetry of cycles may reflect differences in the state of the neuronal network and its computational roles. This would help explain a recent result in which neuronal activity could be used to decode current position better during more asymmetric (shorter rise) hippocampal theta cycles, and future position better during more symmetric cycles (Amemiya and Redish, 2018). In an example pair of neurons, the theta oscillation is mostly asymmetric (short rise) when N1 fires after N2, but more symmetric when N1 fires before N2 (Figure 3.6E, $U = 950$, $p = 0.028$). In another example neuron pair, the theta oscillation is more peak-trough asymmetric (short peak) when N1 fires before N2, but the oscillation is more symmetric when N1 fires after N2 (Figure 3.6F, $U = 1098$, $p = 0.001$).

We tested the significance of these sorts of effects across all eligible neuron pairs in our data set (see Methods). For each neuron pair, the distribution of cycle features was determined separately for the two sequences (N1 before N2, and N1 after N2), and a nonparametric,

unpaired two-sample test (Mann-Whitney U) was applied to test if there was a significant difference in the cycle feature distribution between the two sequence events. The number of neuron pairs with a significant difference in cycle feature distribution ($p < 0.05$) was then compared to the number of neuron pairs expected by chance to have a significant effect (5%) using a binomial test (Figure 3.6G). It is notable that each cycle feature significantly correlated with firing sequence for both pyramidal neurons (amplitude: 41/278 pairs, $p < 10^{-9}$, period: 53/278 pairs, $p < 10^{-16}$, rdsym: 26/278 pairs, $p = 0.002$, ptsym: 34/278 pairs, $p < 10^{-5}$) and interneurons (amplitude: 17/45 pairs, $p < 10^{-10}$, period: 23/45 pairs, $p < 10^{-17}$, rdsym: 8/45 pairs, $p = 0.002$, ptsym: 8/45 pairs, $p = 0.002$). Because spike order is arbitrary, we cannot overinterpret the results, though we can say there are consistent cycle feature differences for different spike sequences. These results were qualitatively similar when the time window of a “synchronous event” was varied between 10 ms and 50 ms. Furthermore, results were similar when investigating the sequence of neuron pairs consisting of one pyramidal neuron and one interneuron, and all tests withstood controls for multiple hypothesis testing by false discovery rate (FDR) correction (Benjamini and Hochberg, 1995).

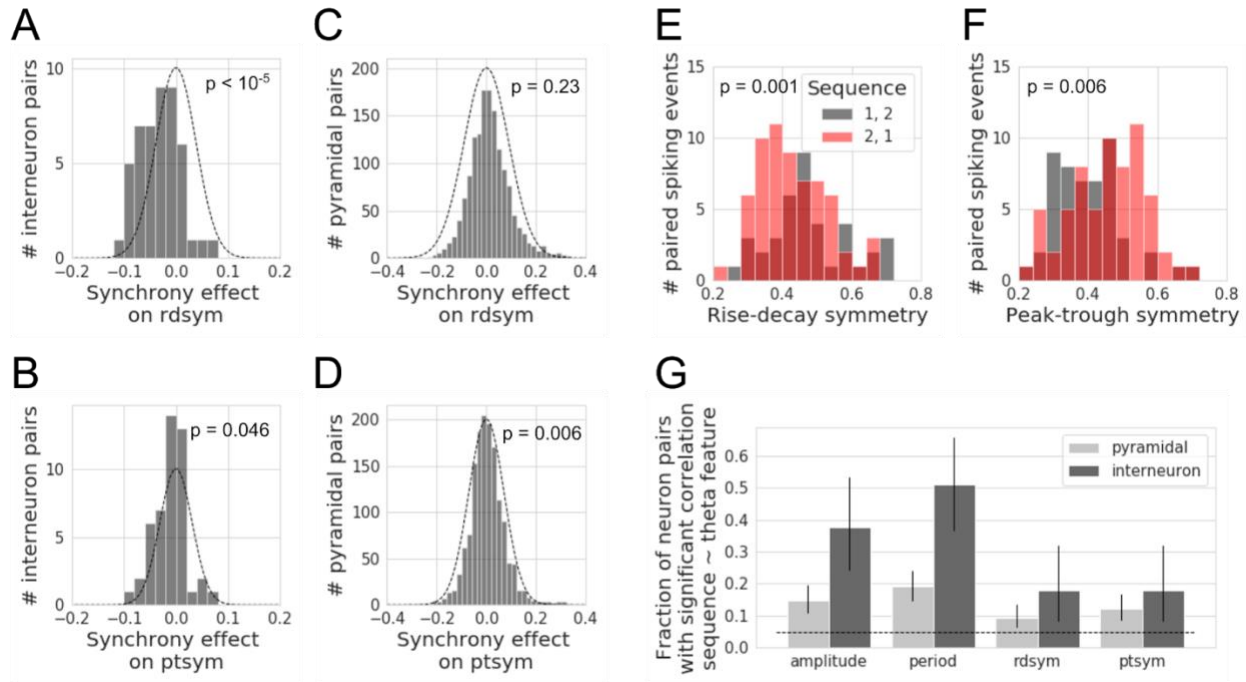


Figure 3.6. Neuronal synchrony and sequence are correlated with theta cycle features. (A-B) Distributions of the difference in (A) rise-decay symmetry and (B) peak-trough symmetry between synchronous events compared to nonsynchronous events for putative pairs of interneurons. Gaussian outlines are mean of 0 and std equal to the distribution of the data, to visually compare results against the null hypothesis. (C-D) Same as (A-B) but for pyramidal neurons, which do not have a strong relationship between their synchrony and the (C) rise-decay symmetry or (D) peak-trough symmetry of the ongoing hippocampal theta rhythm. (E-F) Example pairs of putative pyramidal neurons showing significantly different distributions of (E) rise-decay symmetry or (F) peak-trough symmetry during cycles with one sequence compared to the opposite sequence. (G) Fraction of neuron pairs with a significant relation (One-sample Wilcoxon signed rank test, $p < 0.05$) between the sequence of firing and the theta cycle features. Note that the firing sequence of neuron pairs significantly relates to all four theta cycle features, and the effect is stronger for pairs of putative interneurons. Error bars denote the 95% binomial confidence interval for the number of significant neuron pairs. The dotted line denotes 5% of neurons that, by chance, would have a significant result.

Relationship between theta bursting and cycle features

It is important to acknowledge that oscillations are not present in the signal at all points in time (Jones, 2016). This holds true for the hippocampal theta rhythm, perhaps the most stationary neural oscillation recorded in awake, behaving mammals, yet there are still periods in which it is clearly absent from the LFP. We used a burst detection algorithm (see Methods) to determine the time periods in which the theta oscillation was present. Figure 3.7A shows the distribution of burst duration throughout the data set. There was a minimum requirement of 3 cycles for an oscillatory period to be considered as a burst.

We used the burst detection method to test if there is a systematic (perhaps causal) relationship between the features of the first cycle in a burst and the burst duration. This could be the case if the properties of a specific physiological process that is related to oscillatory stability is detectable in the cycle features. For each recording, we fit a GLM to predict the burst duration from the amplitude, period, and symmetries of the first cycle. Features were normalized using a z-score relative to all cycles in that recording. We then assessed the consistency in the GLM coefficients by computing the coefficient distributions across recordings (Figure 3.7B).

Hippocampal theta bursts tended to be longer when the first cycle has a larger amplitude ($N = 152$, $W = 2886$, $p < 10^{-7}$, average coefficient = 0.67), shorter period ($W = 1262$, $p < 10^{-16}$, average coefficient = -0.78), is more rise-decay asymmetric (shorter rise, $W = 2924$, $p < 10^{-6}$, average coefficient = -0.33), or is more peak-trough asymmetric (shorter peak, $W = 3250$, $p < 10^{-5}$, average coefficient = -0.33). Therefore, all four cycle features are significantly predictive of the duration of the theta burst and together explain 4.9% of the variance in burst duration. Coefficients were qualitatively similar when speed was added as an additional predictor to the model for the neuronal firing rate during the sessions that contained position information (Figure 3.3). This suggests that these specific cycle features (high amplitude, short period, asymmetric) are indicative of a neural state in which the theta oscillation is more stable in time.

Segmenting the recordings into bursts also allows for comparing consecutive bursts. It is feasible that adjacent bursts would have similar features to one another, or for the cycle features to be relatively independent. The latter scenario would suggest that each burst of a theta oscillation is like an independent event that is unrelated to the previous burst of theta, which would have significant functional implications. To analyze this, we computed the average cycle features across all cycles in each burst. In most cases, we observe a positive correlation between the cycle features of adjacent bursts (Figure 3.7C). However, it is important to note that this is not always the case. There is not a significant correlation between adjacent bursts for average: amplitude in 22% of recordings, period for 30% of recordings, rise-decay symmetry for 47% of recordings, and peak-trough symmetry for 36% of recordings. Therefore, the dependence between adjacent theta bursts may depend on the specific context of the recording and local physiology.

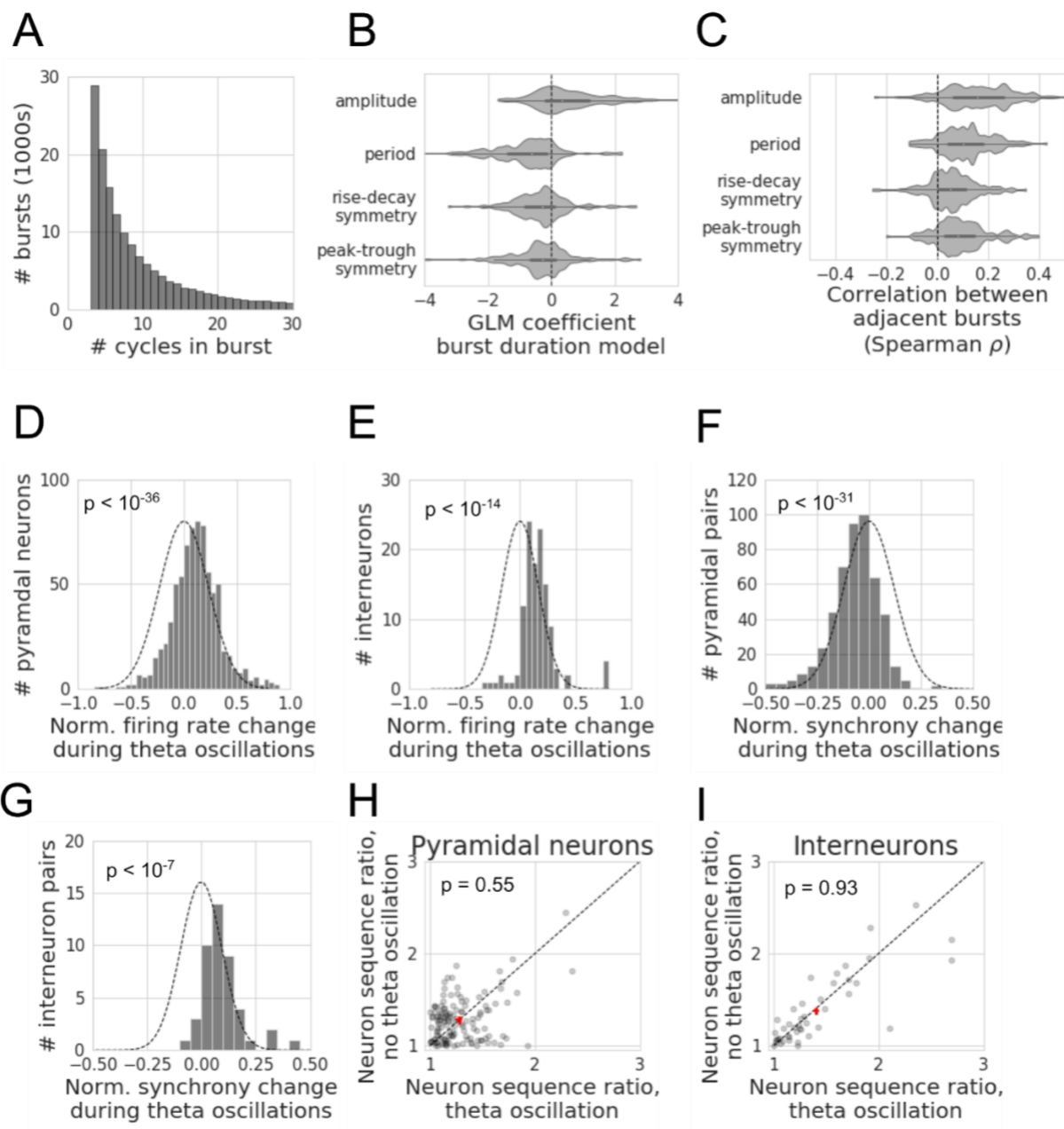
Theta oscillation presence relates to the firing rate, synchrony, and sequence of neuronal activity

Analysis of theta bursts on this dataset additionally allowed us to examine how CA1 neuronal network activity differed between periods of the recording with and without theta oscillations. For instance, both pyramidal neurons and inhibitory neurons tend to fire more during periods of the signal in which theta oscillations were detected (Figure 3.7D,E). This result was expected because of the established correlation between running and both increased firing rate and presence of theta activity (McNaughton et al. 1983). The presence of a theta oscillation is associated with an average 11% increase in pyramidal neurons ($N=760$, $W=67682$, $p < 10^{-36}$), and 15% increase in interneuron, firing rates ($N=119$, $W=569$, $p < 10^{-14}$). Again, we also studied synchrony between neurons. On average, synchronous events in a pair of pyramidal neurons had a 7% decreased likelihood during a theta oscillation burst (Figure 3.7F, $N = 496$ pairs, $W = 23829$, $p < 10^{-31}$) despite the increase in pyramidal neuron firing rate during theta oscillations. In

contrast, synchronous events were on average 9% more likely during a theta oscillation for pairs of interneurons (Figure 3.7G, N = 45 pairs, W = 43, p < 10⁻⁷).

We next analyzed if there was a difference in the relative consistency of neuron sequences between recording segments with and without theta oscillations. We hypothesized there to be a more consistent firing pattern during time periods with a prominent oscillation, with the idea that the oscillatory process is regularly firing a sequence of neurons. However, across all neuron pairs with a sufficient number of sequence observations (see Methods), there was no difference in the sequence consistency during segments with and without a theta oscillation (Figure 3.7H,I, pyramidal: N = 133, W = 4188, p = 0.55, interneuron: N = 44, W = 487, p = 0.93). This result was robust when varying the time window of sequence analysis between 10 ms and 50 ms.

Figure 3.7. Characteristics of theta bursts and their relationship to cycle features and neuronal firing. (A) Distribution of durations of all theta bursts in the data set. The minimum burst duration was set to 3 cycles. (B) General linear models were fit to predict the duration of a theta burst based on the features of the first cycle. One model was computed for each hippocampal theta recording, and the distribution of coefficients across all recordings are shown. Note that theta bursts tend to be longer when cycles have higher amplitudes, shorter periods, and are more asymmetric (shorter rises and shorter peaks). (C) Correlation between average cycle features in adjacent bursts. Histograms show the distribution of Spearman correlation coefficients across all recordings. As indicated by distributions shifted to the right of zero, adjacent bursts tend to have more similar amplitudes, periods, and symmetries. (D-E) Distributions of the normalized difference in neuronal firing rate between periods of theta oscillation and no theta oscillation for putative (D) pyramidal neurons and (E) interneurons. Note that the distributions are shifted to the right of zero, reflecting that putative excitatory and inhibitory neurons fire more when a theta oscillation is present. Gaussian outlines are mean of 0 and *std* equal to the distribution of the data, to visually compare results against the null hypothesis. (F-G) Distributions of the normalized difference in neuronal synchrony between periods of theta oscillation and no theta oscillation for putative (F) pairs of pyramidal neurons or (G) pairs of interneurons. Note that during a theta oscillation, synchronous events between pyramidal neurons were less likely to occur (average 7% decrease), but more likely for interneuron pairs (average 9% increase). (H-I) Comparison of putative (H) pyramidal neuron and (I) interneuron sequence ratio during periods of theta oscillation and no theta oscillation. The “sequence ratio” measures the consistency in firing between a pair of neurons (neuron 1 and neuron 2, i.e., 1→2, or 2→1). Therefore, a sequence ratio of 1 represents both sequences occurred an equal number of times, and a sequence ratio of x means that one order was x times as common as the opposite order. Each dot represents a pair of neurons. The crossshare represents the mean and s.e.m. along each axis. Note for both neuron types, there is no significant difference in sequence ratio between periods with and without theta oscillations.



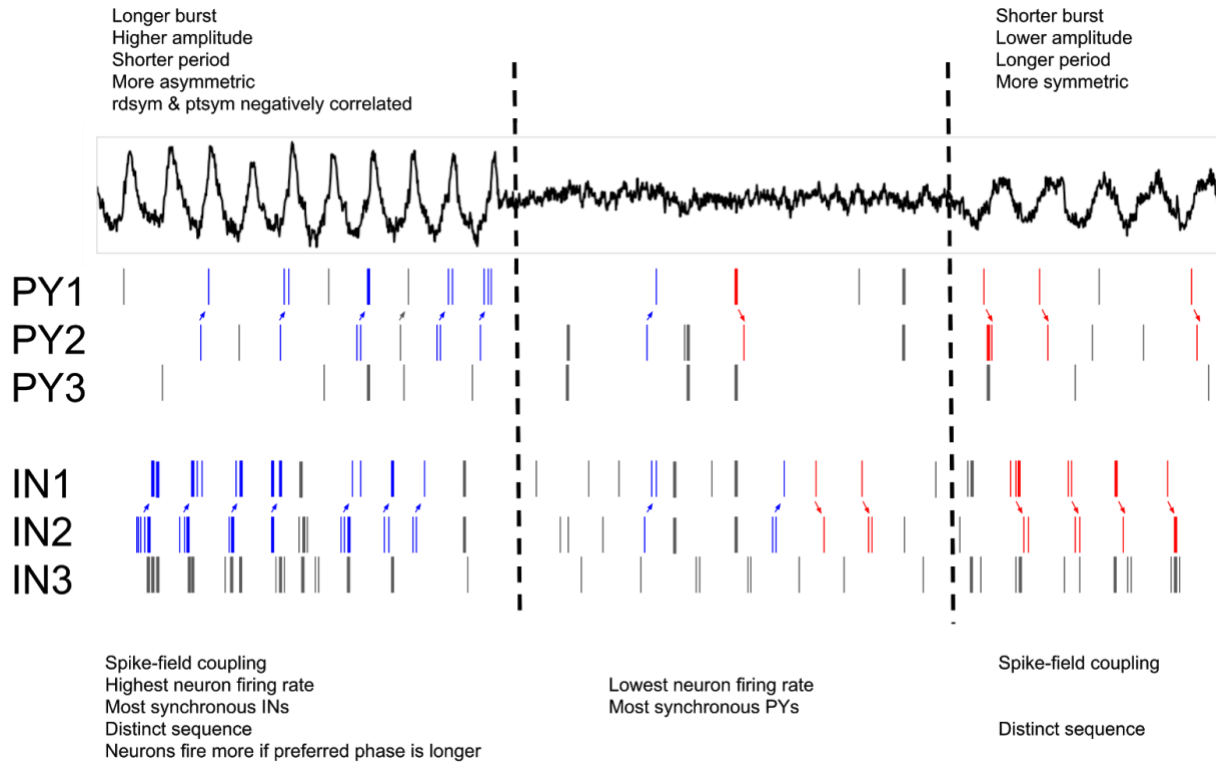


Figure 3.8. Schematized summary of observed relationships between theta oscillation bursting, waveform shape, and local neuronal firing patterns. A field potential (top) was simulated to show three different regimes of a hippocampal recording: a burst of asymmetric theta cycles (left), non-oscillatory activity (center), and a burst of symmetric theta waves. The asymmetric period would be most associated with the rat running, given its higher amplitudes, shorter periods, and relatively short rises and peaks compared to the latter symmetric theta burst (c.f. Figure 3.3). The rise-decay symmetry and peak-trough symmetry of asymmetric cycles are negatively correlated (c.f. Figure 3.2C,F). Additionally, the theta burst with more asymmetric cycles lasts longer than the symmetric burst (c.f. Figure 3.7B). Below the field potential is schematized firing of 3 pyramidal neurons (PY1, PY2, PY3) and 3 interneurons (IN1, IN2, IN3). Vertical lines indicate spikes from each neuron. The pyramidal neurons are coupled to the rise period after the trough, whereas the interneurons are coupled to the decay period before the trough (c.f. Figure 3.4). These neurons fire most when their preferred phase of firing is longest (c.f. Figure 3.5E,F) as well as firing most during the asymmetric burst (c.f. Figure 3.5, Figure 3.7D,E). During the asymmetric burst, interneurons are most synchronous (thick spikes) with one another (c.f. Figure 3.6B, Figure 3.7G). Pyramidal neurons are most synchronous when no theta rhythm is present (c.f. Figure 3.7F). The relative sequence of a pair of pyramidal neurons (PY1, PY2) and a pair of interneurons (IN1, IN2) are systematically different between the asymmetric and symmetric theta bursts (c.f. Figure 3.6E-G). Arrows are drawn and spikes are colored to clearly indicate the sequence of these neuron pairs (blue spikes are the sequence 2→1, red spikes are 1→2), though note that the sequences are arbitrary. However, when collapsing across both periods of theta oscillations, the sequence is no more stereotyped than during the time between theta bursts (c.f. Figure 3.7H,I).

Discussion

This study provides a unique perspective on the rodent hippocampal theta oscillation by segmenting theta into individual cycles and analyzing how local spiking relates to nonsinusoidal cycle features and theta oscillation presence, as summarized in Figure 3.8. Such analyses are only possible using analytics based in the time domain, such as the cycle-by-cycle framework.

Specifically, we uncover several novel characteristics of the nonsinusoidal theta oscillation and its relationship to putative excitatory and inhibitory firing rates, spike synchrony, and spike sequences. For one, the peak-trough asymmetry of the theta rhythm has not previously been parameterized or studied, but here we find that it has a characteristic asymmetry that systematically relates to both rat movement and neuron sequence. Our analysis of rise-decay symmetry extends significantly on the previous, mostly qualitative, reports of the sawtooth-like nature of the hippocampal theta rhythm (Buzsáki et al., 1985; Hentschke et al., 2007; Belluscio et al., 2012; Amemiya and Redish, 2018).

Recent work has shown that the theta rise-decay symmetry correlates with the ability to decode present or future position from place cell firing (Amemiya and Redish, 2018). Specifically, current position was more accurately decoded during asymmetric theta cycles, and future position was better decoded during symmetric cycles. Here we extend this result by demonstrating that this rise-decay symmetry correlates with local pyramidal neuron and interneuron firing patterns. Therefore, the higher firing rates, greater synchrony, and specific pairwise sequences in CA1 during asymmetric cycles may be important neural computational elements for representing current position, while representing future position is supported by lower firing rates and synchrony and alternative neuronal sequences.

Non-independence between cycle features and adjacent cycles

During analysis, awareness that the cycle features are not independent of one another (Figure 3.2A-F) is critical. Nonsinusoidal waveform shape is complex, with many possible

features for parametrization. Additionally, it is important to recognize that features are not independent across cycles (Figure 3.2G). The observations that all cycle features are significantly correlated, not only in adjacent cycles but also with nearby cycles, indicates the speed at which the oscillatory dynamics can change. Concretely, neural activity is more similar in two theta cycles within a few seconds compared to two theta cycles that are minutes apart. Because of this lack of independence across cycles, the p-values for statistical tests within a recording should be cautiously interpreted. Therefore, in this paper, we instead computed a single statistic for each recording (e.g., correlation coefficient between firing rate and rise-decay symmetry) and tested if the statistics are randomly distributed around zero.

Burst detection and analysis of oscillatory time periods

Algorithmic determination of theta burst periods allowed us to study how cycle features vary across bursts of theta oscillations. Across cycles, we observed that the theta features were consistently autocorrelated (Figure 3.2G). It is possible this autocorrelation does not extend across distinct theta bursts but only exists within a burst. However, Figure 3.7C showed that the average cycle features of adjacent bursts are generally positively correlated. This could allow us to conclude that the neural dynamics that periodically occur during theta cycles slowly change over time. However, as mentioned in *Methods*, burst detection algorithms are not perfect, so this result should not be considered definitive. Autocorrelation of cycle features between bursts could potentially be an artifact of the algorithm artificially splitting a single burst into multiple bursts due to noise from aperiodic components of neural activity. In this scenario, the truth may be that when a theta burst ends and a new one begins, their oscillatory dynamics are essentially independent of one another. This interpretation still is possible for the minority of the recordings in which no correlation was observed between features in adjacent bursts (Figure 3.7C).

This prediction of burst duration based on cycle features (Figure 3.7B) reflects an interesting aspect of the underlying physiology, in which oscillatory network dynamics that produce more asymmetric field potentials are more stable than those that produce more

symmetric waveforms. This is reminiscent of previous modeling studies that showed that more asymmetric oscillators synchronize more quickly than more sinusoidal oscillators (Somers and Kopell, 1993). Note that theta is generally faster and more asymmetric during running periods (Figure 3.3), and it is generally known that hippocampal theta is persistent during running periods (Vannderwolf, 1964; Teitelbaum and McFarland, 1971; McFarland et al., 1975). Therefore, this observed correlation between cycle features and stationarity is likely partly a consequence of analyzing periods of movement and non-movement together. That said, as stated in the Results, these trends held when accounting for speed in the linear model to predict burst duration from the cycle features. Future analysis using data with thorough behavioral tracking and annotation can tease apart this result in more detail.

Relationship between theta oscillation and neuronal activity

In addition to analyzing trends within the LFP, a burst detection algorithm also opens the possibility for comparing neuronal activity between periods with and without a theta oscillation. We observed that, in general, both putative pyramidal neurons and interneurons increase in firing rate during a theta oscillation (Figure 3.7A,B). From this result, it would be expected that there would be more synchrony between neurons (i.e., pairs of neurons would more likely fire together within a short time window). Indeed, this was observed for interneurons (Figure 3.7B), but surprisingly the opposite trend was observed in general for pyramidal neurons (Figure 3.7A). That is, pyramidal neurons were less synchronous with one another during theta oscillations. From this, we conclude that theta oscillations do not necessarily enhance synchrony between neurons in a local population, which may not be expected given the widespread idea that oscillations synchronize neurons (Engel et al., 1990, 1997, 2001; Livingstone, 1996; Singer, 1999; Fries, 2005). This idea should be further explored regarding the relative synchronization of neurons between regions, or in higher frequency (beta and gamma) bands.

We find that neurons fire at higher rates if a longer part of the theta cycle is spent in its preferred phase. That is, when an individual theta cycle, for example, rises too quickly, a neuron

that prefers a rise phase will have less time to fire at its preferred phase because the oscillation cycled too quickly out of that preferred phase window. However, if that cycle rises more slowly, the neuron will have a longer temporal window in which to fire, as that cycle spends more time in its preferred phase. One potential consequence of this observation is that asymmetries in individual cycles may be a means for controlling representation and/or computation, wherein specific subnetworks of neurons with different preferred phases can be selected for by specific cycle asymmetries. That is, this introduces the notion of neuronal networks that are controlled by the temporal duration of nonsinusoidal waveform features.

Similarly, there is also the idea that during a neural oscillation, neurons fire in a particular sequence that is not present in the absence of the oscillation (Wehr and Laurent, 1996; Mehta et al., 2002; Roux and Uhlhaas, 2014). However, we find no evidence of this in the hippocampal theta rhythm, as the firing sequence in neuron pairs was no more consistent during theta oscillations compared to periods without theta oscillations (Figure 3.7H-I). This may indicate that neuronal sequences are independent of the presence of the theta rhythm. It is still theoretically possible that higher order sequences (3+ neurons) are more consistent during theta oscillations, but more complex methods are required to assess this scenario. Even then, it is rather strange to consider a scenario in which theta oscillations coordinate longer sequences while having no effect on pairwise sequence consistency.

Future directions

This manuscript serves as the first work to systematically relate nonsinusoidal waveform features of a neural oscillation to local neuronal spiking patterns. We showed that neuronal activation patterns correlate with the waveform shape of the theta oscillation, suggesting that changes in the symmetry of an oscillation may reflect qualitative changes in the function of the oscillation. This established relationship to spiking may help motivate and inform applications of nonsinusoidal features as predictive features for brain-machine interfaces or biomarkers for disease.

This work can be extended in several ways to further explore the potential significance and interpretations of oscillatory waveform asymmetries. It may be advantageous to study spatial patterns of the field potential (Agarwal et al., 2014). Additionally, studying simultaneous intracellular voltage and extracellular recordings may elucidate how fluctuations in the field potential relate to excitatory and inhibitory synaptic input. Since the field potential is not generated simply from the local spiking patterns (Herreras, 2016) neuronal activity from different brain regions may account for significant variance in the field potential recordings.

In addition to the rodent hippocampal theta rhythm, the relationship between the LFP waveform and local spiking patterns should be conducted in different frequency bands, brain regions, and species. Furthermore, new techniques may be developed to capture important features of oscillatory dynamics. For example, the “smoothness” of the oscillation was not studied here, and state-of-the-art deep learning methods could provide some informative, though less intuitive, features. Ultimately, this work only scratches the surface of future efforts to better understand the physiological, behavioral, and functional significance of neural oscillation waveform shape.

Chapter 3, in full, has been submitted for publication of the material as it currently appears in: Cole SR, Voytek B. (2018) Hippocampal theta bursting and waveform shape reflect CA1 spiking patterns. *bioRxiv*. The dissertation author was the primary investigator and author of this paper.

References

- Agarwal G, Stevenson IH, Berényi A, Mizuseki K, Buzsáki G, Sommer FT (2014) Spatially distributed local fields in the hippocampus encode rat position. *Science* 344:626–630.
- Amemiya S, Redish AD (2018) Hippocampal Theta-Gamma Coupling Reflects State-Dependent Information Processing in Decision Making. *Cell Rep* 22:3328–3338.
- Amzica F, Steriade M (1998) Electrophysiological correlates of sleep delta waves. *Electroencephalogr Clin Neurophysiol* 107:69–83.
- Belluscio MA, Mizuseki K, Schmidt R, Kempter R, Buzsáki G (2012) Cross-frequency phase-phase coupling between θ and γ oscillations in the hippocampus. *J Neurosci* 32:423–435.
- Benjamini YH, Hochberg Y (1995) Controlling The False Discovery Rate - A Practical And Powerful Approach To Multiple Testing. *Journal of the Royal Statistical Society Series B: Methodological*.
- Berens P (2009) circstat : a *MATLAB* toolbox for circular statistics. *J Stat Softw* 31.
- Brunn A (2004) Fourier-, Hilbert- and wavelet-based signal analysis: are they really different approaches? *J Neurosci Methods* 137:321–332.
- Buzsáki G, Anastassiou CA, Koch C (2012) The origin of extracellular fields and currents--EEG, ECoG, LFP and spikes. *Nat Rev Neurosci* 13:407–420.
- Buzsáki G, Draguhn A (2004) Neuronal oscillations in cortical networks. *Science* 304:1926–1929.
- Buzsáki G, Rappelsberger P, Kellényi L (1985) Depth profiles of hippocampal rhythmic slow activity ('theta rhythm') depend on behaviour. *Electroencephalogr Clin Neurophysiol* 61:77–88.
- Buzsáki G, Wang X-J (2012) Mechanisms of gamma oscillations. *Annu Rev Neurosci* 35:203–225.
- Cohen MX (2017) Where does EEG come from and what does it mean? *Trends Neurosci* 40:208–218.
- Cole SR, van der Meij R, Peterson EJ, de Hemptinne C, Starr PA, Voytek B (2017) Nonsinusoidal beta oscillations reflect cortical pathophysiology in parkinson's disease. *J Neurosci* 37:4830–4840.
- Cole SR, Voytek B (2017) Brain oscillations and the importance of waveform shape. *Trends Cogn Sci (Regul Ed)* 21:137–149.
- Cole SR, Voytek B (2018) Cycle-by-cycle analysis of neural oscillations. *BioRxiv*.
- Dvorak D, Fenton AA (2014) Toward a proper estimation of phase-amplitude coupling in neural oscillations. *J Neurosci Methods* 225:42–56.

- Einevoll GT, Kayser C, Logothetis NK, Panzeri S (2013) Modelling and analysis of local field potentials for studying the function of cortical circuits. *Nat Rev Neurosci* 14:770–785.
- Einevoll GT, Pettersen KH, Devor A, Ulbert I, Halgren E, Dale AM (2007) Laminar population analysis: estimating firing rates and evoked synaptic activity from multielectrode recordings in rat barrel cortex. *J Neurophysiol* 97:2174–2190.
- Engel AK, Fries P, Singer W (2001) Dynamic predictions: oscillations and synchrony in top-down processing. *Nat Rev Neurosci* 2:704–716.
- Engel AK, König P, Gray CM, Singer W (1990) Stimulus-Dependent Neuronal Oscillations in Cat Visual Cortex: Inter-Columnar Interaction as Determined by Cross-Correlation Analysis. *Eur J Neurosci* 2:588–606.
- Engel AK, Roelfsema PR, Fries P, Brecht M, Singer W (1997) Role of the temporal domain for response selection and perceptual binding. *Cereb Cortex* 7:571–582.
- Feingold J, Gibson DJ, DePasquale B, Graybiel AM (2015) Bursts of beta oscillation differentiate postperformance activity in the striatum and motor cortex of monkeys performing movement tasks. *Proc Natl Acad Sci USA* 112:13687–13692.
- Fransen AMM, van Ede F, Maris E (2015) Identifying neuronal oscillations using rhythmicity. *Neuroimage* 118:256–267.
- Fries P (2005) A mechanism for cognitive dynamics: neuronal communication through neuronal coherence. *Trends Cogn Sci (Regul Ed)* 9:474–480.
- Gao R, Peterson EJ, Voytek B (2017) Inferring synaptic excitation/inhibition balance from field potentials. *Neuroimage* 158:70–78.
- Haider B, Schulz DPA, Häusser M, Carandini M (2016) Millisecond coupling of local field potentials to synaptic currents in the awake visual cortex. *Neuron* 90:35–42.
- Haller M, Donoghue T, Peterson E, Varma P, Sebastian P, Gao R, Noto T, Knight RT, Shestyuk A, Voytek B (2018) Parameterizing neural power spectra. *BioRxiv*.
- Harris KD, Henze DA, Csicsvari J, Hirase H, Buzsáki G (2000) Accuracy of tetrode spike separation as determined by simultaneous intracellular and extracellular measurements. *J Neurophysiol* 84:401–414.
- Hentschke H, Perkins MG, Pearce RA, Banks MI (2007) Muscarinic blockade weakens interaction of gamma with theta rhythms in mouse hippocampus. *Eur J Neurosci* 26:1642–1656.
- Herreras O (2016) Local field potentials: myths and misunderstandings. *Front Neural Circuits* 10:101.
- Herreras O, Makarova J, Makarov VA (2015) New uses of LFPs: Pathway-specific threads obtained through spatial discrimination. *Neuroscience* 310:486–503.

- Hughes AM, Whitten TA, Caplan JB, Dickson CT (2012) BOSC: a better oscillation detection method, extracts both sustained and transient rhythms from rat hippocampal recordings. *Hippocampus* 22:1417–1428.
- Jas M, Tour T, Şimşekli U, Re G (2017) Learning the Morphology of Brain Signals Using Alpha-Stable Convolutional Sparse Coding. Arxiv.
- Jasper HH (1948) Charting the Sea of Brain Waves. *Science* 108:343–347.
- Jones SR (2016) When brain rhythms aren't "rhythmic": implication for their mechanisms and meaning. *Curr Opin Neurobiol* 40:72–80.
- Klimesch W (1999) EEG alpha and theta oscillations reflect cognitive and memory performance: a review and analysis. *Brain Res Rev* 29:169–195.
- König P, Engel AK, Singer W (1996) Integrator or coincidence detector? The role of the cortical neuron revisited. *Trends Neurosci* 19:130–137.
- Kosciessa JQ, Grandy TH, Garrett DD, Werkle-Bergner M (2018) Single-trial characterization of neural rhythms: potentials and challenges. *BioRxiv*.
- Le Van Quyen M, Foucher J, Lachaux J, Rodriguez E, Lutz A, Martinerie J, Varela FJ (2001) Comparison of Hilbert transform and wavelet methods for the analysis of neuronal synchrony. *J Neurosci Methods* 111:83–98.
- Lee H, Simpson GV, Logothetis NK, Rainer G (2005) Phase locking of single neuron activity to theta oscillations during working memory in monkey extrastriate visual cortex. *Neuron* 45:147–156.
- Li C -I., McLennan H, Jasper H (1952) Brain waves and unit discharge in cerebral cortex. *Science* 116:656–657.
- Lindén H, Pettersen KH, Einevoll GT (2010) Intrinsic dendritic filtering gives low-pass power spectra of local field potentials. *J Comput Neurosci* 29:423–444.
- Lindén H, Tetzlaff T, Potjans TC, Pettersen KH, Grün S, Diesmann M, Einevoll GT (2011) Modeling the spatial reach of the LFP. *Neuron* 72:859–872.
- Livingstone MS (1996) Oscillatory firing and interneuronal correlations in squirrel monkey striate cortex. *J Neurophysiol* 75:2467–2485.
- Lozano-Soldevilla D (2018) Nonsinusoidal neuronal oscillations: bug or feature? *J Neurophysiol* 119:1595–1598.
- Lundqvist M, Rose J, Herman P, Brincat SL, Buschman TJ, Miller EK (2016) Gamma and beta bursts underlie working memory. *Neuron* 90:152–164.
- Mazzoni A, Lindén H, Cuntz H, Lansner A, Panzeri S, Einevoll GT (2015) Computing the Local Field Potential (LFP) from Integrate-and-Fire Network Models. *PLoS Comput Biol* 11:e1004584.

- McFarland WL, Teitelbaum H, Hedges EK (1975) Relationship between hippocampal theta activity and running speed in the rat. *J Comp Physiol Psychol* 88:324–328.
- Mehta MR, Lee AK, Wilson MA (2002) Role of experience and oscillations in transforming a rate code into a temporal code. *Nature* 417:741–746.
- Miller KJ, Sorensen LB, Ojemann JG, den Nijs M (2009) Power-law scaling in the brain surface electric potential. *PLoS Comput Biol* 5:e1000609.
- Mitzdorf U (1985) Current source-density method and application in cat cerebral cortex: investigation of evoked potentials and EEG phenomena. *Physiol Rev* 65:37–100.
- Mizuseki K, Diba K, Pastalkova E, Buzsáki G (2011) Hippocampal CA1 pyramidal cells form functionally distinct sublayers. *Nat Neurosci* 14:1174–1181.
- Mizuseki K, Diba K, Pastalkova E, Teeters J, Sirota A, Buzsáki G (2014) Neurosharing: large-scale data sets (spike, LFP) recorded from the hippocampal-entorhinal system in behaving rats [version 2; referees: 4 approved]. F1000Res.
- Mizuseki K, Sirota A, Pastalkova E, Buzsáki G (2009) Theta oscillations provide temporal windows for local circuit computation in the entorhinal-hippocampal loop. *Neuron* 64:267–280.
- Ness TV, Remme MWH, Einevoll GT (2016) Active subthreshold dendritic conductances shape the local field potential. *J Physiol (Lond)* 594:3809–3825.
- Pastalkova E, Itskov V, Amarasingham A, Buzsáki G (2008) Internally generated cell assembly sequences in the rat hippocampus. *Science* 321:1322–1327.
- Pesaran B, Vinck M, Einevoll GT, Sirota A, Fries P, Siegel M, Truccolo W, Schroeder CE, Srinivasan R (2018) Investigating large-scale brain dynamics using field potential recordings: analysis and interpretation. *Nat Neurosci* 21:903–919.
- Peterson EJ, Voytek B (2018) The trade-off between neural computation and oscillatory coordination. *BioRxiv*.
- Reimann MW, Anastassiou CA, Perin R, Hill SL, Markram H, Koch C (2013) A biophysically detailed model of neocortical local field potentials predicts the critical role of active membrane currents. *Neuron* 79:375–390.
- Roux F, Uhlhaas PJ (2014) Working memory and neural oscillations: α - γ versus θ - γ codes for distinct WM information? *Trends Cogn Sci (Regul Ed)* 18:16–25.
- Roy SA, Alloway KD (2001) Coincidence detection or temporal integration? What the neurons in somatosensory cortex are doing. *J Neurosci* 21:2462–2473.
- Salinas E, Sejnowski TJ (2000) Impact of correlated synaptic input on output firing rate and variability in simple neuronal models. *J Neurosci* 20:6193–6209.
- Siapas AG, Lubenov EV, Wilson MA (2005) Prefrontal phase locking to hippocampal theta oscillations. *Neuron* 46:141–151.

- Singer W (1999) Neuronal synchrony: a versatile code for the definition of relations? *Neuron* 24:49–65, 111.
- Skaggs WE, McNaughton BL (1996) Replay of neuronal firing sequences in rat hippocampus during sleep following spatial experience. *Science* 271:1870–1873.
- Somers D, Kopell N (1993) Rapid synchronization through fast threshold modulation. *Biol Cybern* 68:393–407.
- Stevens CF, Zador AM (1998) Input synchrony and the irregular firing of cortical neurons. *Nat Neurosci* 1:210–217.
- Sweeney-Reed CM, Nasuto SJ, Vieira MF, Andrade AO (2018) Empirical mode decomposition and its extensions applied to EEG analysis: a review. *Advances in Data Science and Adaptive Analysis*.
- Teeters JL, Harris KD, Millman KJ, Olshausen BA, Sommer FT (2008) Data sharing for computational neuroscience. *Neuroinformatics* 6:47–55.
- Teitelbaum H, McFarland WL (1971) Power spectral shifts in hippocampal EEG associated with conditioned locomotion in the rat. *Physiol Behav* 7:545–549.
- Tort ABL, Fontanini A, Kramer MA, Jones-Lush LM, Kopell NJ, Katz DB (2010) Cortical networks produce three distinct 7–12 Hz rhythms during single sensory responses in the awake rat. *J Neurosci* 30:4315–4324.
- Trimper JB, Stefanescu RA, Manns JR (2014) Recognition memory and theta-gamma interactions in the hippocampus. *Hippocampus* 24:341–353.
- Uhlhaas PJ, Singer W (2010) Abnormal neural oscillations and synchrony in schizophrenia. *Nat Rev Neurosci* 11:100–113.
- van Ede F, Quinn AJ, Woolrich MW, Nobre AC (2018) Neural Oscillations: Sustained Rhythms or Transient Burst-Events? *Trends Neurosci* 41:415–417.
- Vannderwolf CH (1964) Electroencephalographic waves with voluntary movement. *Arch Neurol* 11:379.
- Voytek B, Knight RT (2015) Dynamic network communication as a unifying neural basis for cognition, development, aging, and disease. *Biol Psychiatry* 77:1089–1097.
- Ward LM (2003) Synchronous neural oscillations and cognitive processes. *Trends Cogn Sci (Regul Ed)* 7:553–559.
- Wehr M, Laurent G (1996) Odour encoding by temporal sequences of firing in oscillating neural assemblies. *Nature* 384:162–166.
- Womelsdorf T, Valiante TA, Sahin NT, Miller KJ, Tiesinga P (2014) Dynamic circuit motifs underlying rhythmic gain control, gating and integration. *Nat Neurosci* 17:1031–1039.
- Yu AC, Margoliash D (1996) Temporal hierarchical control of singing in birds. *Science* 273:1871–1875.

CONCLUSION

In studying neural oscillations, the analyses we apply are often very complicated, mathematically intensive, and full of assumptions, both explicit and implicit. Therefore, careful consideration of the methods applied to our data is paramount, as seemingly arbitrary choices in the hyperparameters of our analysis (e.g. the minimum number of spikes required for inclusion of a neuron or the length and precise cutoff frequencies of a filter) can have large impacts on the results and ultimate conclusions. Often, in-depth knowledge of the techniques is required in order to appropriately choose hyperparameters and assure the validity of our conclusions. Because considerable effort is required to obtain this knowledge, this means that we will often make honest mistakes in our analysis and as peer reviewers, we often miss the statistical confounds that may underlie highly impactful results. This scientific issue is analogous to a contemporary issue in “fake news” in which data and statistics are either intentionally or ignorantly abused, often in pursuit of an agenda.

There are a few approaches I have found over the course of this thesis work to help alleviate issues I had in trusting my analyses.

1. Deliberate attention to and inspection of raw data is extremely helpful to gaining maximal understanding of our analyses, as complicated methods can often treat our data in ways we do not expect. If we do not understand how we see the ultimate effect by looking at the raw data, there is reason for concern or at least further investigation.
2. Rather than considering the presence of hyperparameters as a “nuisance” that complicates analyses, they can also be valuable tools in order to better understand the data. Hyperparameter settings can be varied, and their effects on the results can be measured in order to better understand the conditions necessary for our results to hold. Suggestion of this approach is a bit ironic, as grid-searching hyperparameters is also a very effective “p-hacking” strategy. Therefore, the efficacy of this approach fully relies on the integrity of the researcher at that moment.

3. In addition to varying hyperparameters, it can similarly be useful to apply multiple methods to our data. When it comes to analyzing neural oscillations, there are several analytic options to choose from (e.g. spectral or cycle-by-cycle analysis), and so this choice should be made consciously. Prior to the work in Chapter 1, I investigated at least six phase-amplitude coupling metrics in order to get a sense of how each of them worked and which, if any, was most appropriate to use with the recordings from the patients with Parkinson's disease. Applying multiple methods and comparing results not only yields a sense of robustness to our results but also often provides a valuable learning experience.

The choice for the analytic method applied can strongly impact the ultimate conclusion. As discussed in Chapter 1, phase-amplitude coupling analysis and sharpness analysis were capturing the same phenomena in the data. However, the former favored a conclusion of coupled oscillators, whereas we favored the latter conclusion concerning synchrony of transmembrane currents.

In Chapter 2, the choice of developing a time-domain approach to analyzing neural oscillations was very deliberate. As physical processes, including neural dynamics, happen over time (as opposed to being generated in the frequency domain), there are advantages in analyzing signals in this natural domain and directly measure and account for nonstationarities in the dynamics. While it is certainly a biased perspective, I believe that neural oscillations research would be better positioned if the default analysis of these rhythms was based in the time domain using a cycle-by-cycle approach instead of a spectral domain approach. While an analysis based on the Fourier transform has an advantage of computational efficiency, this is no longer as important of an advantage, as computational power is now very cheap.

Conversely, our cycle-by-cycle analysis offers some great features that are advantages over a potential spectral approach. First, our approach directly quantifies waveform asymmetry,

which is only indirectly and ambiguously captured in spectral analysis (i.e., similar harmonic patterns can be generated by different oscillators that produce diverse waveforms). Second, cycle-by-cycle analysis inherently runs an oscillation detection algorithm, so oscillatory features are only analyzed on appropriate portions of the signal (i.e., where the oscillation is observable). Third, cycle-by-cycle analysis offers time-resolved estimates of oscillatory features with an appropriate degree of temporal resolution. Not only is symmetry measured for a single cycle, but the estimates of amplitude and frequency are intuitively measured in terms of peak-to-trough voltage and trough-to-trough time, respectively. However, “instantaneous” estimates of amplitude and frequency that are comparatively used offer amplitude and frequency estimates at every point in time. In order to accomplish this, these estimates rely on both narrowband filtering and the complex Hilbert transform. In this approach, both the width of the time window and the behavior on a variety of noisy, nonstationary signals is nonobvious. In Figures 2.5 and 2.6, we demonstrate that the cycle-by-cycle approach can provide more sensitive measures of amplitude and frequency by better differentiating simulated experimental conditions.

Developing this approach to capture the waveform shape of neural oscillations begs the question of what information about neural activity can be gained from this analytic perspective. Chapter 3 showed that the hippocampal theta cycle features, including its symmetry, contain information about the neuronal firing patterns. However, it is still unclear how these differences in waveform shape may reflect differences in neural mechanisms. This is currently unclear, but could be addressed in future experiments and analyses that are designed to compare the changing shape of the field potential to known behavior-related or physiologically-induced changes in oscillatory circuits.

Currently, I abstractly consider oscillation waveform shape as an observed state variable of a dynamical system defined by the oscillatory generator. The trajectory of this oscillation in phase space changes based on changes in the circuit connectivity, input patterns, extracellular ion concentrations, and the dynamics of transmembrane currents. Changes in this trajectory can

be detected as changes in the oscillation waveform shape in addition to the amplitude and frequency. The specific ways in which the waveform shape reflects neural activity are currently unknown, and it is unclear how this will generalize between brain regions.

The pursuit of relating the waveform shape of oscillations to neural mechanisms will greatly benefit from future methodological developments. Not only is a cycle-by-cycle analysis approach being applied to studying waveform shape, but bicoherence has also been applied to show that patients with Schizophrenia have mu rhythms that are less sharp compared to the stereotyped mu rhythms in control subjects (Bartz et al., 2018; Shahbazi Avarvand et al., 2018).

While the current thesis only considered the waveform shape of a single recording at a time, neural recordings are usually collected with a grid of electrodes. Therefore, methods to analyze the spatial patterns of oscillation waveform shape may provide further insights by extracting spatial information about these features. Multivariate convolutional sparse coding is a promising approach for characterizing this information (Agarwal et al., 2014; Jas et al., 2017; La Tour et al., 2018).

The current cycle-by-cycle analysis was limited to four features of oscillatory cycles (amplitude, period, rise-decay symmetry, and peak-trough symmetry), but further features could be defined in order to better distinguish waveforms, such as sine waves and triangle waves. A recent study quantified spectral coupling on a cycle-by-cycle basis by measuring the frequency, power, and timing of gamma oscillations during individual theta cycles in the rodent hippocampus (Lopes-Dos-Santos et al., 2018).

Another limitation of this thesis is that it relied on a burst detection algorithm that defined each point in time as either containing or not containing an oscillation. However, this is a false dichotomy, as it is rarely undoubtedly certain whether or not an oscillation is observable in a neural recording at each point in time. Therefore, this work would benefit from a probabilistic oscillation detection algorithm that captures this nuance in oscillation presence (Andrew Watrous, personal communication).

In conclusion, a cycle-by-cycle characterization of neural oscillations can provide a promising complement to the spectral analysis that has led to many discoveries of the importance of rhythms in the brain.

References

- Agarwal G, Stevenson IH, Berényi A, Mizuseki K, Buzsáki G, Sommer FT (2014) Spatially distributed local fields in the hippocampus encode rat position. *Science* 344:626–630.
- Bartz S, Avarvand FS, Leicht G, Nolte G (2018) Analyzing the waveshape of brain oscillations with bicoherence. *Neuroimage*.
- Jas M, Tour T, Şimşekli U, Re G (2017) Learning the Morphology of Brain Signals Using Alpha-Stable Convolutional Sparse Coding. *Arxiv*.
- La Tour TD, Moreau T, Jas M, Gramfort A (2018) Multivariate Convolutional Sparse Coding for Electromagnetic Brain Signals. *arXiv*.
- Lopes-Dos-Santos V, van de Ven GM, Morley A, Trouche S, Campo-Urriza N, Dupret D (2018) Parsing Hippocampal Theta Oscillations by Nested Spectral Components during Spatial Exploration and Memory-Guided Behavior. *Neuron* 100:940–952.e7.
- Shahbazi Avarvand F, Bartz S, Andreou C, Samek W, Leicht G, Mulert C, Engel AK, Nolte G (2018) Localizing bicoherence from EEG and MEG. *Neuroimage* 174:352–363.